On Decentralized Control of Power Electronics Using Nonlinear Oscillators

A THESIS
SUBMITTED TO THE FACULTY OF THE GRADUATE SCHOOL
OF THE UNIVERSITY OF MINNESOTA
BY

Mohit Sinha

IN PARTIAL FULFILLMENT OF THE REQUIREMENTS
FOR THE DEGREE OF
DOCTOR OF PHILOSOPHY

Prof. Sairaj Dhople, Advisor

November, 2018

To my parents, Mukul and Suprabha Sinha

Acknowledgements

I am enormously grateful to my research advisor Sairaj Dhople for his guidance and support. I am going to reminisce about : our conversations where he patiently evaluated my half-baked ideas and offered interesting directions to explore, our late night sprints to submit articles where he, through his rewritings, taught me the value of effective writing and presentation, and our various discussions that shaped my learnings in the field of power electronics and power systems. I continue to be inspired by his meticulous attention to detail and his systematic approach to solve problems. I am indebted to my mentors and fellow collaborators, Florian Dörfler and Brian Johnson, for their valuable inputs in the articles we wrote together, and for the knowledge they have provided me through our discussions. This dissertation would not have been possible without their hard work and their expert feedback on the preliminary ideas. I would also like to thank Jason Poon, Miguel Rodriguez, Prasanta Achanta, Nathan Ainsworth, and Xiaofan Wu for their contributions and helpful discussions that brought many ideas to fruition.

Secondly, I would like to express my gratitude to the committee members – Ned Mohan, Andrew Lamperski, and Daniel Boley – for their advice and insightful comments that helped me strengthen my thesis. I would also like to thank Bruce Wollenberg for his courses on power systems and Mihailo Jovanovic for his courses on systems theory; they built the foundation for everything that followed. I would be remiss if I don't mention my fellow lab members – Hyungjin, Swaroop, Victor, Sukumar, Ling, and Sanjana– and roommates – Kartik, Vaibhav, Abhishek, Hari and Kishore – who made all these years unforgettable with their friendship.

Finally, I would like to thank my parents and my younger brother for their constant love and support. It was their phone calls and late night Skype calls that kept me sane through difficult times. That, and sometimes films, and books, and music.

Abstract

This thesis develops theoretical tools and hardware prototypes for the decentralized control of power electronic interfaces connected via an electrical network. This research thrust is particularly relevant given that renewable generation, storage devices, and electric vehicles continue to be rapidly integrated with power electronic interfaces into various power systems with ad-hoc control architectures. In particular, controllers are developed for two key applications of inverter control for dc-ac conversion for standalone and grid-connected microgrids, and switch interleaving for multiphase dc-dc conversion, where decentralized control lends a way to ensure robust, efficient and modular operation.

The control philosophy derives from the rich subfield of coupled oscillator theory and focuses on a particular class of second order systems called Liénard-type oscillators. Depending upon the nature of coupling, such oscillators demonstrate emergent patterns of sustained oscillations that can be leveraged to engineer steady-state behavior with stability certificates. Based upon this premise, the core idea is to program the second order nonlinear differential equation onto a micro-controller and use its states to construct switching signals for the power-electronic converters. To close the loop, the output current is used to design a local feedback strategy that guarantees desirable steady-state behavior: synchronized solutions are of interest in inverter systems and phase-balanced solutions are of interest in interleaving switching waveforms for multiphase systems.

Theoretical stability proofs based on Lyapunov and passivity arguments along with extensive hardware results are presented to demonstrate the suitability of the proposed paradigm. In the case of inverters, the work establishes a link between oscillator-based control and the classical droop laws that affords a comprehensive design procedure for synthesis of oscillators which incorporates steady state regulation, control of harmonic content and rate of convergence. Furthermore, a completely communication-free switch interleaving for dc-dc converters has a distinct advantage over the state-of-the-art methods that are at best distributed in nature and have a single point of failure.

Contents

List of Figures

List of Tables

Chapter 1

Introduction

Power electronics form a crucial component of the modern power systems. Driven by solid-state switches, they facilitate the energy conversion from one form to another, ac to dc conversion or vice versa for example to facilitate generation and consumption of electricity in various ways, and are ubiquitous in their presence from cell-phone chargers to high-power motor drives [9–12]. The Electric Power Research Institute (EPRI) estimates that more than 70% of U.S. electrical energy now flows through power electronics, and this will eventually grow to 100% [13]. Under the emerging smart grid paradigm, they are facilitating: significant renewable energy penetration, bulk energy storage systems, energy saving applications in lighting systems, variable speed drives in transportation systems and high efficiency energy transmission systems, and they have had a tremendous impact on the way electricity is produced and consumed. In a lot of these settings, a network of power electronic devices are connected via passive circuit elements viz. capacitor, resistor and inductor to supply power to different loads and it becomes crucial to have a *network level* perspective of the dynamics involved to ensure reliable operation. To this end, this dissertation explores the control challenges that arise when power electronics are connected through an electrical network and proposes modular, efficient and robust algorithms that lend a way to adhoc or plug-n-play architectures and do not require external tuning to adapt to changing operating conditions. In so doing, it supports a paradigm shift in the control and operation of power electronic systems from rigid, hierarchical, and centralized architectures to adaptive decision makers and flat hierarchies that afford distributed optimization and control.

The control problems in power electronics come in various flavors, see [14–16] for a brief survey. Broadly speaking, they could be at the *local* level where the output of a particular converter is to be controlled within a certain range in spite of the variations on the input and

load side or they could be at the *network* level when the output of such converters have to agree to a common value in terms of frequency. The nature of the physics emanating from various devices lead to different models that require varied control design techniques. Often, when power electronic devices are connected in a network, the control algorithms must satisfy requirements both on the local as well as the network level. There are performance metrics involved with the steady-state output behavior – distortion from the ideal sinusoidal behavior, the ripple that is seen in the output capacitor, the losses in the circuit elements – and the transient behavior – maximum voltage or current amplitude reached, rate of convergence to the equilibrium, all of which lead to interesting system theoretic problems depending on the device physics and the interconnection structures. Additionally, in order to enhance reliability and modularity, a *decentralization* constraint is put on real-time control algorithms so that neither communication breakdown adversely impacts the performance nor does the addition of a power-electronic device require tweaking the communication layer. It is particularly relevant where the seamless connection/ disconnection of devices is important and ad-hoc architectures are anticipated. This work focuses on two key applications, which has garnered a lot of attention in power electronics, that features most of these challenges: i) control of inverters for islanded and grid connected AC microgrids, and ii) switch-level interleaving in multiphase dc-dc converters. It is with the belief that the methods studied here that address these two specific control problems inspire similar endeavors with different power electronic devices and network topologies; that the analytical insights gleaned here lay foundation for rigorous mathematical formalisms; and finally, that the prototypes built here get shaped with subsequent innovations into widely accepted technological products.

For the first problem, building on previous works [17–22], where they were first considered, decentralized oscillator-based controllers for H-bridge inverters are developed for ac microgrids to ensure frequency (or phase) synchronization or when the outputs agree on frequency (or phase, respectively). Stronger stability results for a variety of electrical networks, a comprehensive design framework and an evolutionary link between the classical droop laws and the oscillator-based controllers are some of the major highlights that make a compelling case for their use. Extending the control philosophy to dc-dc converters, for the second problem, to solve an opposite problem of phase anti-synchronization, or when the sinusoidal outputs of these oscillators are evenly placed apart, is where this work breaks new ground and, to the best of my knowledge, it's the first work to implement completely communication-free decentralized interleaving for an arbitrary number of converters connected in parallel. The analysis follows the rich tradition of Lyapunov based stability analysis, with significant imports from circuit and passivity theory, and is corroborated by

experimental evidence in both the cases.

This thesis combines the graduate work that have appeared in various conferences and journals, and is organized as follows. Chapter 2 introduces the limit-cycle oscillators which form the basis of controllers and explores their connections to nonlinear circuits. Following which, theoretical results related to phase-synchronization and phase-balancing of trajectories of Liénard-type oscillators are presented, based on articles [23–25], which form the backbone for the analysis in the subsequent chapters. Chapter 3 collects the work on control of inverters and is based on [26–28] while Chapter 4 focuses on dc-dc converters and is based on [29, 30]. Most of the discussion is presented as it appeared in those manuscripts with slight embellishments and interpolations to connect to the overarching theme. Chapter 5 presents the conclusions of this thesis and makes recommendations for future research, which is then followed by several appendices that complement the material covered in preceding chapters. Each chapter includes a survey of the relevant literature.

Chapter 2

Limit-Cycle Oscillators and Nonlinear Circuits

Limit cycles are isolated closed orbits that occur in the phase plane and are objects of perennial interest in the study of nonlinear dynamical systems [31–34]. They are a gateway to model periodic oscillations that are quite prevalent in nature – circadian rhythms, firing of a nerve, or chemical oscillations – and have often proved useful in engineering contexts, to study vibrations on a bridge [35], or example, or characterize oscillations in electrical circuits [36, 37]. Just like equilibrium points, these can be, stable, unstable or semi-stable. When the limit cycles are stable, or the so-called *attractors* exist in the vector field, they give rise to robust sustained oscillations i.e. the system returns to the orbit even after being disturbed from it. Such a trait is highly desirable for switched power electronic systems as it allows a designed periodic behavior in the steady-state. So, it is with this view of dictating stable behavior in the networks of power electronic devices that meets performance objectives that limit-cycle oscillators are considered to form the basis for the controllers. Whilst guaranteeing the existence of limit cycles is an incredibly hard proposition in general, as exemplified by the limited progress on Hilbert's sixteenth problem [38], there are a few classical results for relatively simpler second-order systems which establish existence, uniqueness and stability of the limit cycles. These second-order systems, as presented next, are therefore chosen to form the backbone of the controllers.

Liénard's equation is a nonlinear second-order differential equation of the general form

$$\ddot{x} + f(x)\dot{x} + g(x) = 0. \tag{2.1}$$

This equation is commonly employed to study oscillations in nonlinear dynamical systems, e.g., the Van der Pol oscillator dynamics can be recovered as a special case of Liénard's equation [34] (see, also, Fig. 2.1). The following theorem establishes conditions that the functions $f(\cdot)$ and $g(\cdot)$ need to satisfy so that the system (2.1) exhibits a unique and stable limit cycle around the origin.

Theorem 1 (**Liénard's Theorem [33]**). *Consider the second-order nonlinear dynamical system* (2.1). *Assume that the functions $f(x)$ and $g(x)$ satisfy the following properties:*

(A1) $f(x)$ *and* $g(x)$ *are continuously differentiable* $\forall x$*;*

(A2) $g(x) > 0, \forall x > 0$*; and* $g(x)$ *is an odd function, i.e.,* $g(-x) = -g(x), \forall x$*;*

(A3) $G(x)$ *is an even function, i.e.,* $f(-x) = f(x), \forall x$*;*

(A4) The odd function $F(x) := \int_0^x f(\tau)d\tau$ *has exactly one positive zero at* $x = z$*, is strictly negative for* $0 < x < z$*, is positive and nondecreasing for* $x > z$*, and* $F(x) \to \infty$ *as* $x \to \infty$*.*

Then, the system (2.1) *has a unique and asymptotically stable limit cycle surrounding the origin in the phase plane.*

The conditions of *continuous differentiability* can be relaxed by a slightly more general theorem, which can be stated as under:

Theorem 2 (**Levinson-Smith Theorem [33]**). *Consider the second-order nonlinear dynamical system* (2.1). *Assume that the functions $f(x)$ and $g(x)$ satisfy the following properties:*

(A1) $f(x)$ *is even and continuous* $\forall x$*;*

(A2) $g(x) > 0, \forall x > 0$*; and* $g(x)$ *is an odd function, i.e.,* $g(-x) = -g(x), \forall x$*;*

(A3) $G(x) \to \infty$ *as* $x \to \infty$*, where* $G(x) := \int_0^x g(\tau)d\tau$

(A4) The odd function $F(x) := \int_0^x f(\tau)d\tau$ *has exactly one positive zero at* $x = z$*, is strictly negative for* $0 < x < z$*, is positive and nondecreasing for* $x > z$*, and* $F(x) \to \infty$ *as* $x \to \infty$*.*

Then, the system (2.1) *has a unique and asymptotically stable limit cycle surrounding the origin in the phase plane.*

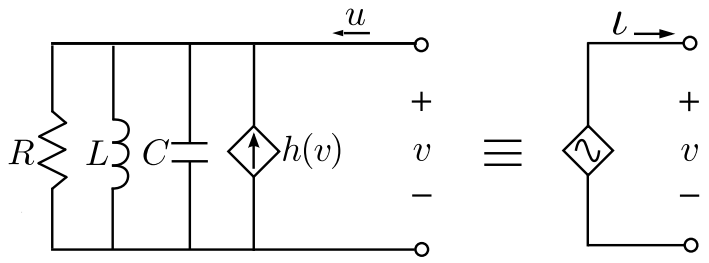

Figure 2.1: The Van der Pol oscillator admits the dynamics in (2.2) with $\omega = 1/\sqrt{LC}$, $\varepsilon = \sqrt{L/C}$ and $f(v) = \varepsilon\alpha\omega(\beta v^2 - 1)$, where α and β are positive constants. The nonlinear voltage-dependent current source is denoted by $h(v) := \int f(v)dv$. (Source: [24])

The proofs are omitted as they are fairly involved and are tangential to the subject matter at hand. Here, this work focuses on *forced* identical Liénard-type oscillator circuits that exhibit unforced oscillations at the frequency ω. The terminal voltage, v, of such circuits is governed by:

$$\ddot{v} + f(v)\dot{v} + \omega^2 v = \dot{u}\,, \tag{2.2}$$

where $f(v)$ satisfies the conditions in Theorem 1, $g(v) = \omega^2 v$, and $u(t)$ is the input to the oscillator. Figure 2.1 depicts an example of the well-known Van der Pol circuit which falls under this class of nonlinear oscillators. If the Van der Pol oscillator circuit shown in Fig. 2.1 is coupled to an electrical network, note that $u = -i$, where i is the output current or in some cases a function of the current. These are the circuits that are virtually executed and form the core of the control algorithms for power electronic converters in the subsequent text. The subsequent chapters 3 and 4 shall keep returning to these circuits to explain the workings of the controllers.

A consequence of the conditions mentioned in Liénard theorem is that the function $f(x)$ is unbounded from below, which in turn can be reinterpreted in terms of passivity theory to be *incrementally output-feedback passive*, and is established in the following result. Passivity and by extension incremental passivity has proven to be instrumental in group coordination problems and output regulation for nonlinear dynamical systems [39–42].

Lemma 1. *Consider the function $f(x)$ that satisfies the conditions in Theorem 1. Then, there exists a lower bound $-\rho < 0$ such that $f(x) \geq -\rho$.*

Proof. Since $f(x)$ is an even function, it suffices to consider only the positive part of the real line as the domain for the function. Since $F(x) := \int_0^x f(\tau)d\tau$ is strictly negative for $0 < x < z$, then $f(x)$ attains a negative value at at least one point. Thus, the lower bound of $f(x)$ has to be strictly negative. Furthermore, $F(x)$ is positive and nondecreasing for

$x > z$, therefore, $F'(x) = f(x) \geq 0$ for $x > z$. Hence, the lower bound is attained in the interval $0 \leq x \leq z$. Now, as the function $f(x)$ is continuously differentiable for all x, it cannot be unbounded from below at a point in the compact interval $0 \leq x \leq z$ or it would not be differentiable at that point. Therefore, $f(x)$ attains a lower bound which is a finite negative number in the interval $0 \leq x \leq z$. □

Lemma 2. *Liénard-oscillator dynamics* (2.2) *is* incrementally output-feedback passive.

Proof. Following the definition in [43], a system of the general form

$$\dot{x} = f(x,u)\ ; y = h_{\text{out}}(x)\ x \in \mathbb{R}^n, y \in \mathbb{R}^q \tag{2.3}$$

is to be *incrementally* output-feedback passive, if there exists a positive definite storage function $\Phi(x,x') : \mathbb{R}^n \times \mathbb{R}^n \to \mathbb{R}_{\geq 0}$, a scalar ρ_0 and two functions $\underline{\alpha}$ and $\overline{\alpha}$ of class $\mathcal{K}_\infty$ such that $\underline{\alpha}(||x-x'||_2) \leq \Phi(x,x') \leq \overline{\alpha}(||x-x'||_2)$ and :

$$\frac{\partial \Phi(x,x')}{\partial x} f(x,u) + \frac{\partial \Phi(x,x')}{\partial x'} f(x',u') \leq \rho_0 (y-y')^{\mathrm{T}}(y-y') + (y-y')^{\mathrm{T}}(u-u') \tag{2.4}$$

for all (x,u,y) and (x',u',y').

The (2.2) can be written in the Lur'e form as:

$$\dot{x} = \begin{bmatrix} 0 & \omega \\ -\omega & 0 \end{bmatrix} x + \begin{bmatrix} 0 \\ 1 \end{bmatrix} (u + f(y))\ ;\ y = v \tag{2.5}$$

where $x = \begin{bmatrix} \omega \int_{\tau=0}^{t} v(\tau) d\tau \\ v \end{bmatrix}$. Then, it is straightforward to see that choosing $\Phi(x,x') = 0.5(x-x')^{\mathrm{T}}(x-x')$ with the oscillator dynamics (2.2), gives the inequality to be

$$\begin{aligned} &\frac{\partial \Phi(x,x')}{\partial x} \left(\begin{bmatrix} \omega & \\ -\omega & 0 \end{bmatrix} x + \begin{bmatrix} 0 \\ 1 \end{bmatrix} (u + F(y)) \right) + \frac{\partial \Phi(x,x')}{\partial x'} \left(\begin{bmatrix} \omega & \\ -\omega & 0 \end{bmatrix} x' + \begin{bmatrix} 0 \\ 1 \end{bmatrix} (u' + F(y')) \right) \\ &\leq (y-y') \left(F(y) - F(y') \right) + (y-y')(u-u') \\ &\leq -\rho (y-y')^2 + (y-y')(u-u')\,, \end{aligned} \tag{2.6}$$

where the last line follows from Lemma 1.

□

In this work, collective motion of such Liénard-type oscillators, when coupled by an elec-

trical network, is what dictates the self-organizing nature of the power electronic converters. It is only fitting that a brief survey of ideas for their emergence of spontaneous order be mentioned at the outset. Broadly related to the algorithms prescribed here is a rich body of literature that has examined synchronization in networks of coupled oscillators and complex dynamical systems [44–46]. In particular, the work leverages notions from incremental stability theory in a similar vein as Lyapunov- and passivity-based methods [47–52], and departs from the alternative input-output $\mathcal{L}_2$ methods in [53, 54], which allows us to relax the Lipschitz-boundedness condition in [54]. Recently, controllers are proposed in [43], based on incremental output-feedback passivity, to relax the Lipschitz boundedness for synchronization of Lur'e nonlinear systems (which includes Liénard-type systems) in networks without shunt elements or the case when Kron reduction yields identical shunt elements. The modelling and analysis framework in [43,51,52] requires the edges (lines connecting the nonlinear circuits) to be strictly input passive, e.g., a parallel RL interconnection, whereas the analysis presented in this work allows us to handle series RL interconnections which are strictly output passive. More importantly, transmission-line models typically assume the circuit model of a series RL interconnection, so this problem setup is relevant to the power-network context.

2.1 Synchronization of Liénard-type Oscillators in Heterogenous Electrical Networks

The nonlinear circuits are coupled through a connected and passive LTI network where the interconnecting lines are modeled as series R-L circuits. The focus is on R-L networks with heterogeneous line characteristics without shunt elements thereby relaxing the uniform resistance-to-inductance ratio modeling assumption that is commonly used in the literature in similar settings. Some of the nodes of the electrical network are connected to the nonlinear circuits and the rest have zero current injections. Notice that the nodes with zero current injections can be eliminated to obtain an equivalent circuit with elementary algebraic manipulations of the network admittance matrix. This model reduction procedure is called Kron reduction. Further details on Kron reduction can be found in [55]. It can be shown that Kron reduction of networks without shunt elements yields networks without shunt elements. Therefore, it suffices to consider only the Kron-reduced networks (i.e., networks with no nodes having zero current injections) in subsequent developments while recognizing that the originating networks may have had more complex topologies.

Lemma 3. *The following statements are equivalent: i) The original electrical network has no shunt elements; ii) The Kron-reduced network has no shunt elements.*

Proof. See [54, Theorem 1]. □

Now that the basic properties of the networks that are relevant to the study are introduced, the problem of global asymptotic synchronization for the coupled network of oscillators is considered next. In particular, a first-order filter on the outputs of the oscillators is designed to ensure synchronization which can otherwise not be guaranteed with just the electrical interconnection. Furtheremore, the analysis suggests a class of heterogeneous dynamic links between the identical oscillators that guarantee synchronization and adds to the findings in [56, 57] where dynamic feedback for Lur'e systems was designed to guarantee synchronization.

Consider a Kron-reduced network interconnecting the N Liénard-type circuits (without shunt elements), recognizing that the originating network may have had additional nodes that were eliminated. Let $\mathcal{N} = \{1, \dots, N\}$ denote the set of nodes with the oscillators, and let $\mathcal{L} = \{1, \dots, L\}$ denote the set of interconnecting transmission lines (edges in the underlying graph). Furthermore, let r_ℓ and l_ℓ denote the resistance and inductance of the ℓ-th edge. To capture the different resistance-to-inductance ratios in branches of the electrical network, define

$$\frac{r_\ell}{l_\ell} =: \gamma_\ell \quad \forall\, \ell \in \mathcal{L}\,. \tag{2.7}$$

Furthermore, let $v = [v_1, \dots, v_N]^{\mathrm{T}}$ collect the voltages at the oscillator terminals, $\eta = [\eta_1, \dots, \eta_L]^{\mathrm{T}}$ collect the edge currents and $\iota = [\iota_1, \dots, \iota_N]^{\mathrm{T}}$ denote the vector with current injections as its entries.

2.1.1 Network Dynamics

Kirchoff's voltage law for the ℓ-th branch in the Kron-reduced network between the j-th and k-th oscillator yields

$$r_\ell \eta_\ell + l_\ell \dot{\eta}_\ell = v_j - v_k\,, \tag{2.8}$$

where η_ℓ is the branch current in the ℓ-th branch. Rearranging terms, and taking the Laplace transform yields

$$(s + \gamma_\ell)\eta_\ell = \frac{1}{l_\ell}(v_j - v_k) = \frac{1}{l_\ell} w_\ell\,, \tag{2.9}$$

where w_ℓ denotes the voltage difference across the ℓ-th edge. It follows that the vector of all nodal-voltage differences can be expressed as

$$w = B^{\mathrm{T}} v, \tag{2.10}$$

where B is the edge-oriented incidence matrix of the network. From (2.9) and (2.10), the Laplace transform of the nodal current-injection vector can be expressed as

$$\iota = B\eta = BD_\gamma(s)D_l^{-1}B^{\mathrm{T}}v, \tag{2.11}$$

where

$$D_\gamma(s) := \mathrm{diag}\{(s+\gamma_1)^{-1}, \ldots, (s+\gamma_L)^{-1}\}, \tag{2.12}$$

$$D_l := \mathrm{diag}\{l_1, \ldots, l_L\}. \tag{2.13}$$

The (transfer) matrices (2.12) and (2.13) are evidently a linear mapping describing the electrical network part of the system.

Recall that the current injections at the nodes are used as feedback to the oscillators to close the loop. In particular, the entries of the vector u (i.e., the vector of oscillator input currents) are specified as $u = -\iota$. While this electrical interconnection has been shown to be sufficient for synchronization in many cases [17, 48], it can be shown to be inadequate in the present heterogeneous setting.

2.1.2 Oscillator Dynamics

Having described the network dynamics, the dynamical model for the oscillators is described next. It is don as a *differential system* (leveraging the projector-matrix notion), while parameterizing the system in the conventional (ξ, v) Lur'e coordinates, where $\xi_j := \omega \int_0^t v_j(t)dt$. Thus, the collective *differential* oscillator dynamics (2.2) are

$$\begin{aligned} \Pi\dot{\xi} &= \omega\Pi v, \\ \Pi\dot{v} &= -\omega\Pi\xi - \Pi H(v) + \Pi u\,, \end{aligned} \tag{2.14}$$

where $v \in \mathbb{R}^N$ is the vector of terminal voltages, $\xi = [\xi_1, \ldots, \xi_N]^{\mathrm{T}} \in \mathbb{R}^N$, Π is the projector matrix, given by $\Pi := I_N - \frac{1}{N}1_N 1_N$ and the following function is defined to contain the

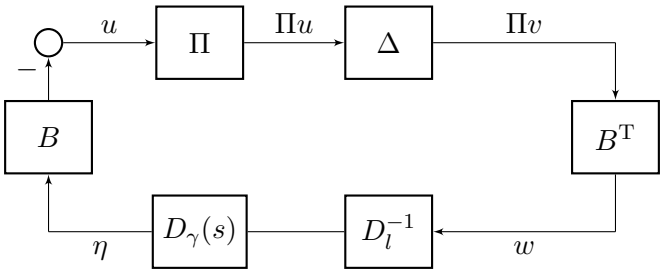

Figure 2.2: Block-diagram representation of interconnected system without the filter and only current feedback. (Source: [25])

nonlinearities:

$$H(v) := \left[\int_0^{v_1} f(r)dr, \ldots, \int_0^{v_N} f(r)dr\right]^{\mathrm{T}}. \tag{2.15}$$

The block diagram in Fig. 2.2 captures the interconnection of the dynamical models discussed above for a Kron-reduced network of N identical Liénard-type oscillators coupled through a heterogeneous R-L network without shunt elements and $L = \binom{N}{2}$ edges. By way of notation, Δ denotes the nonlinear oscillator sub-system as specified by (2.14).

2.1.3 Standard Lyapunov Function

Relying solely on the electrical interconnection (i.e., $u = -\iota$) turns out to be inadequate for synchronization, and it is observed in simulations too. Let us motivate this inadequacy by analytic reasoning. Consider the standard energy-based Lyapunov function suggested by circuit and passivity theory:

$$V = \tfrac{1}{2}(\Pi\xi)^{\mathrm{T}}(\Pi\xi) + \tfrac{1}{2}(\Pi v)^{\mathrm{T}}(\Pi v) + \tfrac{1}{2}\eta^{\mathrm{T}} D_l \eta\,, \tag{2.16}$$

where D_l is defined as in (2.13) The associated time derivative along trajectories of the differential oscillator and circuit dynamics (2.14), (2.8) with the interconnections $w = B^{\mathrm{T}}v$, $\iota = B\eta$, and $u = -\iota$ is (after some manipulations) obtained as

$$\dot{V} = -(\Pi v)^{\mathrm{T}}\Pi H(v) - \eta^{\mathrm{T}} D_r^{-1}\eta\,, \tag{2.17}$$

where $D_r = \mathrm{diag}\{r_1, \ldots, r_L\}$. Observe that $\dot{V}$ is generally sign-indefinite. Alternatively, one may consider a synchronization-inspired Lyapunov function [24]

$$V = \tfrac{1}{2}(\Pi\xi)^{\mathrm{T}}(\Pi\xi) + \tfrac{1}{2}(\Pi v)^{\mathrm{T}}(\Pi v) + \tfrac{1}{2}(\Pi\iota)^{\mathrm{T}}(\Pi\iota). \tag{2.18}$$

The time derivative is obtained (after some manipulations) as

$$\dot{V} = -(\Pi v)^{\mathrm{T}} \Pi H(v) - \eta^{\mathrm{T}} B^{\mathrm{T}} B \Gamma \eta + \eta^{\mathrm{T}} B^{\mathrm{T}} L_l v \,, \tag{2.19}$$

where D_l is as defined in (2.13), and

$$L_l := B D_l^{-1} B^{\mathrm{T}}, \tag{2.20}$$

is the weighted Laplacian matrix associated with the susceptances (inverse inductances) of the network, and

$$\Gamma := \mathrm{diag}\{\gamma_1, \ldots, \gamma_L\} = \mathrm{diag}\{r_1/l_1, \ldots, r_L/l_L\}. \tag{2.21}$$

Again, the time-derivative is indefinite, and no stability certificate can be established. These failing analysis approaches do not only show the inadequacy of the considered Lyapunov functions, but also confirm numerical observations: the closed-loop system may not synchronize.

2.1.4 Filters for Synchronization

A scalar dynamic filter $\kappa s + \tau$ is proposed for the output of the oscillators to facilitate synchronization in the heterogeneous network. A circuit diagram of the implementation is shown in Fig. 2.3. The networked-dynamics of the oscillators with this output filter are shown in the block diagram in Fig. 2.4. Note that the cascade system of the second-order nonlinear oscillator (2.14) and the first-order filter is causal. Hence, from an implementation point of view for converter control [17, 58], the nonlinear oscillator with output filter can readily be implemented in software. For other potential circuit-related applications, it can be realized with current-controlled and voltage-controlled voltage sources.

Since the filter described by the scalar transfer-function block $\kappa s + \tau$, commutes with all other linear blocks in Fig. 2.4, the equivalent block-diagram can be studied in Fig. 2.5 for

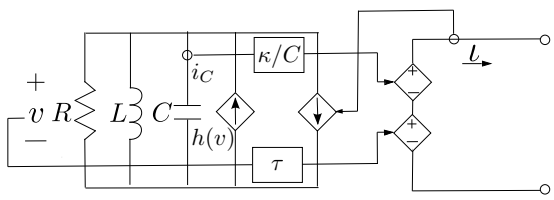

Figure 2.3: The output filter is implemented by using the capacitor current and voltage which in turn control voltage sources. (Source: [25])

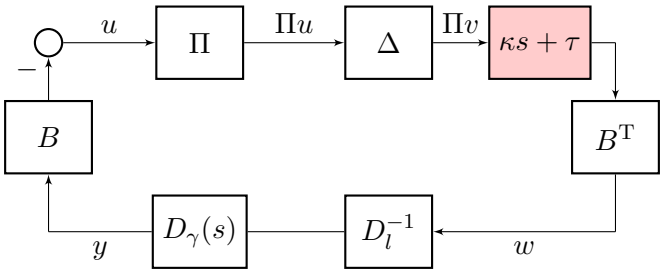

Figure 2.4: Block diagram of the system with the proposed filter (shaded in red) placed at the outputs of the oscillator terminals. (Source: [25])

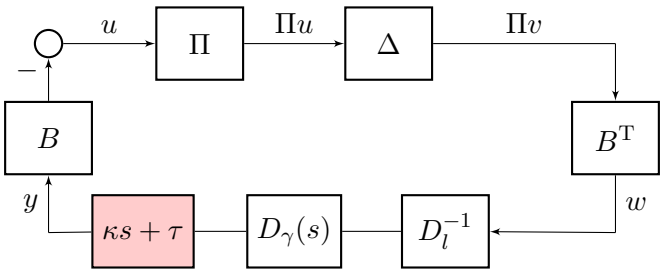

Figure 2.5: Revised block diagram that facilitates analysis derived from the one in Fig. 2.4 leveraging the commutativity of the filter and B. (Source: [25])

the sake of a simplified analysis. The interpretation of Fig. 2.5 is that the edge currents are filtered by the system $\kappa s + \tau$, where κ and τ are design parameters that can be selected to ensure stability of the interconnection. The following result establishes sufficient conditions for the design of this filter so that global asymptotic synchronization in the network of oscillators can be guaranteed.

Theorem 3. *Consider a network of N identical Liénard-type circuits with unforced frequency ω connected through an output filter $\kappa s + \tau$ to a heterogeneous electrical network. Let the maximum resistance-to-inductance ratio in the electrical network be $\gamma_{\max}$, and L_l be the Laplacian matrix associated with the inductances* (3.75)*. Denote the algebraic connectivity corresponding to L_l by $\lambda_2(L_l)$, and let $-\rho$ be the global minimum for the function $f(\cdot)$ for each Liénard oscillator. If the parameters of the output filter, $\kappa s + \tau$, satisfy*

$$\kappa \cdot \lambda_2(L_l) > \rho, \quad \tau/\kappa > \gamma_{\max}, \tag{2.22}$$

then the terminal voltages of the oscillators in the network synchronize asymptotically.

Proof. Consider the block diagram in Fig. 2.5 which illustrates the networked connection

of the oscillators with the output filters (shaded red). In particular, the approach hinges on exploiting the passivity properties of the subsystems and then considering a composite Lyapunov function to establish synchronization. Begin by considering the oscillator system described by (2.14) and denoted by Δ in Fig. 2.5.

Nonlinear Subsystem. The nonlinear block, Δ, is *incrementally output-feedback passive*. To prove this, consider the following Lyapunov function for the system (2.14):

$$V_{\text{osc}} = \frac{1}{2}(\Pi\xi)^{\text{T}}(\Pi\xi) + \frac{1}{2}(\Pi v)^{\text{T}}(\Pi v). \tag{2.23}$$

Given the dynamics (2.14), it follows that:

$$\begin{aligned}\dot{V}_{\text{osc}} &= -(\Pi v)^{\text{T}}\Pi H(v) + (\Pi v)^{\text{T}}\Pi u \\ &\leq \rho(\Pi v)^{T}(\Pi v) + (\Pi v)^{\text{T}}\Pi u\,,\end{aligned} \tag{2.24}$$

where the last line leverages the lower-boundedness of f, i.e., $f(r) \geq -\rho\,\forall r\, \in \mathbb{R}$ as established in Lemma 1.

Linear Subsystem. The transfer function of the linear subsystem which establishes the mapping between the edge voltage differences and filtered edge currents (i.e., it captures the dynamics of the *R-L* line dynamics including the designed filter) is given by

$$D(s) = (\kappa s + \tau)D_{\gamma}(s)D_{l}^{-1}, \tag{2.25}$$

where, $D_{\gamma}(s)$ and D_l are defined in (2.12) and (2.13), respectively. (See Fig. 2.5.) The state-space model of this system can be realized as

$$\begin{aligned}\dot{x} &= -\Gamma x + w \\ y &= D_{l}^{-1}\left((\tau I_L - \kappa\Gamma)x + \kappa w\right)\,,\end{aligned} \tag{2.26}$$

where Γ is defined in (2.21), and I_L is the identity matrix of size $L \times L$. For these dynamics, define the Lyapunov function

$$V_{\text{net}} = \frac{1}{2}x^{\text{T}}Ax, \tag{2.27}$$

where $A := D_l^{-1}(\tau I_L - \kappa\Gamma)$ is a diagonal matrix with

$$A_{jj} := (\tau - \kappa\gamma_j) \cdot l_j > 0, \tag{2.28}$$

given that $\tau > \kappa\gamma_{\max}$ by assumption (2.22). Then,

$$\begin{aligned}
\dot{V}_{\text{net}} &= x^{\mathrm{T}} A(-\Gamma x + w) && \text{(2.29a)}\\
&= -x^{\mathrm{T}} A\Gamma x + w^{\mathrm{T}}(y - \kappa D_l^{-1} w) && \text{(2.29b)}\\
&\leq w^{\mathrm{T}} y - \kappa w^{\mathrm{T}} D_l^{-1} w\,, && \text{(2.29c)}
\end{aligned}$$

where $Ax = (y - \kappa D_l^{-1} w)$ in (2.29a) to get (2.29b) and subsequently use positive definiteness of the matrix $A\Gamma$ to obtain (2.29c). Thus, the linear subsystem is *input strictly passive*.

Interconnection of Linear and Nonlinear Subsystems. The outputs of both the subsystems are connected via the edge-incidence matrix B as $w = B^{\mathrm{T}} v$ and $u = -By$. For the interconnected system, consider the storage function $V_{\text{sys}} = V_{\text{osc}} + V_{\text{net}}$ with derivative given by

$$\begin{aligned}
\dot{V}_{\text{sys}} &= \dot{V}_{\text{osc}} + \dot{V}_{\text{net}} && \text{(2.30a)}\\
&\leq \rho(\Pi v)^{\mathrm{T}}(\Pi v) + (\Pi v)^{\mathrm{T}}\Pi u + w^{\mathrm{T}} y - \kappa w^{\mathrm{T}} D_l^{-1} w && \text{(2.30b)}\\
&= \rho(\Pi v)^{\mathrm{T}}(\Pi v) - v^{\mathrm{T}} B y + v^{\mathrm{T}} B y - \kappa v^{\mathrm{T}} B D_l^{-1} B^{\mathrm{T}} v && \text{(2.30c)}\\
&= \rho(\Pi v)^{\mathrm{T}}(\Pi v) - \kappa v^{\mathrm{T}} L_l v && \text{(2.30d)}\\
&\leq -\left(\kappa\lambda_2(L_l) - \rho\right)(\Pi v)^{\mathrm{T}}(\Pi v). && \text{(2.30e)}
\end{aligned}$$

Above, (2.30b) follows from (2.29) and (2.24), and subsequently $u = -By$, $w = B^{\mathrm{T}} v$, $\Pi B = B$ to get (2.30c). Finally, Πv is orthogonal to 1_N spanning the nullspace of L_l, and thus

$$(\Pi v)^{\mathrm{T}} L_l (\Pi v) \geq \lambda_2(L_l)(\Pi v)^{\mathrm{T}}(\Pi v)\,. \tag{2.31}$$

Therefore, if $\kappa\lambda_2(L_l) > \rho$ then V_{net} is negative semidefinite and, therefore, by Lyapunov stability theorem and LaSalle's invariance principle [59, Theorem 4.1 and 4.4], the origin of the coupled system is globally asymptotically stable. This further implies that the network of oscillators synchronizes asymptotically. □

The main stability condition (2.22) can always be met by choosing appropriate filter parameters κ and τ, and it has the following interpretation: the first inequality $\tau/\kappa > \gamma_{\max}$

restricts the filter time constant τ/κ relative to the largest network time constant $\gamma_{\max} = \max_\ell \frac{r_\ell}{l_\ell}$. Indeed, this first inequality allows us to investigate heterogeneous line dynamics by dominating their time-constants via the filter time constant τ/κ. The second inequality $\kappa \cdot \lambda_2(L_l) > \rho$ requires the effective network coupling (product of the filter gain κ and the algebraic connectivity $\lambda_2(L_l)$) to be larger than the (instability-inducing) negative damping bound ρ.

Next, same set of N Liénard-type oscillators are considered with a *positive* Laplacian coupling to demonstrate the phenomenon of phase-balancing. In this paper, three types of equilibria are studied for a fully-connected system of Liénard-type oscillators in the quasi-harmonic regime: the phase-balanced state, the phase synchronous state, and the bi-cluster synchronous state. To simplify exposition of these different equilibria, consider: i) a collection of N oscillators (indexed in the set $\mathcal{N}$) with phases $\theta_1, \ldots, \theta_N$; and ii) the *order parameter*, $Re^{\jmath\psi} = \frac{1}{N}\sum_{k=1}^{N} e^{\jmath\theta_k}$, a metric that quantitatively captures phase cohesiveness [60–62] and represents the centroid of all oscillators (when conceptualized to be points on the circle). The magnitude of the order parameter is a synchronization measure [62]. The case where $R = 0$ corresponds to the phase-balanced state, i.e., the phases $\theta_1, \ldots, \theta_N$ are spaced apart such that $\sum_{k=1}^{N} e^{\jmath\theta_k} = 0$ [62]. The case where $R = 1$ corresponds to the phase-synchronized state, i.e., the phases $\theta_1, \ldots, \theta_N$ are such that $\theta_\ell = \theta_k, \forall \ell, k \in \mathcal{N}$. One phase-balanced set of particular interest is the splay state where the phases are uniformly distributed around the circle, i.e., $\theta_k = k\frac{2\pi}{N} + \phi \pmod{2\pi}, k \in \mathcal{N}, 0 \leq \phi \leq 2\pi$ [63, 64]. Finally, the bi-cluster synchronous state refers to motion with phases evolving in one of two phase-synchronized clusters, i.e., $\theta_\ell = \theta_k \pmod{\pi}, \forall \ell, k \in \mathcal{N}$. It emerges that altering the signs of the feedback—which is demonstrated in the following section—ensures the stability of the phase-balanced state instead [64–66]. Splay states have also been investigated for various oscillator models like Kuramoto oscillators [67, 68], kinematic models [66, 69], and Van der Pol oscillators [64,65] (which fall in the class of Liénard oscillators considered here). The phase balanced state which contain the splay states is relevant to several engineering systems such as autonomous underwater vehicles; where coordinated, periodic trajectories can be used to collect data with requisite spatial and temporal separation as remarked in [66], or in the control for collective circular motion of nonholonomic vehicles [70]. In this thesis, this emergent phenomenon is exploited is in networks of dc-dc converters in Chapter 4, where carrier wave interleaving, which refers to the temporal separation of the triangular waves used for PWM, minimizes current ripple and harmonics. Using Liénard-type oscillators to locally construct triangular waves of the same phase for each converter, it can be guaranteed that the carrier waves for the converters are interleaved just by virtue of the electrical

network interaction.

The collective motion of $N \geq 2$ identical Liénard-type oscillators described by dynamics (2.2) and indexed by elements in the set $\mathcal{N} := \{1, \ldots, N\}$ is studied. Again, the dynamics of the jth oscillator (2.2) is written in Lur'e form using $y_j(t) = x_j(t)$ and $z_j(t) = \omega \int_0^t x_j(\tau) d\tau$ as states as a first step:

$$\dot{z}_j = \omega y_j, \quad \dot{y}_j = -\omega z_j - \varepsilon h(y_j) + \varepsilon u_j \,, \tag{2.32}$$

where $h_j : \mathbb{R} \to \mathbb{R}$ is defined as$\int_{s=0}^{y_j} f(s) ds$The oscillators are connected over an undirected graph $\mathcal{G}$, and it is assumed that the graph is complete (this can be further relaxed easily, but this chapter sticks to this for ease of exposition) and without self loops. Denoting $u = [u_1, \ldots, u_N]^{\mathrm{T}}$ and $y = [y_1, \ldots, y_N]^{\mathrm{T}}$, the interactions between the oscillators are captured by the *positive* (and thus repulsive) diffusive coupling

$$u = Ly, \tag{2.33}$$

where $L = NI_N - 1_N 1_N^{\mathrm{T}}$ is the Laplacian matrix of $\mathcal{G}$.

2.1.5 Averaging Theory

In the parametric regime $0 < \varepsilon \ll 1$, the dynamical behavior of individual oscillators is weakly nonlinear, and they are weakly coupled. This results in multiple time-scale behavior, the analysis of which can be significantly simplified with periodic averaging [59]. Consider a time-varying dynamical system

$$\dot{x} = \varepsilon p(x, t, \varepsilon), \tag{2.34}$$

with time-periodic vector field $p(x, t, \varepsilon) = p(x, t + T, \varepsilon)$ with period $T > 0$, and $0 < \varepsilon \ll 1$. The associated *time-averaged dynamical system* is given by

$$\dot{\overline{x}} = \varepsilon \overline{p}(\overline{x}) = \varepsilon \frac{1}{T} \int_{\tau=0}^{T} p(\overline{x}, \tau, 0) d\tau. \tag{2.35}$$

The solution of the averaged system (2.35) in the time scale εt is $\mathcal{O}(\varepsilon)$ *close* to the solution of the original system (2.34), i.e.,

$$||x(t, \varepsilon) - \overline{x}(\varepsilon t)||_2 = \mathcal{O}(\varepsilon), \quad \forall t \in [0, t^*], \tag{2.36}$$

for some $t^* > 0$ for which unique solutions exist for both (2.34) and (2.35), and assuming $||x(0,\varepsilon) - \overline{x}(0)||_2 = \mathcal{O}(\varepsilon)$. This allows to work with *averaged* quantities without compromising on accuracy while inferring the dynamics of the original system. Such a formulation is revisited again and again in the following chapters 3 and 4.

In addition to this standard setting for Liénard-type oscillators, the following assumption is made on the function $h(x)$ – $h(x) = \frac{N}{2}x$ admits a unique positive solution, ρ, and $\left(\int_0^x h\left(s\right) ds - cx^2\right) \to \infty$ as $x \to \infty$ for any real scalar $c \in \mathbb{R}$.

This is a mild restriction and is satisfied, e.g., for the Van der Pol oscillator for which $h(x) = x^3/3 - x$.

2.2 Convergence to Phase-Balanced Solutions

In this section, the nature of the trajectories of the coupled Liénard oscillators is characterized and the stability of a few equilibria of interest is studied.

2.2.1 Averaged Model

Consider the following bijective coordinate transformation from the state-space model in (2.32) to polar coordinates:

$$z_j \ \to r_j \sin\left(\omega t + \theta_j\right), \quad y_j \ \to r_j \cos\left(\omega t + \theta_j\right). \tag{2.37}$$

In these new set of coordinates, the amplitude dynamics of the j oscillator are given by:

$$\begin{aligned}\dot{r}_j = &-\varepsilon h(r_j \cos(\omega t + \theta_j)) \cos(\omega t + \theta_j) \\ &- \varepsilon \sum_{k=1}^{N} (r_k \cos(\omega t + \theta_k)) \cos(\omega t + \theta_j),\end{aligned} \tag{2.38}$$

and the phase dynamics are given by

$$\begin{aligned}\dot{\theta}_j = &\frac{\varepsilon}{r_j} h(r_j \cos(\omega t + \theta_j)) \sin(\omega t + \theta_j) \\ &+ \frac{\varepsilon}{r_j} \sum_{k=1}^{N} (r_k(\cos \omega t + \theta_k)) \sin(\omega t + \theta_j).\end{aligned} \tag{2.39}$$

Using the averaging operation in (2.35), the amplitude and phase dynamics of the non-autonomous system above in (2.38)–(2.39) can be approximated with the following au-

tonomous system (the simple but lengthy integral calculations is omitted)

$$\dot{\overline{r}}_j = -\varepsilon\overline{h}(\overline{r}_j) + \frac{\varepsilon(N-1)}{2}\overline{r}_j - \frac{\varepsilon}{2}\sum_{k=1,k\neq j}^{N}\overline{r}_k\cos(\overline{\theta}_{jk}),$$

$$\dot{\overline{\theta}}_j = \frac{\varepsilon}{2\overline{r}_j}\sum_{k=1,k\neq j}^{N}\overline{r}_k\sin(\overline{\theta}_{jk}), \tag{2.40}$$

where $\overline{\theta}_{jk} := \overline{\theta}_j - \overline{\theta}_k$ for notational convenience. The dynamics in (2.40) allows restricting attention to the domain $\overline{r}_j > 0$, $\forall j \in \mathcal{N}$. This is formalized next.

Proposition 1. *The set*

$$\mathcal{I} := \{(\overline{r},\overline{\theta}) \in \mathbb{R}^N_{\geq 0} \times \mathbb{T}^N : \overline{r}_j > 0, \forall j \in \mathcal{N}\} \tag{2.41}$$

is positively invariant under the flow (2.40).

Proof. The state-space model (2.32) in Euclidean coordinates can be extended to the following interconnected system:

$$\dot{z} = \omega y\,;\; \dot{y} = -\omega z - \varepsilon\Gamma(y) + \varepsilon L y\,, \tag{2.42}$$

where $z = [z_1,\ldots,z_N]^{\mathrm{T}}$ and $y = [y_1,\ldots,y_N]^{\mathrm{T}}$ collect the states of the N connected oscillators, and $\Gamma(y) := [h(y_1),\ldots,h(y_N)]^{\mathrm{T}}$, with $h(\cdot)$ defined in (**??**). The Jacobian of (2.42) around the origin is denoted by J_0 and it is given by:

$$J_0 := \left[\begin{array}{c|c} 0 & \omega I_N \\ \hline -\omega I_N & \Lambda \end{array}\right], \tag{2.43}$$

where $\Lambda := \varepsilon\Gamma'(0) + \varepsilon L$ is a diagonally dominant matrix with positive diagonal entries and is therefore positive definite. Let the set $\{\lambda_1,\ldots,\lambda_N\}$ denote eigenvalues of Λ. Then, $2N$ eigenvalues of J_0 can be written as $0.5\left(\lambda_j \pm \sqrt{\left(\lambda_j^2 - 4\omega^2\right)}\right), j \in \mathcal{N}$. Thus, the real parts of the eigenvalues of the Jacobian at the origin are positive and therefore the origin does not have a stable manifold and is repulsive [71]. Now, going back to the averaged polar coordinates, recall that

$$\overline{r}_j(t) = \frac{\omega}{2\pi}\int_{t-2\pi/\omega}^{t} r_j(\tau)d\tau\,. \tag{2.44}$$

Since $r_j(t)$ is a nonnegative and $2\pi/\omega$-periodic quantity, $\overline{r}_j = 0$ if and only if there exists an

interval $[t_1, t_2]$ of length greater than the period, i.e., $|t_2 - t_1| \geq 2\pi/\omega$ such that $r_j(t) = 0$ for $t \in [t_1, t_2]$. As the trajectories with $r_j(t) = 0$ are unstable, therefore the set $\mathcal{I}$ is positively invariant. □

2.2.2 Lyapunov Stability

Now, the averaged model is used in (2.40) to study the nature of the trajectories of the collective motion of oscillators and their stability. To this end, various sets are defined in which the equilibria of the dynamics could reside.

Definition 1 (**Phase-balanced Set**). *The set that describes collective motion where the centroid of the coupled oscillator system in polar coordinates is at the origin referred to as the* phase-balanced *set,* $\mathcal{S}$*:*

$$\mathcal{S} := \big\{(\overline{r}, \overline{\theta}) \in \mathcal{I} : \overline{r}_j = \overline{r}_k, \sum_{k=1}^{N} \mathrm{e}^{\jmath\overline{\theta}_k} = 0, \forall j, k \in \mathcal{N}\big\}. \tag{2.45}$$

This is similar to the *balanced set* defined in [62,72]. Another set of solutions, the cluster synchronous set, is defined next.

Definition 2 (**Bi-Cluster Synchronous Set**). *The set that describes collective motion in which the oscillators belong to one of two phase-synchronized clusters, which are* π *apart themselves, is called the* bi-cluster synchronous *set,* $\mathcal{S}'$*:*

$$\mathcal{S}' := \big\{(\overline{r}, \overline{\theta}) \in \mathcal{I} : \dot{\overline{r}}_j = 0 \ \ \overline{\theta}_{jk} = m\pi \ \forall j, k \in \mathcal{N}, m \in \mathbb{Z}\big\}. \tag{2.46}$$

Finally, the phase-synchronized set is defined.

Definition 3 (**Phase Synchronous Set**). *The set that describes the phase-synchronized collective motion is called the* phase synchronous *set,* $\mathcal{S}''$*:*

$$\begin{aligned} \mathcal{S}'' := \big\{(\overline{r}, \overline{\theta}) \in \mathcal{I} : \overline{r}_j = \overline{r}_k, \, \overline{\theta}_{jk} = 2m\pi \\ \forall j, k \in \mathcal{N}, \, m \in \mathbb{Z}\big\}. \end{aligned} \tag{2.47}$$

It is worth pointing out a few facts about the sets described above. First, note that $S'' \subset S'$ and $S'' \cap S = \emptyset$. Furthermore, $S \cap S' \neq \emptyset$ if and only if the number of oscillators are even and each of the two phase-synchronized clusters in $\mathcal{S}'$ have exactly the same number of oscillators. These aspects are illustrated in Fig. 2.6. Next, a Lyapunov function is

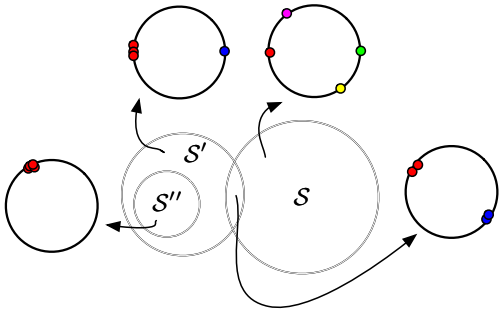

Figure 2.6: Equilibria from the phase-balanced set, $\mathcal{S}$, the bi-cluster synchronous set, $\mathcal{S}'$, and the phase-synchronous set, $\mathcal{S}''$ are depicted to demonstrate the nature of the trajectories in polar coordinates. In particular, $\mathcal{S}'' \subset \mathcal{S}'$ and $\mathcal{S}'' \notin \mathcal{S}$. Furthermore, $\mathcal{S}$ and $\mathcal{S}'$ have common elements if and only if the number of oscillators are even and each of the two phase-synchronized clusters in $\mathcal{S}'$ have exactly the same number of oscillators. (Source: [23])

constructed to establish convergence of trajectories generated by (2.40) starting from initial conditions in the set $\mathcal{I}$ to the phase-balanced set, $\mathcal{S}$, or the bi-cluster synchronous set, $\mathcal{S}'$.

Theorem 4. *Consider the collective motion of the N networked oscillators, with the dynamics of each described by the flow* (2.40)*. Then, for all initial conditions $(\overline{r}_0, \overline{\theta}_0) \in \mathcal{I}$, trajectories converge either to $\mathcal{S}$* (2.45) *or $\mathcal{S}'$* (2.46)*.*

Proof. The dynamics (2.40) can be written as the gradient flow:

$$\dot{\overline{r}}_j = -\nabla_{\overline{r}_j} V(\overline{r}, \overline{\theta})\,;\, \dot{\overline{\theta}}_j = -\frac{1}{\overline{r}_j^2} \nabla_{\overline{\theta}_j} V(\overline{r}, \overline{\theta}), \tag{2.48}$$

where $V(\overline{r}, \overline{\theta})$ is a potential function given by

$$\begin{aligned} V(\overline{r}, \overline{\theta}) = \varepsilon \Bigg(& \sum_{j=1}^{N} \int_{\tau=0}^{\overline{r}_j} \overline{h}(\tau) d\tau - \frac{N-1}{4} \sum_{j=1}^{N} \overline{r}_j^2 \\ & + \frac{1}{2} \sum_{j=1}^{N} \sum_{k=1, k\neq j}^{N} \overline{r}_j \overline{r}_k \cos(\overline{\theta}_{jk}) \Bigg). \end{aligned} \tag{2.49}$$

The level sets of $V(\overline{r}, \overline{\theta})$ are closed (due to continuity), bounded in $\overline{\theta}$ (due to boundedness of the trigonometric nonlinearities), and radially unbounded in $\overline{r}$ (due to Assumption 1).

Next, the time derivative of $V(\overline{r},\overline{\theta})$ along the trajectories of the system is given by

$$\begin{aligned}\dot{V}(\overline{r},\overline{\theta}) &= \left(\nabla_{\overline{r}_j} V\left(\overline{r},\overline{\theta}\right)\right)^{\mathrm{T}} \dot{\overline{r}}_j + \left(\nabla_{\overline{\theta}_j} V\left(\overline{r},\overline{\theta}\right)\right)^{\mathrm{T}} \dot{\overline{\theta}}_j \\ &= -\left(\nabla_{\overline{r}_j} V\left(\overline{r},\overline{\theta}\right)\right)^2 - \overline{r}_j^2 \left(\frac{1}{\overline{r}_j^2}\nabla_{\overline{\theta}_j} V\left(\overline{r},\overline{\theta}\right)\right)^2 \leq 0.\end{aligned}$$

Therefore, the sublevel sets of $V(\overline{r},\overline{\theta})$ are forward invariant, and thus by LaSalle's invariance principle [59, Theorem 4.4] it follows that the dynamics (2.40) converge to the largest positively invariant set contained in

$$\left\{(\overline{r},\overline{\theta}) \in \mathcal{I} :\, V(\overline{r},\overline{\theta}) \leq V(\overline{r}_0,\overline{\theta}_0)\,,\, \dot{V}(\overline{r},\overline{\theta}) = 0\right\},$$

where the positive invariance of $\mathcal{I}$ is incorporated. Next, the set of solutions that satisfy $\dot{V}(\overline{r},\overline{\theta}) = 0$ is characterized, i.e., the set of non-zero amplitude equilibria

$$\nabla_{\overline{r}_j} V\left(\overline{r},\overline{\theta}\right) = 0;\ \frac{1}{\overline{r}_j^2}\nabla_{\overline{\theta}_j} V\left(\overline{r},\overline{\theta}\right) = 0\,, \tag{2.50}$$

which, by using (2.40) and (2.48), can be compactly written as:

$$H + C\overline{r} = 0;\ S\overline{r} = 0\,, \tag{2.51}$$

where the entries of H, C and S are given by:

$$\begin{aligned}&\Big[H\Big]_j = \ \overline{h}(\overline{r}_j) - \tfrac{N}{2}\overline{r}_j\ \ ,\ \Big[C\Big]_{j\ell} = \tfrac{1}{2}\cos(\overline{\theta}_{jl}),\\ &\Big[S\Big]_{j\ell} = \tfrac{1}{2}\sin(\overline{\theta}_{jl}).\end{aligned} \tag{2.52}$$

Notice that S is a null matrix when $\overline{\theta}_{jk} = m\pi\ \forall j,k\ \in \mathcal{N}, m\ \in\ \mathbb{Z}$. So, one set of solutions is represented by (2.46).

Now, let us consider the case when S is not a null matrix and establish that (2.45) describes such solutions. Observe that when S is not a null matrix, then S and C have the same null space over the field of reals, the proof of this was suggested to me by Dr. Darij Grinsberg and Dr. Robert Israel on MathOverflow. We will return to this interesting property in Chapter 4 when the stability of interleaved solutions are discussed.

Lemma 4. *Consider the matrices C and S defined in* (2.52)*. Further, assume that the S is not a null matrix, i.e.,$\overline{\theta}_{jk} \neq m\pi, \forall j,k \in \mathcal{N}, m \in \mathbb{Z}$. Then, the null spaces of C and S (over*

the field of reals) are identical.

Proof. Define matrix $E = C + \jmath S$. Since E is a outer product of $z_0 z_0^{\mathrm{H}}$ (and therefore rank 1) where z_0 is a complex vector with entries $\mathrm{e}^{\jmath\overline{\theta}_j}$ and therefore $\mathrm{Ker}(E) = \mathrm{Ker}(z_0^{\mathrm{H}})$ (using the positivity of the inner product). Therefore,

$$\begin{aligned}\mathrm{Ker}_{\mathbb{R}}(E) &= \mathrm{Ker}_{\mathbb{R}}\left(z_0^H\right)\\ &= \left\{v \in \mathbb{R}^N : z_0^{\mathrm{H}} v = 0\right\}\\ &= \Bigg\{[v_1, v_2, \ldots, v_N]^{\mathrm{T}} \in \mathbb{R}^N : \sum_{j=1}^{N}(\cos\overline{\theta}_j)v_j = 0\,,\\ &\qquad \sum_{j=1}^{N}(\sin\overline{\theta}_j)v_j = 0\Bigg\}.\end{aligned}$$

This is the intersection of two hyperplanes in $\mathbb{R}^N$. Since the cases when $\overline{\theta}_{jk} = m\pi, m \in \mathbb{Z}$ are excluded, the hyperplanes are distinct (hyperplanes are coincident when $\tan\overline{\theta}_j = \tan\overline{\theta}_k\, \forall j,k \in \mathcal{N}$) and thus $\mathrm{Ker}_{\mathbb{R}}(E)$ is an $(N-2)$-dimensional real subspace of $\mathbb{R}^N$. From $E = C + \jmath S$, $\mathrm{Ker}_{\mathbb{R}}(E) = \mathrm{Ker}_{\mathbb{R}}(C) \cap \mathrm{Ker}_{\mathbb{R}}(S)$. If all the three kernels involved are $N-2$-dimensional, then this yields that $\mathrm{Ker}_{\mathbb{R}}(E) = \mathrm{Ker}_{\mathbb{R}}(C) = \mathrm{Ker}_{\mathbb{R}}(S)$. By using the fact that for square matrices, X and Y, $\mathrm{rank}(X+Y) \leq \mathrm{rank}(X) + \mathrm{rank}(Y)$, $S = (E - E^{\mathrm{H}})/2\jmath$ and $C = (E + E^{\mathrm{H}})/2\jmath$ have rank at most 2 ; to show the three kernels involved are $N-2$-dimensional, it suffices to show that $\mathrm{rank}(C)$ and $\mathrm{rank}(S)$ are greater than 2. Choose $m < n$ satisfying $\sin(\overline{\theta}_{mn}) \neq 0$ (by assumption) and then observe that the determinants of $(\{m,n\},\{m,n\})$-minors of C and S are greater than zero. Since the rank of a matrix is the largest order of any non-zero minor and there exists a second order minor which is nonzero, the rank is at least 2. Thus, the nullspace of C and S are identical when S is not a null matrix. □

Thus, (2.51) effectively reduces to:

$$H = 0,\ S\overline{r} = 0\,. \tag{2.53}$$

Observe that $H = 0$ ensures that equilibrium radii are identical, given by ρ which satisfies

$$\overline{h}(\rho) = \frac{N}{2}\rho\,. \tag{2.54}$$

Incorporating identical radii, $S1_N = 0$ which implies $C1_N = 0$ (as they have identical null spaces) and therefore:

$$e^{\jmath\overline{\theta}_j} \sum_{k=1}^{N} \left(e^{-\jmath\overline{\theta}_k} \right) = 0 \ \forall j \in \mathcal{N}, \tag{2.55}$$

which gives the phase-balanced state set $\mathcal{S}$. Thus, all such trajectories, where $\overline{\theta}_{jk} \neq m\pi, m \in \mathbb{Z}, \ \forall j,k \in \mathcal{N}$, originating in $\mathcal{I}$ converge to $\mathcal{S}$. Thus, the dynamics either converge to $\mathcal{S}$ (2.45) or $\mathcal{S}'$ (2.46). □

Recall that $\mathcal{S} \cap \mathcal{S}'$ is not necessarily empty. When the number of oscillators are even and the number of oscillators in each of phase-synchronized clusters in $\mathcal{S}'$ are equal then such equilibria belong to $\mathcal{S}$ as well. (See Fig. 2.6.) As we are interested in the asymptotic convergence to the phase-balanced states, the equilibria that belong to $\mathcal{S}'$ but not to $\mathcal{S}$ are shown to be locally unstable and thus almost all trajectories in $\mathcal{I}$ converge to the phase-balanced state set.

2.2.3 Local Instability of Solutions

Now, the focus is on the set of solutions described by $\mathcal{S}'$ (2.46), of which the phase synchronized solutions, $\mathcal{S}''$ (2.47), are a special case and have been widely studied in the context of Liénard-type oscillators [24]. The chosen feedback makes these equilibria locally unstable if they do not lie in $\mathcal{S}$. The following theorem establishes the result.

Theorem 5. *Equilibria of* (2.40) *that reside in the set* $\mathcal{S} \setminus \mathcal{S}'$ *are unstable. Consequently, phase-synchronized solutions that lie in the set* $\mathcal{S}''$ *are also unstable.*

Proof. Linearizing (2.40) around the equilibria in $\mathcal{S}'$:

$$J' = \left[\begin{array}{c|c} J'_{\mathrm{A}} & 0_N \\ \hline 0_N & J'_{\mathrm{D}} \end{array}\right]. \tag{2.56}$$

The entries of J'_{A}, J'_{B}, J'_{C}, and J'_{D} are specified as:

$$\left[J'_{\mathrm{A}}\right]_{j\ell} = \begin{cases} \varepsilon \left(\frac{d\overline{h}_j}{r_j}(\rho_j) + \frac{N-1}{2} \right) & \text{if } j = \ell \\ 0 & \text{if } j \neq l \end{cases}$$

$$\left[J'_{\mathrm{D}}\right]_{j\ell} = \begin{cases} -\sum_{\ell=1,\ell\neq j}^{N} [J'_{\mathrm{D}}]_{j\ell} & \text{if } j = \ell \\ -\frac{\varepsilon}{2} & \text{if } j \neq l \ \& \ \overline{\theta}_{j\ell} = 2m\pi \\ \frac{\varepsilon}{2} & \text{if } j \neq l \ \& \ \overline{\theta}_{j\ell} = (2m+1)\pi \end{cases}$$

where $m \in \mathbb{Z}$ and ρ_j is the equilibrium radius for the jth oscillator. Since J' is block diagonal, therefore its eigenvalues are eigenvalues of J'_{A} and J'_{D}. In the following, the analysis is focused on the definiteness properties of the symmetric submatrix J'_{D} associated with the angle dynamics. Recall that for the bi-cluster synchronous set, the oscillators belong to one of the two clusters on the circle (see Fig. 1) which differ in phase π (depending on the fact that the phase-differences are odd or even multiples of π). The subsequent analysis can be divided into three cases:

i) The sizes of the two clusters differ by more than one: The diagonal entries J'_{D} corresponding to the bigger cluster are positive, and since $e_j^{\mathrm{T}} J'_{\mathrm{D}} e_j > 0$ (j is index of the node in the bigger cluster), it is not negative semidefinite, therefore J'_{D} must have at least one positive eigenvalue [73]. Therefore, the solutions that lie in (2.46) such that the sizes of the synchronized clusters (that are π apart) differ by more than one are unstable.

ii) The sizes of the clusters differ by one: The diagonal entries are either 0 (for the nodes in the bigger cluster) or -2 (for the nodes in the smaller cluster). Thus, there exists a symmetric principal minor of order 2 (corresponding to two nodes in distinct clusters) of the form

$$\frac{\varepsilon}{2} \cdot \begin{bmatrix} 0 & \pm 1 \\ \pm 1 & -2 \end{bmatrix}$$

which features a positive eigenvalue. Therefore J'_{D} cannot be negative semi-definite [73].

iii) The size of both the clusters are the same: The solution also belongs to the phase-balanced set, $\mathcal{S}$. □

Corollary 1 (Main result). *Consider the collective motion of the N networked oscillators, with the dynamics of each described by the flow* (2.40)*. Then, for almost all initial conditions $(\overline{r}_0, \overline{\theta}_0) \in \mathcal{I}$, the trajectories converge to the phase-balanced set $\mathcal{S}$* (2.45)*.*

Chapter 3

Virtual Oscillator Control for Inverters

An islanded inverter-based microgrid is a collection of heterogeneous DC energy resources, e.g., photovoltaic (PV) arrays, fuel cells, and energy-storage devices, interfaced to an AC electric distribution network and operated independently from the bulk power system. Energy conversion is typically managed by semiconductor-based power-electronic voltage-source inverters. The goal of decentralized real-time control is to regulate the inverters' terminal-voltage amplitude and frequency to realize a stable power system while achieving a fair and economic sharing of the network load.

The vast majority of academic and industrial efforts approaches the real-time control challenge by means of *droop control* [74–77]. Drawing from the control of synchronous generators in bulk power systems, droop control linearly trades off the active and reactive power injection with the inverters' terminal-voltage amplitude and frequency. In this chapter, the focus is on a communication-free decentralized control strategy wherein islanded inverters are regulated to mimic the dynamics of nonlinear limit-cycle oscillators [17, 20–22]. This method is inspired by synchronization phenomena in complex networks of coupled oscillators, and is termed *Virtual Oscillator Control* (VOC). In general, VOC is executed by programming nonlinear differential equations of limit-cycle oscillators onto inverters' microcontrollers, and utilizing pertinent sinusoidally varying oscillator dynamic states to construct the pulse-width modulation (PWM) control signal. It is worth emphasizing that VOC constitutes a *time-domain* approach and stabilizes arbitrary initial conditions to a sinusoidal steady state. As such, it is markedly different from droop control which operates on phasor quantities and presumes the existence of a quasi-stationary AC steady state; see Fig. 3.1.

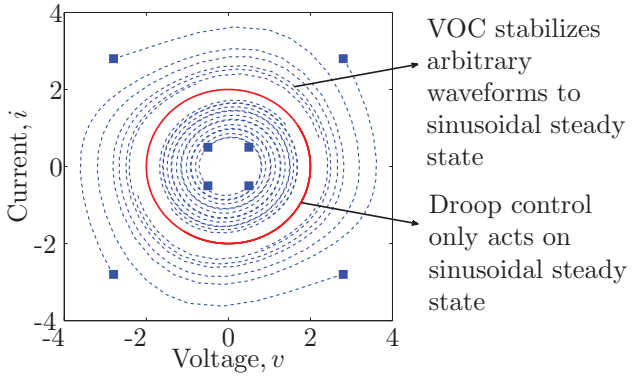

Figure 3.1: VOC stabilizes arbitrary initial conditions to a sinusoidal steady state, while droop control acts on phasor quantities; only well defined in the sinusoidal steady state. (Source: [26])

See also [18, 78] for similar time-domain control strategies.

Extending the previous efforts in [17, 20–22] where the work was focused on deadzone oscillators, here, the voltage dynamics of power-electronic inverters is investigated when they are controlled to emulate the dynamics of Van der Pol oscillators (essentially, smooth cubic polynomial realizations of deadzone oscillators). Unless stated otherwise, in subsequent discussions where VOC is referenced, it is implied that the control strategy is implemented with Van der Pol oscillators; also, inverters controlled with this approach are termed virtual-oscillator controlled (VO-controlled) inverters. Coupled Van der Pol oscillators tend to synchronize without any external forcing [34, 79], and hence utilizing them as virtual oscillators for inverter control is an effective strategy for realizing a stable AC microgrid.

The work provides two main contributions: First, a correspondence is established between VOC and droop control by obtaining conditions under which the respective voltage dynamics at the inverter terminals—close to the sinusoidal steady state—are identical. To bridge the temporal gap between droop control and VOC, the periodic nonlinear oscillator dynamics to focus on AC-cycle time scales is averaged [80]. In addition to yielding insightful circuit-theoretic interpretations for droop control, the analysis highlights the choice of design parameters that ensure VO-controlled inverters mimic the behavior of droop-controlled inverters close to the quasi-stationary sinusoidal steady state and vice versa (see Fig. 3.1), which allows to leverage insights on the optimal choice of droop coefficients [81] to design VO-controlled inverters that achieve load sharing or economic optimality in steady state.

The second contribution here is to demonstrate the convergence of the averaged terminal-voltage amplitude and phase dynamics of VO-controlled inverters in resistive networks using a gradient-sytem formulation in concert with LaSalle's invariance principle. Under a set of non-restrictive decoupling assumptions on the phase and amplitude dynamics—valid in

unstressed networks with a nearly uniform voltage profile and approximately equal phase angles [74, 82–86]— sufficient conditions are also presented for local exponential stability of potentially desirable equilibria of the linearized and averaged VO-controlled inverter dynamics.

Within the realm of analytical approaches that investigate stability and synchronization in this application domain, for the deadzone type oscillators and parallel-connected inverters considered in [17, 20–22], small-gain type arguments were utilized to prove synchronization; these results were generalized in terms of oscillator type and network topology recently in [54] by leveraging structural and spectral properties of a network reduction procedure called Kron reduction [55]. Related work in [18, 78] employed similar arguments based on incremental passivity. From a dynamical systems perspective, a connection is established between limit-cycle oscillators (VO-controlled inverters) and phase oscillators (droop-controlled inverters) by means of coordinate transformations and averaging. For Van der Pol oscillators, similar connections and synchronization analyses date back to [79] and have recently been surveyed in the tutorial [46]. Additionally, averaging methods have recently been applied to study synchronization in Liénard-type oscillators [87], which include Van der Pol oscillators as a particular case. It is also worth mentioning that similar averaging methods have been applied to extract small-signal state-space models for DC-DC power-electronic converters [88–92]. Finally, it is worth pointing out that the averaging analysis adopted here applies to general planar Liénard-type limit-cycle oscillators which include Van der Pol oscillators as a particular case [27].

Related to this work, for droop-controlled inverters in radial lossless microgrids under the assumption of constant voltage amplitudes, analytic conditions for proportional power sharing and synchronization have recently been derived by applying results from the theory of coupled oscillators in [81, 93]. Conditions for voltage stability for a lossless parallel microgrid with one common load have been derived in [94]. A decentralized linear matrix inequality-based control design for guaranteeing network stability considering variable voltage amplitudes and phase angles for meshed networks while accounting for power sharing has been described in [95].

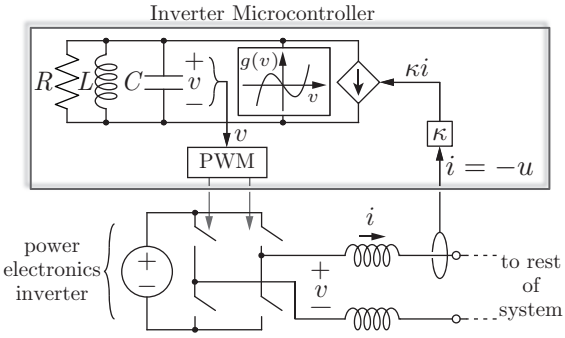

Figure 3.2: Implementation of VOC for a single-phase power-electronic inverter. The Van der Pol oscillator is composed of a parallel RLC circuit, and a nonlinear voltage-dependent current source, $g(v)$. The capacitor voltage is utilized as the PWM modulation signal. (Source: [26])

3.1 Correspondence between Droop Control and VOC for Inverter Control

In this section, the droop coefficients are derived under which the dynamics of droop control match VOC. A brief overview of droop control and VOC is provided next. For the ease of exposition, the particular case of VOC implementation with Van der Pol oscillator is considered, it can be easily extended to the class of Liénard-type oscillators and a remark has been included to that effect.

3.1.1 Droop control

For resistive networks, droop control linearly trades off frequency deviation versus reactive-power; and inverter terminal-voltage amplitude versus active-power [75, 96]:

$$\frac{d}{dt}\overline{\theta}_j = n_j\left(\overline{Q}_j - \overline{Q}_j^*\right), \quad \overline{r}_j - \overline{r}_j^* = m_j\left(\overline{P}_j^* - \overline{P}_j\right), \tag{3.1}$$

where $\overline{Q}_j^*$ and $\overline{P}_j^*$ are the per-phase average reactive-power and active-power setpoints, respectively; $\overline{r}_j^*$ is the terminal-voltage-amplitude setpoint; and $n_j, m_j \in \mathbb{R}_{>0}$ are reactive-power and active-power droop coefficients, respectively. As expressed in (3.1), assume that the droop laws are executed with AC-cycle averages of active and reactive power. To preserve the generality of the ensuing discussions, the dynamics of additional low-pass filters, voltage controllers, and current controllers in experimental implementations [76] are disgarded; however, these could be included in the analysis readily.

3.1.2 VOC implemented with a Van der Pol Oscillator

Consider the Van der Pol oscillator to constitute the virtual oscillator circuit for inverter control as shown in Fig. 3.8. The circuit implementation is composed of a parallel RLC circuit and a nonlinear voltage-dependent current source, $g(\cdot)$. In the scaled time coordinates $\tau = t/\sqrt{LC}$, the dynamics of the oscillator are captured by the following:[1]

$$\ddot{v} - \sqrt{\frac{L}{C}}\left(\sigma - \frac{1}{R}\right)\left(1 - \frac{3k}{(\sigma - \frac{1}{R})}v^2\right)\dot{v} + v = \kappa\sqrt{\frac{L}{C}}\dot{u}(\tau), \tag{3.2}$$

where $u(\tau)$ is the current input to the Van der Pol oscillator (see Fig. 3.8), and κ is the *current gain*. In particular, the inverter output current is scaled by κ, and this is extracted from the Van der Pol oscillator that forms the inverter controller. The system in (3.2) can be compactly written as

$$\ddot{v} - \varepsilon\alpha\big(1 - \beta v^2\big)\dot{v} + v = \kappa\varepsilon\dot{u}(\tau)\,, \tag{3.3}$$

by defining the following parameters:

$$\varepsilon := \sqrt{\frac{L}{C}}, \quad \alpha := \sigma - \frac{1}{R}, \quad \beta := \frac{3k}{(\sigma - \frac{1}{R})}. \tag{3.4}$$

With this notation in place, the nonlinear voltage-dependent current source is a cubic polynomial, $g(v) = v - \beta(v^3/3)$ (see Fig. 3.8). Liénard's condition [34] for ensuring a stable limit cycle in the system (3.3) requires positive damping at the origin, i.e., $\alpha = \sigma - 1/R > 0$. In the so-called quasi-harmonic limit, i.e., $\varepsilon \searrow 0$, the model (3.3) reduces to a forced harmonic oscillator with unit frequency. In the original time scale $t = \tau\sqrt{LC}$, this natural frequency of oscillation is $1/\sqrt{LC}$. By standard regular perturbation arguments [80, Theorem 10.1], this correspondence can also be made for ε sufficiently small. Subsequently, $\omega := 1/\sqrt{LC}$.

Begin by establishing a state-space model in Cartesian coordinates; choosing a scaled version of the inductor current and capacitor voltage as states, $x := \varepsilon i_L$, and $y := v$,

$$\dot{x} = y, \quad \dot{y} = -x + \varepsilon\alpha g(y) + \varepsilon\kappa u(\tau). \tag{3.5}$$

Next, transform the model (3.5) to polar coordinates by defining $x = r\sin(\phi)$ and $y =$

[1] For notational simplicity, the subscript is dropped from electrical quantities and parameters that indexes the inverter in this section.

$r\cos(\phi)$ and recover the following dynamics in polar coordinates:[2]

$$\begin{aligned}\dot{r} &= \varepsilon\left(\alpha g\big(r\cos(\phi)\big) + \kappa u(\tau)\right)\cos(\phi),\\ \dot{\phi} &= 1 - \varepsilon\left(\frac{\alpha}{r} g\big(r\cos(\phi)\big) + \frac{\kappa u(\tau)}{r}\right)\sin(\phi).\end{aligned} \tag{3.6}$$

In ensuing discussions, (3.38) written in the original time coordinates shall be used, with the nominal frequency of oscillation, $\omega = 1/\sqrt{LC}$, and phase offset as defined in (**??**):

$$\begin{aligned}\frac{dr}{dt} &= \frac{1}{C}\left(\alpha g\big(r\cos(\omega t+\theta)\big) + \kappa u(t)\right)\cos(\omega t+\theta),\\ \frac{d\theta}{dt} &= \omega - \left(\frac{\alpha}{rC} g\big(r\cos(\omega t+\theta)\big) + \frac{\kappa u(t)}{rC}\right)\sin(\omega t+\theta).\end{aligned} \tag{3.7}$$

Remark 1 (Controller implementation)**.** Essentially, (3.7), (3.1) describe the controller dynamics of the per-phase equivalent circuit at the inverter terminals; the signal $v = y = r\cos(\phi)$ can be utilized for control of single-phase inverters [17] (Fig. 3.8). For three-phase settings, a balanced set of PWM modulation signals, $m_{\rm a}, m_{\rm b}, m_{\rm c}$ are obtained as follows:

$$\begin{bmatrix} m_{\rm a}\\ m_{\rm b}\\ m_{\rm c}\end{bmatrix} = \Sigma^{\rm T}\begin{bmatrix} r\cos(\phi)\\ r\sin(\phi)\end{bmatrix}, \quad \Sigma := \begin{bmatrix} 1 & -\frac{1}{2} & -\frac{1}{2}\\ 0 & \frac{\sqrt{3}}{2} & -\frac{\sqrt{3}}{2}\end{bmatrix}. \tag{3.8}$$

The matrix Σ implements a coordinate transformation from polar to abc coordinates [21,97]. □

3.1.3 Uncovering Droop Laws in Averaged VOC Dynamics

Consider two microgrids, each with N identical inverters, identical network configurations and loads. All inverters in one microgrid are controlled with VOC (3.7), and the inverters in the other are controlled with droop control (3.1). For the jth inverter, denote the difference in voltage amplitudes and phase offsets in the two inverter-control strategies by

$$e_r(t) = \bar{r}_j - r_j(t), \quad e_\theta(t) = \bar{\theta}_j(t) - \theta_j(t) \tag{3.9}$$

[2]This bijective change of coordinates is well defined (and leads to smooth dynamics) whenever $r \neq 0$ or equivalently $[x, y]^{\rm T} \neq 0$. Theorem 7 establishes well-posedness conditions focused on convergence of the amplitude dynamics to an equilibrium that excludes the origin.

where $\bar{r}_j$ and $\bar{\theta}_j(t)$ are the amplitudes and phases as used in droop control (3.1), and $r_j(t)$ and $\theta_j(t)$ those in VOC (3.7).

In the following, how the droop laws and coefficients should be designed is analyzed so that the difference in the phase dynamics and steady-state equilibrium voltage profile of the two sets of inverters (controlled with VOC and droop) is of order $\mathcal{O}(\varepsilon) = \mathcal{O}(\sqrt{L/C})$. To bridge the time-scale separation between VOC (that is implemented in real-time) and droop control (that presumes the existence of a quasi-stationary sinusoidal steady state), average the VOC dynamics (3.7) (a detailed derivation is provided in Step 1 of the proof to Theorem 6 below) to arrive at the following description:

$$\frac{d}{dt}\overline{r}_j = \frac{\alpha}{2C}\left(\overline{r}_j - \frac{\beta}{4}\overline{r}_j^3\right) - \frac{\kappa_j}{C\overline{r}_j}\overline{P}_j, \tag{3.10a}$$

$$\frac{d}{dt}\overline{\theta}_j = +\frac{\kappa_j}{C\overline{r}_j^2}\overline{Q}_j. \tag{3.10b}$$

The averaged VOC dynamics (3.10) enable us to compare the droop control laws in (3.1) with VOC (3.7).

Theorem 6 (**Correspondence between Droop Control and VOC).** *Consider two identical microgrids where all inverters in one microgrid are controlled with VOC* (3.7)*, and the inverters in the other are droop controlled* (3.1)*. Assume*

(A1) unique solutions to the droop-controlled system (3.1) *and the averaged VOC system* (3.10) *exist in a time interval $t \in [0, t^*]$ of strictly positive length.*

(A2) the average active power delivered by the jth inverter in sinusoidal steady state, $\overline{P}_{j,\mathrm{eq}}$, is bounded as

$$0 < \kappa_j \overline{P}_{j,\mathrm{eq}} < \frac{\alpha}{2\beta}, \tag{3.11}$$

so that the average VOC dynamics (3.10) *admit a nonnegative amplitude equilibrium $\overline{r}_{j,\mathrm{eq}}$.*

(A3) both the VO-controlled microgrid (3.7) *and the droop-controlled microgrid* (3.1) *operate in steady state and the initial signal differences are of order $\varepsilon = \sqrt{L/C}$:*

$$e_r(0) \approx \mathcal{O}(\varepsilon) \quad \text{and} \quad e_\theta(0) \approx \mathcal{O}(\varepsilon).$$

Suppose the frequency-droop coefficient is picked as

$$n_j = \frac{\kappa_j}{\overline{r}_{j,\mathrm{eq}}^2 C}\,, \tag{3.12}$$

and the average reactive-power setpoint is set to zero, $\overline{Q}_j^* = 0$. *Suppose the voltage-droop coefficient is picked as*

$$m_j = -\kappa_j \left(\alpha \left(\overline{r}_{j,\mathrm{eq}} - \frac{\beta}{2}\overline{r}_{j,\mathrm{eq}}^3\right)\right)^{-1}\,, \tag{3.13}$$

and the average active-power and amplitude setpoints are picked as $\overline{P}_j^* = \overline{P}_{j,\mathrm{eq}}$ *and* $\overline{r}_j^* = \overline{r}_{j,\mathrm{eq}}$. *Then, there exists an* ε^*, *such that for all* $0 < \varepsilon < \varepsilon^*$, *for all* $t \in [0, t^*]$

$$e_r(t) \approx \mathcal{O}(\varepsilon) \quad \textit{and} \quad e_\theta(t) \approx \mathcal{O}(\varepsilon).$$

Assumption (A1) is guaranteed for $\overline{r}_j(0) > 0$ due to local Lipschitz continuity; (A2) can be met by design; and (A3) is necessary for comparing the two strategies using averaging techniques.

The correspondences derived in Theorem 6 are asymptotic results based on a perturbation and averaging analysis for sufficiently small $\varepsilon = \sqrt{L/C}$. However, a small ε also implies a weak (nonlinear) viscous damping in (3.3) and a slow convergence to the quasi-harmonic limit cycle. In Section 3.2.3, it is shown that the convergence rate is, in fact, inversely proportional to ε. Theorem 6 and the above discussion indicate that the droop laws (3.1) are recovered from the VOC dynamics (3.7) only on *slow* AC-cycle time scales, and when the dynamics of VO-controlled inverters are *deliberately decelerated*. Hence, on the limit cycle, the decelerated VOC subsumes droop control, but it is much faster in general. Finally, the correspondences established in (3.12) and (3.85) are formally valid only on a bounded time horizon $[0, t^*]$. The findings can be extended to an unbounded time horizon provided that the averaged system is exponentially stable [80].

Proof. The proof consists of three parts: an averaging analysis of VOC, a correspondence of the phase dynamics, and a correspondence of the steady-state voltage amplitudes.

1) Averaging the VOC dynamics: Consider the dynamics (3.3) of the VO-controlled mi-

crogrid (3.7) in the time coordinates $\tau = t/\sqrt{LC}$:[3]

$$\begin{aligned}\dot{r} &= \varepsilon\left(\alpha g\big(r\cos(\tau+\theta)\big) + \kappa u(\tau)\right)\cos(\tau+\theta),\\ \dot{\theta} &= -\varepsilon\left(\frac{\alpha}{r} g\big(r\cos(\tau+\theta)\big) + \frac{\kappa u(\tau)}{r}\right)\sin(\tau+\theta).\end{aligned} \tag{3.14}$$

Note that the dynamical systems above are 2π-periodic functions in τ. In the quasi-harmonic limit $\varepsilon \searrow 0$, apply standard averaging arguments using ε as the *small parameter*, to obtain the averaged dynamics [80]:

$$\begin{aligned}\begin{bmatrix}\dot{\overline{r}}\\ \dot{\overline{\theta}}\end{bmatrix} &= \frac{\varepsilon}{2\pi}\int_0^{2\pi} \alpha g\left(\overline{r}\cos(\tau+\overline{\theta})\right)\begin{bmatrix}\cos(\tau+\overline{\theta})\\ -\frac{1}{\overline{r}}\sin(\tau+\overline{\theta})\end{bmatrix} d\tau\\ &\quad + \frac{\varepsilon}{2\pi}\int_0^{2\pi} \kappa u(\tau)\begin{bmatrix}\cos(\tau+\overline{\theta})\\ -\frac{1}{\overline{r}}\sin(\tau+\overline{\theta})\end{bmatrix} d\tau\\ &= \varepsilon\alpha\begin{bmatrix}\frac{\overline{r}}{2} - \beta\frac{\overline{r}^3}{8}\\ 0\end{bmatrix} + \frac{\varepsilon}{2\pi}\int_0^{2\pi}\kappa u(\tau)\begin{bmatrix}\cos(\tau+\overline{\theta})\\ -\frac{1}{\overline{r}}\sin(\tau+\overline{\theta})\end{bmatrix} d\tau.\end{aligned} \tag{3.15}$$

The last line in (3.15) follows from

$$\begin{aligned}&-\frac{\varepsilon}{2\pi\overline{r}}\int_0^{2\pi}\alpha g\left(\overline{r}\cos(\tau+\overline{\theta})\right)\sin(\tau+\overline{\theta})d\tau\\ &= \frac{\alpha\varepsilon}{2\pi}\left(\left[\frac{1}{4}\cos(2\tau+2\overline{\theta})\right]_0^{2\pi} + \frac{\beta\overline{r}^2}{3}\left[\cos^4(\tau+\overline{\theta})\right]_0^{2\pi}\right) = 0.\end{aligned}$$

Transitioning (3.15) from τ to t coordinates,

$$\begin{bmatrix}\frac{d\overline{r}}{dt}\\ \frac{d\overline{\theta}}{dt}\end{bmatrix} = \frac{\alpha}{C}\begin{bmatrix}\frac{\overline{r}}{2} - \beta\frac{\overline{r}^3}{8}\\ 0\end{bmatrix} + \frac{\kappa\omega}{2\pi C}\int_0^{\frac{2\pi}{\omega}} u(t)\begin{bmatrix}\cos(\omega t+\overline{\theta})\\ -\frac{1}{\overline{r}}\sin(\omega t+\overline{\theta})\end{bmatrix} dt.$$

From Fig. 3.8 recognize that the current sourced by the Van-der-Pol oscillator is $i(t) = -u(t)$,

$$\begin{aligned}\begin{bmatrix}\frac{d\overline{r}}{dt}\\ \frac{d\overline{\theta}}{dt}\end{bmatrix} &= \frac{\alpha}{C}\begin{bmatrix}\frac{\overline{r}}{2} - \frac{\beta\overline{r}^3}{8}\\ 0\end{bmatrix} + \frac{\kappa\omega}{2\pi C}\int_0^{\frac{2\pi}{\omega}}\begin{bmatrix}-i(t)\cos(\omega t+\overline{\theta})\\ \frac{i(t)}{\overline{r}}\sin(\omega t+\overline{\theta})\end{bmatrix} dt\\ &= \frac{\alpha}{C}\begin{bmatrix}\frac{\overline{r}}{2} - \frac{\beta\overline{r}^3}{8}\\ 0\end{bmatrix} + \frac{\kappa\omega}{2\pi C}\int_0^{\frac{2\pi}{\omega}}\begin{bmatrix}-\frac{i(t)\overline{r}}{\overline{r}}\cos(\omega t+\overline{\theta})\\ \frac{i(t)\overline{r}}{\overline{r}^2}\sin(\omega t+\overline{\theta})\end{bmatrix} dt.\end{aligned} \tag{3.16}$$

[3]For notational simplicity, the subscript j is dropped from the variables $[r,\theta]^{\mathrm{T}}, [\overline{r},\overline{\theta}]^{\mathrm{T}}, \kappa, i, u$, indexing the jth inverter in equations (3.14)-(3.16).

Recalling the instantaneous and average active and reactive power definitions respectively, observe that the averaged dynamics in (3.16) are given by (3.10) (For details, see Appendix A).

Under assumptions (A1), (A2), and (A3), by standard averaging arguments [80, Theorem 10.4], there exists an ε_1^* sufficiently small so that for all $0 < \varepsilon < \varepsilon_1^*$, the solution of the averaged VOC dynamics (3.10) is $\mathcal{O}(\varepsilon)$ close to the solution of the original VOC dynamics (3.7) for times $t \in [0, t^*/\varepsilon]$. Next, the averaged VOC system (3.10) is compared with the droop control system (3.1).

2) Correspondence of phase dynamics: The VOC system (3.7) is assumed to evolve in quasi-stationary sinusoidal steady state with a small initial (at time $t = 0$) $\mathcal{O}(\varepsilon)$ difference from the harmonic droop signals. Recall that in the quasi-harmonic limit, there exists an ε_2^* sufficiently small so that for all $0 < \varepsilon < \varepsilon_2^*$, the solution of the VOC dynamics (3.7) is $\mathcal{O}(\varepsilon)$ close to the solution of a harmonic oscillator with radius $\overline{r}_{j,\mathrm{eq}}$ for $t \in [0, t^*]$; see [46, 80]. In particular, for $t \in [0, t^*]$, the solution $\overline{\theta}_j(t)$ of the averaged phase dynamics (3.10b) is $\mathcal{O}(\varepsilon)$ close to the solution of

$$\frac{d}{dt}\overline{\theta}_j = \frac{\kappa_j}{C\overline{r}_{j,\mathrm{eq}}^2}\overline{Q}_j\,,$$

where the amplitude dynamics (3.10a) is disregarded, and replaced $\overline{r}_j(t)$ in (3.10b) by $\overline{r}_{j,\mathrm{eq}}$ (whose closed form is discussed below).

For the following arguments, let $0 \leq \varepsilon \leq \min\{\varepsilon_1^*, \varepsilon_2^*\}$. Observe that the phase dynamics of a droop-controlled inverter (3.1) correspond with the AC-cycle-averaged dynamics of a VO-controlled inverter (3.7)—up to an order $\mathcal{O}(\varepsilon)$ mismatch—if the reactive-power setpoint is chosen, $\overline{Q}_j^*$, and the frequency-droop coefficient, n_j, as follows:

$$\overline{Q}_j^* = 0, \quad n_j = \frac{\kappa_j}{\overline{r}_{j,\mathrm{eq}}^2 C}. \tag{3.17}$$

3) Correspondence of amplitude dynamics: Next, consider the amplitude dynamics (3.10a) and its equilibrium terminal-voltage profile. For the network of VO-controlled inverters, the steady-state voltage profile is recovered from the solution of the following N nonlinear equations:

$$0 = \frac{\alpha}{2C}\left(\overline{r}_{j,\mathrm{eq}} - \frac{\beta}{4}\overline{r}_{j,\mathrm{eq}}^3\right) - \frac{\kappa_j \overline{P}_{j,\mathrm{eq}}}{C\overline{r}_{j,\mathrm{eq}}}, \quad \forall j = 1, \ldots, N. \tag{3.18}$$

By rearranging terms in (3.42), get the following power-balance condition for the jth inverter

$$\frac{\alpha\beta}{8}\overline{r}_{j,\mathrm{eq}}^4 - \frac{\alpha}{2}\overline{r}_{j,\mathrm{eq}}^2 + \kappa_j \overline{P}_{j,\mathrm{eq}} = 0. \tag{3.19}$$

The positive roots of the above equation are given by

$$\overline{r}_{j,\mathrm{eq}} = \left[\frac{2\alpha \pm 2\sqrt{\alpha^2 - 6k\kappa_j \overline{P}_{j,\mathrm{eq}}}}{3k}\right]^{\frac{1}{2}}, \tag{3.20}$$

where $\alpha\beta = 3k$ (see (3.4)). Notice that these two roots are real-valued if and only if (3.45) holds. Around the high-voltage solution of (3.20), (denoted by $\overline{r}_{j,\mathrm{eq}}$ with a slight abuse of notation), the sensitivity of the active-power injection with respect to a change in amplitude is:

$$\kappa_j \frac{d\overline{P}_{j,\mathrm{eq}}}{d\overline{r}_{j,\mathrm{eq}}} = \alpha\left(\overline{r}_{j,\mathrm{eq}} - \frac{\beta}{2}\overline{r}^3_{j,\mathrm{eq}}\right), \quad \forall j = 1, \ldots, N. \tag{3.21}$$

Theorem 3 depicts that this high-voltage solution is exponentially stable. Equation (3.21) can be placed in correspondence with the amplitude dynamics of a droop-controlled inverter (3.1). By an analogous reasoning as for the phase dynamics, there exists an ε_3^* sufficiently small so that for all $0 < \varepsilon < \varepsilon_3^*$, the solution $\overline{r}_j(t)$ of the averaged amplitude dynamics (3.10a) satisfies—up to an $\mathcal{O}(\varepsilon)$ mismatch—the conditions of the stationary solution (3.21) (with fixed radius $\overline{r}_{j,\mathrm{eq}}$) for times $t \in [0, t^*]$.

For the following arguments, let $0 \leq \varepsilon \leq \min\{\varepsilon_1^*, \varepsilon_3^*\}$. Observe that the amplitude dynamics of a droop-controlled inverter (3.1) correspond with that of a VO-controlled inverter in (3.21)—up to an order $\mathcal{O}(\varepsilon)$ mismatch—if the active-power setpoint, $\overline{P}_j^*$, terminal-voltage setpoint, $\overline{r}_j^*$, and the voltage-droop coefficient, m_j, are chosen as follows:

$$\overline{P}_j^* = \overline{P}_{j,\mathrm{eq}},\ \overline{r}_j^* = \overline{r}_{j,\mathrm{eq}},\ m_j = -\kappa_j\left(\alpha\left(\overline{r}_{j,\mathrm{eq}} - \frac{\beta}{2}\overline{r}^3_{j,\mathrm{eq}}\right)\right)^{-1}.$$

Finally, to complete the proof, let $\varepsilon^* = \min\{\varepsilon_1^*, \varepsilon_2^*, \varepsilon_3^*\}$, and note that all arguments held for the time scales $[0, t^*/\varepsilon^*] \cap [0, t^*]$ which equals $[0, t^*]$ for ε^* sufficiently small. □

3.2 Reverse Engineering Droop Control, Convergence Rates, and Numerical Validation

Simulations in this section focus on corroborating the averaging analysis and the correspondence established with droop control. Additionally, the load-sharing capabilities afforded by VOC and implications of the quasi-harmonic limit, $\varepsilon \searrow 0$, on the VOC convergence speed are discussed.

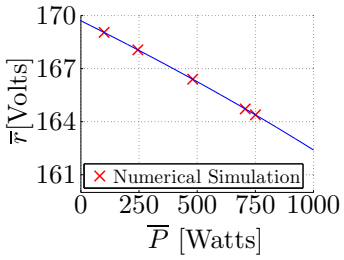

Figure 3.3: Voltage-power characteristic (3.20) for an inverter superimposed to time-domain simulations of the non-averaged nonlinear model (3.7) run out to steady state. (Source: [26])

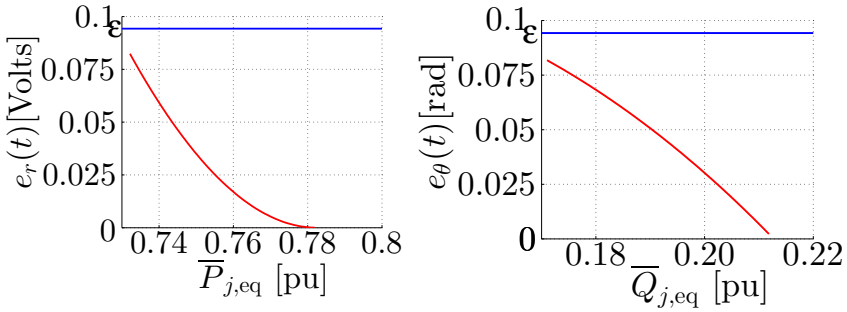

(a) (b)

Figure 3.4: Differences in: (a) equilibrium-voltages and (b) phase-offsets when comparing VOC and droop control. (Source: [26])

3.2.1 Correspondence between VOC and Droop Control

First, the averaging analysis is validated by focusing on the expression in (3.20). In particular, the voltage-regulation curve for VOC (from (3.20)) is plotted in Fig. 3.3 and the analytical expression is validated by comparison with simulations of the original nonlinear and non-averaged Van der Pol oscillator model (3.7) run out to steady state.

Next, the spotlight is turned on the correspondences established between VOC and droop control. To this end, consider a single 15 kW three-phase inverter connected to a load which draws a constant current at a lagging power factor of 0.85. Suppose a Van der Pol oscillator-based controller (parameters are listed in the Appendix) is supplying 0.78 pu active power and 0.21 pu reactive power in steady state. A corresponding droop controller is derived using the expressions in (3.12) and (3.85). Figure 3.4(a) depicts $e_r(t)$ in steady state as the active power consumed by the load is varied. Figure 3.4(b) depicts $e_\theta(t)$ recorded at time $t = 2.5$s as the reactive power consumed by the load is varied. Differences in both cases are of $\mathcal{O}(\varepsilon)$.

3.2.2 Load Sharing and Economic Optimality

Consider the microgrid setting where N inverters are connected in parallel across a balanced three-phase load. In this case, droop control (3.1) also achieves steady-state load sharing or economic optimality. For resistive networks, it is known [75, 93] that the steady-state reactive power injection $\overline{Q}_{j,\mathrm{eq}}$ from the jth inverter is proportional to its rating R_j, that is,

$$\frac{\overline{Q}_{j,\mathrm{eq}}}{R_j} = \frac{\overline{Q}_{\ell,\mathrm{eq}}}{R_\ell} \quad \forall\, j, \ell \in \{1, \ldots, N\}, \tag{3.22}$$

provided the following hold:

$$\frac{\overline{Q}_j^*}{R_j} = \frac{\overline{Q}_\ell^*}{R_\ell}, \quad n_j R_j = n_\ell R_\ell \quad \forall\, j, \ell \in \{1, \ldots, N\}.$$

Similarly, droop control can be designed to minimize an unconstrained economic dispatch of the reactive power injections

$$\min_{\{\overline{Q}_{j,\mathrm{eq}}\}_{j=1}^N} \quad \sum_{j=1}^N \lambda_j \overline{Q}_{j,\mathrm{eq}}^2, \tag{3.23}$$

with marginal costs $\lambda_i > 0$ provided the reactive-power setpoints and droop coefficients are selected as follows [81]:[4]

$$\overline{Q}_j^* = 0, \quad \frac{n_j}{\lambda_j} = \frac{n_\ell}{\lambda_\ell}, \quad \forall\, j, \ell \in \{1, \ldots, N\}. \tag{3.24}$$

The correspondences established in Theorem 6 allow us to translate these insights to the design of optimal current gains (i.e., the κ's) in VO-controlled inverters (3.2) to achieve optimality in terms of reactive-power production. In particular, leveraging (3.17), and based on (3.24), the following design achieves an optimal dispatch of reactive power generation:

$$\frac{\kappa_j}{\overline{r}_{j,\mathrm{eq}}^2 \lambda_j} = \frac{\kappa_\ell}{\overline{r}_{\ell,\mathrm{eq}}^2 \lambda_\ell}, \quad j, \ell \in \{1, \ldots, N\}. \tag{3.25}$$

Similar load-sharing conditions have been obtained for inverters controlled as deadzone oscillators where all voltage waveforms perfectly synchronize (amplitude, frequency, and

[4] Note that the two objectives (3.22) and (3.23) and the associated droop gains coincide for $R_j/\lambda_j = R_\ell/\lambda_\ell$ for all $j, \ell \in \{1, \ldots, N\}$.

phase) [17]. In particular, picking the current gains κ_j as

$$R_j\kappa_j = R_\ell\kappa_\ell, \quad \forall\, j,\ell \in \{1,\dots,N\}\,, \tag{3.26}$$

ensures that the current injections are shared proportionally [17], and thus—due to perfect synchronization of the voltage waveforms—the apparent power injections $\overline{S}_{j,\mathrm{eq}} = \overline{P}_{j,\mathrm{eq}} + \mathrm{j}\overline{Q}_{j,\mathrm{eq}}$ are shared proportionally in steady state:

$$\frac{\overline{S}_{j,\mathrm{eq}}}{R_j} = \frac{\overline{S}_{\ell,\mathrm{eq}}}{R_\ell}, \quad \forall\, j,\ell \in \{1,\dots,N\}. \tag{3.27}$$

As a consequence, the average active and reactive injections are shared, and (3.22) is recovered as a special case. Results from Theorem 6 allow us to extend load-sharing results for VO-controlled inverters from a setting with perfectly synchronized waveforms to more general frequency-synchronized waveforms. Consider the closed-form high-voltage solution for the terminal-voltage amplitude of the jth inverter in (3.20). When the oscillators are identical, the terminal-voltage amplitudes synchronize if the current gains are selected as follows:

$$\kappa_j\overline{P}_{j,\mathrm{eq}} = \kappa_\ell\overline{P}_{\ell,\mathrm{eq}}, \quad \forall j,\ell \in \{1,\dots,N\}. \tag{3.28}$$

Simulation Case Study: To demonstrate power sharing between three identical VO-controlled inverters connected in a parallel configuration with current gains $\kappa = [2 \quad 2 \quad 1]^{\mathrm{T}}$, the consider the set up shown in Fig. 3.5, where two of the inverters share 25% of the load while the third inverter provides 50% of the load. A load step is applied at $t = 1$s by doubling the active-power demand. The inverters support the load in the ratio of their ratings even after the load step.

3.2.3 Convergence Rate of a Van der Pol Oscillator

In this section, the implication of the quasi-harmonic limit $\varepsilon \searrow 0$ on the time taken to converge to the limit cycle in an open-circuited Van der Pol oscillator is established, i.e., when setting the driving term $u = 0$. From (3.38) ,

$$\frac{dr}{d\phi} = \frac{\varepsilon\alpha g\big(r\cos(\phi)\big)\cos(\phi)}{1 - \varepsilon\frac{\alpha}{r}g\big(r\cos(\phi)\big)\sin(\phi)}\,.$$

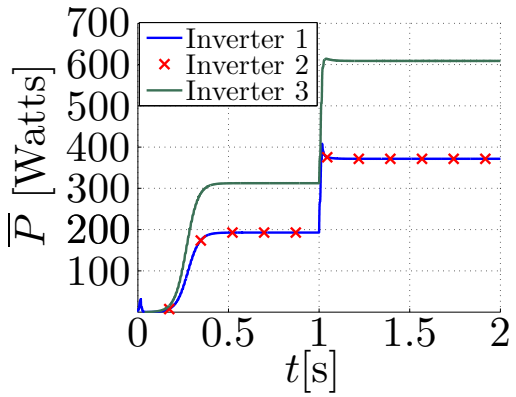

Figure 3.5: Power sharing for 3 parallel VO-controlled inverters. (Source: [26])

In the quasi-harmonic limit $\varepsilon \ll 1$, apply the series expansion $\varepsilon/(1-\varepsilon\cdot c) = \varepsilon + \mathcal{O}(\varepsilon^2)$ above to get

$$\frac{dr}{d\phi} = \varepsilon\left(\alpha g\big(r\cos(\phi)\big)\right)\cos(\phi) + \mathcal{O}(\varepsilon^2).$$

Averaging the above dynamics yields (up to $\mathcal{O}(\varepsilon^2)$ terms):

$$\frac{d\overline{r}}{d\overline{\phi}} = \frac{\alpha\varepsilon}{2}\left(\overline{r} - \frac{\beta}{4}\overline{r}^3\right). \tag{3.29}$$

Note that the locally stable equilibrium of the dynamics (3.29) is given by the open-circuit voltage, $\overline{r}_{\text{eq}} = \overline{r}^{\text{oc}}$. Integrate both sides of (3.29), arbitrarily setting the limits from $0.1\overline{r}_{\text{eq}}$ to $0.9\overline{r}_{\text{eq}}$ (without loss of generality). The arc length traced during this transition, ϕ_{s}, is given by the solution of:

$$\left[-\frac{1}{4}\log\overline{r} + \frac{1}{8}\log|4-\beta(\overline{r})^2|\right]_{0.1\overline{r}_{\text{eq}}}^{0.9\overline{r}_{\text{eq}}} = -\frac{1}{8}\varepsilon\phi_{\text{s}}.$$

Evaluating the limits of this integral, recover $\phi_{\text{s}} \approx 6\,(\varepsilon\alpha)^{-1}$, which clearly indicates that the arc length ϕ_{s} (proportional to a notion of convergence time to $\mathcal{O}(\varepsilon)$) traced before converging to the limit cycle is inversely proportional to ε. Figure 3.6 plots ϕ_{s} as a function of ε. Results from simulations of the original unforced nonlinear dynamics (3.38) (with $u = 0$) are superimposed to demonstrate validity of the above analysis. There is a fundamental trade off between harmonic content and dynamic response for the control strategy. In particular, to speed up dynamic response, a high value of ε is required; however, the amplitudes of higher-order harmonics are directly proportional to ε.

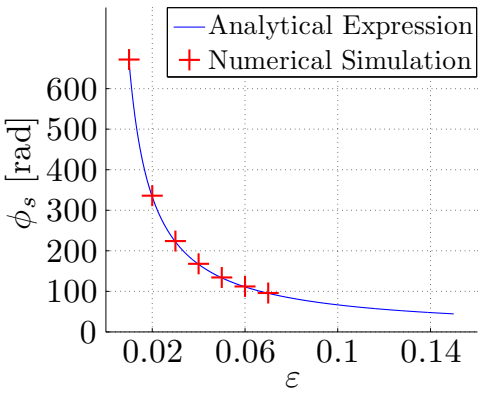

Figure 3.6: Convergence rate of a Van der Pol oscillator. (Source: [26])

3.3 Design Specifications and Parameter Selection for VO-Controlled Inverters

This section focuses on the design of virtual oscillators that underpin the control strategy, referred to as the *oscillator synthesis problem*. Inverter ac performance requirements (voltage and frequency regulation, harmonics, dynamic response) are typically specified with the aid of phasor quantities that are only valid in the quasi-stationary sinusoidal steady state. As such, given the intractability of obtaining closed-form solutions to the oscillator dynamic trajectories, from the outset it is unclear how to design the nonlinear oscillators such that the controlled inverters meet prescribed specifications. The oscillator synthesis problem is addressed with averaging- and perturbation-based nonlinear-systems analysis methods [80, 87, 98]. Leveraging the analysis in the previous section, an averaged dynamical model is used for the nonlinear oscillators that couples the real- and reactive-power outputs to the terminal-voltage dynamics of the inverter. Analyzing this averaged model in the sinusoidal steady state uncovers the voltage- and frequency-regulation characteristics of virtual-oscillator-controlled inverters. In addition, perturbation-based methods are developed that, in general, enable approximating solutions to periodic nonlinear dynamical systems when analytical closed-form solutions cannot be found. In the present setting, this analysis parameterizes the higher-order harmonic content in the inverter output as a function of the oscillator parameters, further aiding in oscillator design. The design strategy developed in this paper is summarized and illustrated in Fig. 3.7.

The contributions of this work are threefold. First, a systematic design strategy is presented to synthesize nonlinear oscillators for inverter control. The design strategy aids

in sculpting a desirable sinusoidal limit cycle that meets performance requirements specified in the lexicon of ac power systems. The proposed strategy can be conveniently applied to design controllers for inverters with different power, voltage, and current ratings; in fact, for a system of parallel-connected inverters, the proposed design strategy natively ensures power sharing in proportion to the inverter power ratings. Second, in addition to demonstrating the validity of the design strategy, the experimental results also validate the accuracy of averaging- and perturbation-based nonlinear-systems analysis methods that are ubiquitous in modeling, analysis, and control of weakly nonlinear periodic systems in application areas such as electrical power systems, circadian rhythms, and bipedal walking machines [44, 87]. With regard to power-electronics based systems, averaging methods at switching-frequency time scales have been successfully applied in prior works to extract analytically tractable models for simulation and controller design [88–92, 99].

Tangentially related to the work are previous efforts in the design of droop-controlled inverters. Particularly, there exists a wide body of literature that attempts to identify droop-control parameters that ensure inverters satisfy steady-state performance metrics and constraints such as voltage regulation, maximum frequency deviation, and proportional power sharing [75–77, 81, 100]. For the previous efforts in realizing VOC, an iterative design procedure was used involving simulation-based open-circuit and full-rated-load tests to design the virtual oscillators [17, 20, 21]. These ad-hoc design methods relied on repeated time-domain simulations to tune parameters and were not affirmed by a rigorous nonlinear-systems analysis approach. Through developing a unified and formal design methodology for VOC, this section is expected to particularly benefit practicing engineers who would be interested in implementation aspects. While this section focuses on inverter-level design, previous work has analyzed the system-level attributes of VOC. Particularly, in [17], a parallel-connected system of VO-controlled inverters was considered to derive : i) analytical conditions for global asymptotic synchronization, and ii) experimental results that demonstrate power sharing, ability to serve linear and nonlinear loads, robustness to parameter variations, and asymptotic decay of circulating currents.

A Van der Pol oscillator constitutes the virtual oscillator in this work. It is worth pointing out that the techniques outlined here can be applied to a family of weakly nonlinear limit-cycle oscillators. Subsequently, where VOC is referenced, it is implied that the control strategy is implemented with Van der Pol oscillators [34, 87]; also, inverters controlled with this approach are termed virtual-oscillator controlled (VO-controlled) inverters.

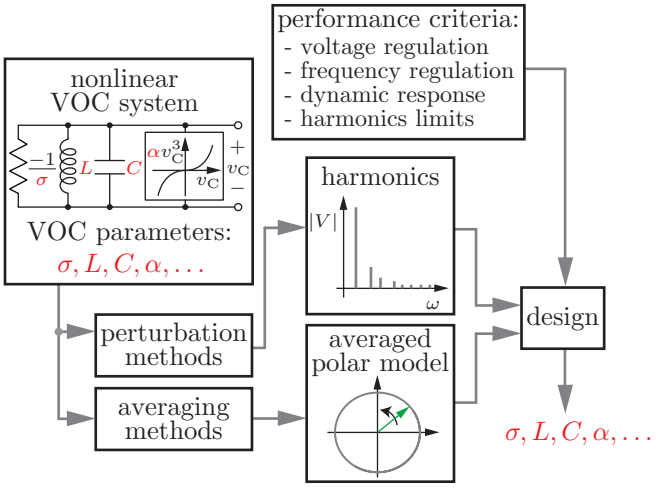

Figure 3.7: Nonlinear-systems analysis methods enable the formulation of a design strategy that relates inverter performance criteria to the oscillator circuit parameters (indicated in red). (Source: [28])

3.3.1 Controller Implementation

The controller implementation is revisited here, slight modifications are introduced such as voltage scaling along with the filtering and discretization details, to accentuate the hardware focus in the subsequent sections. The averaging derivation is repeated to reinforce the material from the previous section as well as to make the transition to design seamless. Figure 3.8 illustrates the Van der Pol VOC implementation for a single-phase inverter. The hardware also includes an LCL filter which is utilized to reduce high-order harmonics in the inverter terminal voltage. Filter elements include the inverter-side inductor, L_{f}, the ac filter capacitor, C_{f}, and the grid-side inductor, L_{g}. The closed-loop controller is a discretized version of the Van der Pol oscillator dynamics programmed onto a digital microcontroller.

The circuit model of the Van der Pol oscillator is composed of the parallel connection of: i) a harmonic oscillator with inductance, L, and capacitance, C (yielding a resonant frequency, $\omega = 1/\sqrt{LC}$), ii) a negative-conductance element, $-\sigma$, and iii) a cubic voltage-dependent current source. The virtual capacitor voltage is denoted by v_C and the inductor current is denoted by i_L. The current consumed by the cubic voltage-dependent current source is given by αv_C^3, where α is a positive constant.

The virtual oscillator is coupled to physical electrical signals in the inverter through the voltage- and current-scaling gains, κ_{v} and κ_{i}, respectively. The inverter output current i is processed by an analog-to-digital converter (ADC), multiplied by κ_{i}, and is extracted

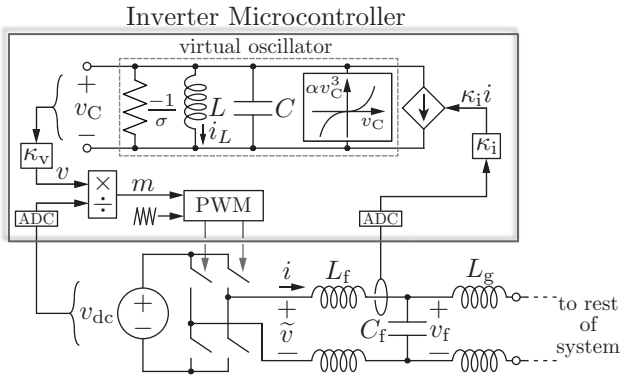

Figure 3.8: Implementation of VOC on a single-phase H-bridge inverter with an LCL output filter. The closed-loop controller is a discrete realization of the nonlinear dynamics of a Van der Pol oscillator programmed on a microcontroller. The current and voltage scalings, κ_v and κ_i, interface the virtual oscillator to the inverter. (Source: [28])

from the Van der Pol oscillator circuit. The resulting value of the VO capacitor voltage, v_C, is scaled by κ_v to produce the signal v, and this is used to construct the pulse width modulation (PWM) signal which drives the H-bridge inverter. For the single-phase inverter topology depicted in Fig. 3.8, the PWM signal, $m(t)$, is constructed as follows

$$m(t) = \frac{v(t)}{v_\mathrm{dc}}, \tag{3.30}$$

where v_dc is the dc-bus voltage. The switching period, T_sw, is much smaller than the period of the modulation signal, which in this setting is approximately $2\pi/\omega$, where ω is the resonant frequency of the LC harmonic oscillator. Consequently, the switch-cycle average of the instantaneous inverter-terminal voltage—denoted by $\widetilde{v}$ in Fig. 3.8—is approximately equal to the scaled virtual capacitor voltage, v [101]:

$$\frac{1}{T_\mathrm{sw}} \int_{s=t-T_\mathrm{sw}}^{t} \widetilde{v}(s) ds = m(t) v_\mathrm{dc} = v(t). \tag{3.31}$$

Subsequently, it is assumed that the switch-cycle-average inverter terminal voltage is equal to v, and referred to as the *inverter terminal voltage*.

With the controller description in place, next an analysis of the terminal-voltage dynamics of a VO-controlled inverter is presented. The dynamic model is leveraged to synthesize the underlying Van der Pol oscillator such that the inverter meets ac performance specifications. Without loss of generality, the focus is on real- and reactive-power ratings, voltage limits, output-current ratings, maximum frequency deviation, dynamic response, and higher-order

harmonics. A key challenge is to connect these performance specifications to the inherently nonlinear Van der Pol oscillator dynamics. The modeling approaches to establish these connections are presented next.

3.3.2 Averaged Dynamics of a VO-controlled Inverter

A derivation of the voltage- and frequency-regulation characteristics of the VO-controlled inverter is presented next, which is based on an averaging analysis of the Van der Pol oscillator dynamics.

The dynamics of the virtual-oscillator inductor current, i_L, and inverter terminal voltage, v, are given by (see Fig. 3.8)

$$\begin{aligned} L\frac{di_L}{dt} &= \frac{v}{\kappa_{\mathrm{v}}}, \\ C\frac{dv}{dt} &= -\alpha\frac{v^3}{\kappa_{\mathrm{v}}^2} + \sigma v - \kappa_{\mathrm{v}} i_L - \kappa_{\mathrm{v}}\kappa_{\mathrm{i}} i\,. \end{aligned} \tag{3.32}$$

The inverter terminal voltage is parameterized in one of the two forms below

$$v(t) = \sqrt{2}V(t)\cos(\omega t + \theta(t)) = \sqrt{2}V(t)\cos(\phi(t)), \tag{3.33}$$

where ω is the electrical frequency, $\theta(t)$ represents the phase offset with respect to ω, and $\phi(t)$ is the instantaneous phase angle. To obtain the dynamical equations that govern the evolution of the RMS-voltage, $V(t)$, and phase offset, $\theta(t)$, (or equivalently, the instantaneous phase angle, $\phi(t)$); together these would completely specify the terminal voltage at any instant, the following definitions are introduced to simplify the notation subsequently:

$$\varepsilon := \sqrt{\frac{L}{C}}, \quad g(y) := y - \frac{\beta}{3}y^3, \quad \beta := \frac{3\alpha}{\kappa_{\mathrm{v}}^2\sigma}. \tag{3.34}$$

A state-space model of the VO-controlled inverter in Cartesian coordinates aimed at recovering the RMS-voltage amplitude and instantaneous phase dynamics can be formulated with a scaled version of the inductor current and the inverter terminal voltage selected as states, $x := \kappa_{\mathrm{v}}\varepsilon i_L$, and $y := v$. With the aid of the $g(\cdot)$ and ε defined in (3.34), (3.32) can

be rewritten in the time coordinates $\tau = \omega t = (1/\sqrt{LC})t$ as follows:

$$\dot{x} = \frac{dx}{d\tau} = y, \tag{3.35}$$

$$\dot{y} = \frac{dy}{d\tau} = -x + \varepsilon\sigma g(y) - \varepsilon\kappa_{\mathrm{v}}\kappa_{\mathrm{i}} i. \tag{3.36}$$

Next, with the coordinate transformation

$$\sqrt{2}V = \sqrt{x^2 + y^2}, \quad \phi = \tan^{-1}\left(\frac{x}{y}\right), \tag{3.37}$$

applied to (3.35)-(3.36), recover the following dynamical model for the RMS terminal-voltage amplitude, V, and the instantaneous phase angle, ϕ:

$$\begin{aligned} \dot{V} &= \frac{dV}{d\tau} = \frac{\varepsilon}{\sqrt{2}}\Big(\sigma g\big(\sqrt{2}V\cos(\phi)\big) - \kappa_{\mathrm{v}}\kappa_{\mathrm{i}} i\Big)\cos(\phi), \\ \dot{\phi} &= \frac{d\phi}{d\tau} = 1 - \frac{\varepsilon}{\sqrt{2}V}\Big(\sigma g\big(\sqrt{2}V\cos(\phi)\big) - \kappa_{\mathrm{v}}\kappa_{\mathrm{i}} i\Big)\sin(\phi). \end{aligned} \tag{3.38}$$

As $\varepsilon \searrow 0$, transition to the so-called *quasi-harmonic limit*, where the (unloaded) oscillator exhibits near-sinusoidal oscillations at the resonant frequency of the LC harmonic oscillator [34]:

$$\omega = \frac{1}{\sqrt{LC}}. \tag{3.39}$$

In subsequent sections of the manuscript focused on system design, the focus is on how ε is a key design parameter that has bearing on the dynamic response and the harmonics of the system—in particular, a small value of ε ensures near sinusoidal oscillations, at the expense of a sluggish dynamic response.

As laid down in the previous section, the dynamics in (3.38) averaged over one ac cycle, $2\pi/\omega$, under the implicit assumption that $\varepsilon = \sqrt{L/C} \searrow 0$ are given by the following set of coupled nonlinear differential equations:

$$\frac{d}{dt}\overline{V} = \frac{\sigma}{2C}\left(\overline{V} - \frac{\beta}{2}\overline{V}^3\right) - \frac{\kappa_{\mathrm{v}}\kappa_{\mathrm{i}}}{2C\overline{V}}\overline{P}, \tag{3.40}$$

$$\frac{d}{dt}\overline{\theta} = \omega - \omega + \frac{\kappa_{\mathrm{v}}\kappa_{\mathrm{i}}}{2C\overline{V}^2}\overline{Q}, \tag{3.41}$$

where $\overline{P}$ and $\overline{Q}$ are the average real- and reactive-power outputs of the VO-controlled inverter (measured with respect to the nominal frequency, ω), respectively. See Appendix A for a

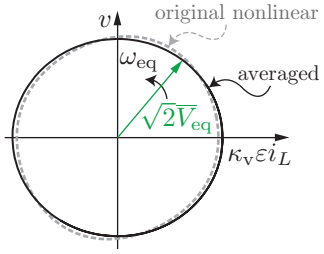

Figure 3.9: Superimposed steady-state limit cycles of the original nonlinear oscillator dynamics and the corresponding averaged model. The limit cycle of the averaged model can be described with a circle of fixed radius, $\sqrt{2}\overline{V}_{\rm eq}$, and constant rotational frequency, $\omega_{\rm eq}$, in quasistationary sinusoidal steady state; $\overline{V}_{\rm eq}$ and $\omega_{\rm eq}$ depend on the real and reactive power delivered by the oscillator, respectively (see (3.44) and (3.48)). (Source: [28])

brief derivation of (3.40)-(3.41), and [26] for more details. Figure 3.9 plots limit cycles recovered from: i) the original nonlinear dynamics, and ii) the averaged model for a Van der Pol oscillator.

Remarkably, with this nonlinear control strategy, it emerges that close to the sinusoidal steady state (recovered in the quasi-harmonic limit $\varepsilon \searrow 0$), the voltage-amplitude and phase dynamics are directly linked to the average real- and reactive-power outputs of the inverter, respectively. Consequently, these averaged dynamics can be leveraged for synthesizing virtual oscillators so that the inverter satisfies voltage- and frequency-regulation specifications in sinusoidal steady state. To this end, the equilibrium solutions are sought corresponding to (3.40)-(3.41) useful, since they establish the voltage- and frequency-regulation characteristics of the VO-controlled inverter.

Voltage-regulation Characteristic

The equilibria of (3.40) can be recovered from the solutions of the nonlinear equation:

$$0 = \frac{\sigma}{2C}\left(\overline{V}_{\rm eq} - \frac{\beta}{2}\overline{V}_{\rm eq}^3\right) - \frac{\kappa_{\rm v}\kappa_{\rm i}}{2C\overline{V}_{\rm eq}}\overline{P}_{\rm eq}, \tag{3.42}$$

where $\overline{V}_{\rm eq}$ and $\overline{P}_{\rm eq}$ represent the equilibrium steady-state RMS-voltage amplitude and average real-power output, respectively. Rearranging terms in (3.42), the following power-balance condition for the VO-controlled inverter is obtained:

$$\frac{\sigma\beta}{2}\overline{V}_{\rm eq}^4 - \sigma\overline{V}_{\rm eq}^2 + \kappa_{\rm v}\kappa_{\rm i}\overline{P}_{\rm eq} = 0. \tag{3.43}$$

The positive roots of (3.43) are given by

$$\overline{V}_{\rm eq} = \kappa_{\rm v} \left(\frac{\sigma \pm \sqrt{\sigma^2 - 6\alpha(\kappa_{\rm i}/\kappa_{\rm v})\overline{P}_{\rm eq}}}{3\alpha} \right)^{\frac{1}{2}}, \tag{3.44}$$

where $\sigma\beta = 3\alpha/\kappa_{\rm v}^2$ (see (3.34)). Notice that (3.44) has two roots. Both roots are real valued if the equilibrium real-power output satisfies

$$0 < \overline{P}_{\rm eq} < \overline{P}_{\rm cr} := \frac{\sigma^2}{6\alpha(\kappa_{\rm i}/\kappa_{\rm v})}, \tag{3.45}$$

where $\overline{P}_{\rm cr}$ is referred to as the *critical value* for real power. The corresponding critical value of the terminal voltage is given by

$$\overline{V}_{\rm cr} := \kappa_{\rm v}\sqrt{\frac{\sigma}{3\alpha}}. \tag{3.46}$$

Under a set of mild power-flow decoupling approximations, the high-voltage solution in (3.44) is locally asymptotically stable. Subsequently, the high-voltage solution of (3.44) is denoted by $\overline{V}_{\rm eq}$ with a slight abuse of notation. It is worth mentioning that the high-voltage root is a decreasing function of $\overline{P}_{\rm eq}$ over the range $0 \leq \overline{P}_{\rm eq} \leq \overline{P}_{\rm cr}$ (that is, steady-state voltage "droops" with increasing real power output). Finally, note that the open-circuit voltage of the VO-controlled inverter, $\overline{V}_{\rm oc}$, can be obtained by substituting $\overline{P}_{\rm eq} = 0$ into the high-voltage root in (3.44):

$$\overline{V}_{\rm oc} = \kappa_{\rm v}\sqrt{\frac{2\sigma}{3\alpha}}. \tag{3.47}$$

Frequency-regulation Characteristic

Consider the phasor-angle dynamics in (3.41). The equilibrium of (3.41) returns the frequency of the VO-controlled inverter:

$$\omega_{\rm eq} = \omega + \frac{\kappa_{\rm v}\kappa_{\rm i}}{2C\overline{V}_{\rm eq}^2}\overline{Q}_{\rm eq}, \tag{3.48}$$

where $\overline{V}_{\rm eq}$ is the stable high-voltage equilibrium obtained from (3.44), and $\overline{Q}_{\rm eq}$ is the average reactive-power output of the VO-controlled inverter.

3.3.3 Dynamic Response

The voltage dynamics of interest are recovered from (3.40) by setting $\overline{P} = 0$:

$$\frac{d}{dt}\overline{V} = \frac{\sigma}{2C}\left(\overline{V} - \beta\frac{1}{2}\overline{V}^3\right). \tag{3.49}$$

Since (3.49) is a variable-separable ordinary differential equation, we integrate both sides, setting the limits from $0.1\overline{V}_{\rm oc}$ to $0.9\overline{V}_{\rm oc}$ (without loss of generality). The time taken for this excursion is defined as the *rise time*; it is denoted by $t_{\rm rise}$, and given by the solution of:

$$t_{\rm rise} = \frac{2}{\varepsilon\sigma}\left[\log\overline{V} - \frac{1}{2}\log\left|1 - \frac{\beta}{2}\overline{V}^2\right|\right]_{0.1\overline{V}_{\rm oc}}^{0.9\overline{V}_{\rm oc}}.$$

Evaluating the limits above, recover, as in the convergence rate subsection previously,

$$t_{\rm rise} \approx \frac{6}{\omega\varepsilon\sigma}. \tag{3.50}$$

The approximation in (3.50) indicates that the rise time, $t_{\rm rise}$, is inversely proportional to ε. This aspect will be leveraged in the design of the oscillator capacitance, C, in Section 3.3.7. (Recall from (3.34) that $\varepsilon = \sqrt{L/C}$.)

For an inverter loaded to its rated real power rating with a resistive load, $R_{\rm rated}$, the rise time is given by $t_{\rm rise} \approx \frac{6}{\omega\varepsilon\sigma'}$, where $\sigma' = \left(\sigma - \frac{\kappa_{\rm v}\kappa_{\rm i}}{R_{\rm rated}}\right)$. The subsequent analysis on inverter design can be performed with this specification of rise time if need be.

3.3.4 Harmonics Analysis

Next, a closed-form analytical expression for the amplitude of the third harmonic of an unloaded VO-controlled inverter is derived. In particular, the effect of the nonlinear forcing term in (3.32) is investigated, as executed within the digital controller, on the low-order harmonic content of the ac output. The analysis is aimed at parameter selection with the aim of bounding the ratio of the amplitude of the third harmonic to the fundamental. To this end, the *perturbation methods* and the *method of multiple scales* [102] are invoked, that seek approximate analytical solutions to nonlinear dynamical systems where exact solutions cannot be found.

Consider the non-averaged dynamics of the terminal-voltage magnitude in an unloaded VO-controlled inverter:

$$\ddot{v} - \varepsilon\sigma\big(1 - \beta v^2\big)\dot{v} + v = 0, \tag{3.51}$$

where ε and β are defined in (3.34), and as before, the implicit assumption is of working in the quasi-harmonic limit, $\varepsilon \searrow 0$. This model follows from expressing (3.35) and (3.36) as a second-order system with the input current $i = 0$. We seek an approximate solution to (3.51) that can be expressed as:

$$v(\tau, \varepsilon) \approx v_0(\tau, \widetilde{\tau}) + \varepsilon v_1(\tau, \widetilde{\tau}). \tag{3.52}$$

The solution is written with respect to two time scales: the original time scale τ, and a slower time scale, $\widetilde{\tau} := \varepsilon\tau$. While higher-order time scales, i.e, $\varepsilon^2\tau$, $\varepsilon^3\tau$, can be analyzed in a similar fashion to obtain approximate solutions correct to higher-order terms, the analysis is: i) valid up to $\mathcal{O}(\varepsilon)$, ii) yields an approximate amplitude for the third harmonic, and iii) provides error terms of $\mathcal{O}(\varepsilon^2)$. Substituting (3.52) in (3.51), and retaining only $\mathcal{O}(\varepsilon)$ terms:

$$\left(\frac{\partial^2 v_0}{\partial \tau^2} + v_0\right) + \varepsilon\left(\frac{\partial^2 v_1}{\partial \tau^2} + v_1 + 2\frac{\partial^2 v_0}{\partial \tau \partial \widetilde{\tau}} - \sigma(1 - \beta v_0^2)\frac{\partial v_0}{\partial \tau}\right) = 0. \tag{3.53}$$

Note that (3.53) must hold for any small parameter ε; this can be ensured if:

$$\frac{\partial^2 v_0}{\partial \tau^2} + v_0 = 0, \tag{3.54}$$

$$\frac{\partial^2 v_1}{\partial \tau^2} + v_1 + 2\frac{\partial^2 v_0}{\partial \tau \partial \widetilde{\tau}} - \sigma(1 - \beta v_0^2)\frac{\partial v_0}{\partial \tau} = 0. \tag{3.55}$$

Since (3.54) represents the dynamics of a simple harmonic oscillator, the corresponding closed-form solution can be expressed as:

$$v_0(\tau, \widetilde{\tau}) = a_0(\widetilde{\tau}) \cos(\tau + \rho_0(\widetilde{\tau})), \tag{3.56}$$

where $a_0(\widetilde{\tau})$ and $\rho_0(\widetilde{\tau})$ are amplitude and phase terms that vary in the slow time scale specified by $\widetilde{\tau}$. For notational convenience, define the orthogonal signal $v_0^{\perp}(\tau, \widetilde{\tau})$ associated with $v_0(\tau, \widetilde{\tau})$ in (3.56) as follows:

$$v_0^{\perp}(\tau, \widetilde{\tau}) := a_0(\widetilde{\tau}) \sin(\tau + \rho_0(\widetilde{\tau})). \tag{3.57}$$

Substituting for v_0 from (3.56) into (3.55):

$$\begin{aligned}
&\frac{\partial^2 v_1}{\partial \tau^2} + v_1 = -2\frac{\partial^2 v_0}{\partial \tau \partial \widetilde{\tau}} + \sigma(1-\beta v_0^2)\frac{\partial v_0}{\partial \tau} \\
&= 2\frac{\partial v_0^{\perp}}{\partial \widetilde{\tau}} - \sigma v_0^{\perp} + \sigma\beta v_0^2 v_0^{\perp} \\
&= 2\frac{\partial a_0}{\partial \widetilde{\tau}}\sin(\tau+\rho_0) + 2v_0\frac{\partial \rho_0}{\partial \widetilde{\tau}} \\
&\quad - \sigma v_0^{\perp} + \sigma\beta a_0^3\left(\sin(\tau+\rho_0) - \sin^3(\tau+\rho_0)\right) \\
&= 2\frac{\partial a_0}{\partial \widetilde{\tau}}\sin(\tau+\rho_0) + 2v_0\frac{\partial \rho_0}{\partial \widetilde{\tau}} \\
&\quad - \sigma v_0^{\perp} + \frac{\sigma\beta}{4}a_0^3\left(\sin(3\tau+3\rho_0) + \sin(\tau+\rho_0)\right), \qquad (3.58)
\end{aligned}$$

where in the last line of (3.58) follows from using $\sin 3\theta = 3\sin\theta - 4\sin^3\theta$. Grouping together the coefficients that multiply the $\sin(\tau+\rho_0)$ and $\cos(\tau+\rho_0)$ terms, the last line of (3.58) can be rewritten as follows:

$$\begin{aligned}
\frac{\partial^2 v_1}{\partial \tau^2} + v_1 &= \left(2\frac{\partial a_0}{\partial \widetilde{\tau}} - \sigma a_0 + \frac{\sigma\beta}{4}a_0^3\right)\sin(\tau+\rho_0) \\
&\quad + \left(2a_0\frac{\partial \rho_0}{\partial \widetilde{\tau}}\right)\cos(\tau+\rho_0) \\
&\quad + \frac{\sigma\beta}{4}a_0^3\sin(3\tau+3\rho_0). \qquad (3.59)
\end{aligned}$$

The coefficients that multiply the $\sin(\tau+\rho_0)$ and $\cos(\tau+\rho_0)$ terms have to be forced to zero to ensure that unbounded terms of the form $\tau\sin(\tau+\rho_0)$ and $\tau\cos(\tau+\rho_0)$, do not appear in the solution for v_1, [5] and therefore:

$$2\frac{\partial a_0(\widetilde{\tau})}{\partial \widetilde{\tau}} - \sigma a_0(\widetilde{\tau}) + \frac{\sigma\beta}{4}a_0(\widetilde{\tau})^3 = 0, \qquad (3.60)$$

$$2a_0(\widetilde{\tau})\frac{\partial \rho_0(\widetilde{\tau})}{\partial \widetilde{\tau}} = 0. \qquad (3.61)$$

Solving (3.61) with initial condition $a_0(0)$, $a_0(\widetilde{\tau})$ can be expressed as:

$$a_0(\widetilde{\tau}) = \left(\frac{\beta}{4} + \mathrm{e}^{-\eta-\sigma\widetilde{\tau}}\right)^{-\frac{1}{2}}, \quad \mathrm{e}^{\eta} = \frac{a_0^2(0)}{1-\frac{\beta}{4}a_0^2(0)}. \qquad (3.62)$$

[5] Functions $\tau\sin(\tau+\rho_0)$ and $\tau\cos(\tau+\rho_0)$ grow without bound, and their existence would suggest that v is unbounded (see (3.52)). However, this contradicts the fact that the unforced Van der Pol oscillator has a stable limit cycle with finite radius.

It follows that the peak amplitude of the first harmonic in sinusoidal steady state is given by:

$$\lim_{\widetilde{\tau}\to\infty} a_0(\widetilde{\tau}) =: a_0 = \frac{2}{\sqrt{\beta}}. \tag{3.63}$$

Note that the RMS value corresponding to the peak amplitude in (3.63) matches the expression for the open-circuit voltage in (3.47). From (3.62), it can also be inferred that $a_0(\widetilde{\tau}) \neq 0$ if $a_0(0) \neq 0$. Therefore it can be seen from (3.60) that $\rho_0(\widetilde{\tau}) = \rho_0$, i.e., ρ_0 is independent of $\widetilde{\tau}$.

With these observations in place, finally recover the following equation that governs the evolution of $v_1(\tau, \widetilde{\tau})$ from (3.59)

$$\frac{\partial^2 v_1}{\partial \tau^2} + v_1 = \frac{2\sigma}{\sqrt{\beta}} \sin(3\tau + 3\rho_0). \tag{3.64}$$

The particular solution to (3.64) is given by the general form:

$$v_1(\tau) = -\frac{\sigma}{4\sqrt{\beta}} \sin(3\tau + 3\rho_0). \tag{3.65}$$

From (3.56), (3.63), (3.65), and (3.52), observe that the ratio of the amplitude of the third harmonic to the fundamental, a quantity denoted by $\delta_{3:1}$, is given by

$$\delta_{3:1} = \frac{\varepsilon\sigma}{8}. \tag{3.66}$$

If initial conditions for v_1 are taken into account while solving (3.64), (3.66) is correct up to $\mathcal{O}(\varepsilon)$. Moreover, the expression in (3.66) indicates that the undesirable third-order harmonic is directly proportional to ε.

With the background in place, a procedure is outlined to determine the Van der Pol oscillator parameters such that the VO-controlled inverter satisfies a set of ac performance specifications. The virtual-oscillator parameters to be determined are summarized in Table 3.1 below. The parameters are divided into: i) *scaling factors* κ_{v} and κ_{i} (addressed in Section 3.3.5); ii) *voltage-regulation parameters* σ and α (addressed in Section 3.3.6), and iii) *harmonic-oscillator parameters* L and C (addressed in Section 3.3.7). The performance specifications which the parameters are designed to satisfy include: the open-circuit voltage, $\overline{V}_{\mathrm{oc}}$; rated real-power output and corresponding voltage, $\overline{P}_{\mathrm{rated}}$ and $\overline{V}_{\mathrm{min}}$, respectively; rated reactive-power output, $|\overline{Q}_{\mathrm{rated}}|$; maximum-permissible frequency deviation, rise time, and ratio of the amplitude of the third harmonic to the fundamental, $|\Delta\omega|_{\mathrm{max}}$, $t_{\mathrm{rise}}^{\mathrm{max}}$, and $\delta_{3:1}^{\mathrm{max}}$, respectively.

Table 3.1: VOC Parameters (Source: [28])

Symbol	Description	Value	Units
κ_{v}	Voltage-scaling factor	126	V/V
κ_{i}	Current-scaling factor	0.15	A/A
σ	Conductance	6.09	Ω^{-1}
α	Coefficient of cubic current source	4.06	$\mathrm{A/V}^3$
C	Harmonic-oscillator capacitance	0.18	F
L	Harmonic-oscillator inductance	3.99×10^{-5}	H

Table 3.2: AC Performance Specifications. (Source: [28])

Symbol	Description	Value	Units
$\overline{V}_{\mathrm{oc}}$	Open-circuit voltage	126	V (RMS)
$\overline{P}_{\mathrm{rated}}$	Rated real power	750	W
$\overline{V}_{\mathrm{min}}$	Voltage at rated power	114	V (RMS)
$\lvert\overline{Q}_{\mathrm{rated}}\rvert$	Rated reactive power	750	VARs
ω	Nominal system frequency	$2\pi 60$	rad/sec
$\lvert\Delta\omega\rvert_{\mathrm{max}}$	Maximum frequency offset	$2\pi 0.5$	rad/sec
$t_{\mathrm{rise}}^{\mathrm{max}}$	Rise time (3.50)	0.2	sec
$\delta_{3:1}^{\mathrm{max}}$	Ratio of third-to-first harmonic (3.66)	2	%

Candidate design [*specifications*]. Accompanying the design strategy to pick system parameters, a running example is presented corresponding to the set of performance specifications in Table 3.2. The specifications result in voltage-regulation of $\pm 5\%$ around a nominal voltage of 120 V, and frequency-regulation of ± 0.5 Hz around a nominal frequency of 60 Hz. The design is subsequently implemented in the hardware prototype discussed in Section 3.4. □

3.3.5 Design of Scaling Factors, κ_{v} and κ_{i}

Notice from Fig. 3.8 that the parameters κ_{v} and κ_{i} respectively determine the voltage and current scaling between the physical-inverter terminal voltage and output current, and those

of the virtual-oscillator circuit. To standardize design, κ_{v} is chosen such that when the VO capacitor voltage is 1 V RMS, the inverter-terminal voltage is equal to the open-circuit voltage, $\overline{V}_{\mathrm{oc}}$. Furthermore, κ_{i} is selected such that when the VO output current is 1 A, the inverter is loaded to full rated capacity, $\overline{P}_{\mathrm{rated}}$. The values of κ_{v} and κ_{i} that ensure this are

$$\kappa_{\mathrm{v}} := \overline{V}_{\mathrm{oc}}, \quad \kappa_{\mathrm{i}} := \frac{\overline{V}_{\mathrm{min}}}{\overline{P}_{\mathrm{rated}}}. \tag{3.67}$$

A system of inverters with different power ratings connected in parallel share the load power in proportion to their ratings if the current gains are chosen as suggested by (3.67) [17, 26]. This directly follows as a consequence of (3.44) since $\kappa_{\mathrm{i}}\overline{P}_{\mathrm{eq}}$ is constant in the parallel configuration and therefore, $\overline{P}_{\mathrm{eq}}/\overline{P}_{\mathrm{rated}}$ is the same for each inverter with identical voltage drops across each output impedance.

Candidate design [*scaling factors*]. The specifications call for an open-circuit voltage, $\overline{V}_{\mathrm{oc}} = 126\,\mathrm{V}$. This translates to a voltage-scaling factor, $\kappa_{\mathrm{v}} = 126\,\mathrm{V/V}$. From the rated power and corresponding voltage, $\overline{P}_{\mathrm{rated}} = 750\,\mathrm{W}$ and $\overline{V}_{\mathrm{min}} = 114\,\mathrm{V}$, the current-scaling factor $\kappa_{\mathrm{i}} = 114/750 = 0.152\,\mathrm{A/A}$. □

3.3.6 Design of Voltage-regulation Parameters, σ and α

Here, the closed-form expression is used for the voltage-regulation characteristic in (3.44) to design the VO conductance, σ, and the cubic coefficient of the nonlinear voltage-dependent current source, α. Effectively, the design strategy suggested below ensures that the equilibrium RMS terminal voltage of the inverter, $\overline{V}_{\mathrm{eq}}$, is bounded between the limits: $\overline{V}_{\mathrm{oc}} \geq \overline{V}_{\mathrm{eq}} \geq \overline{V}_{\mathrm{min}}$, as the average real-power output, $\overline{P}_{\mathrm{eq}}$, is varied between the limits: $0 \leq \overline{P}_{\mathrm{eq}} \leq \overline{P}_{\mathrm{rated}}$.

First, notice from (3.47) that the choice of κ_{v} in (3.67) implies that α is related to σ through:

$$\alpha = \frac{2\sigma}{3}. \tag{3.68}$$

Next, substituting $\overline{P}_{\mathrm{eq}} = \overline{P}_{\mathrm{rated}}$ and $\overline{V}_{\mathrm{eq}} = \overline{V}_{\mathrm{min}}$ into the high-voltage solution of (3.44):

$$\overline{V}_{\mathrm{min}} = \kappa_{\mathrm{v}} \left(\frac{\sigma + \sqrt{\sigma^2 - 6\alpha(\kappa_{\mathrm{i}}/\kappa_{\mathrm{v}})\overline{P}_{\mathrm{rated}}}}{3\alpha} \right)^{\frac{1}{2}}. \tag{3.69}$$

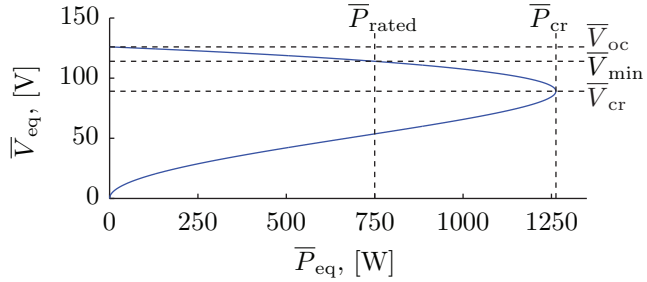

Figure 3.10: Equilibrium terminal voltage, $\overline{V}_{\text{eq}}$, as a function of the real-power output, $\overline{P}_{\text{eq}}$, for the oscillator parameters listed in Table 3.1. (Source: [28])

Substituting for κ_{v} and κ_{i} from (3.67), and for α from (3.68):

$$\overline{V}_{\text{min}} = \overline{V}_{\text{oc}} \left(\frac{\sigma + \sqrt{\sigma^2 - 4\sigma(\overline{V}_{\text{min}}/\overline{V}_{\text{oc}})}}{2\sigma} \right)^{\frac{1}{2}}. \tag{3.70}$$

Solving for σ above:

$$\sigma = \frac{\overline{V}_{\text{oc}}}{\overline{V}_{\text{min}}} \frac{\overline{V}_{\text{oc}}^2}{\overline{V}_{\text{oc}}^2 - \overline{V}_{\text{min}}^2}. \tag{3.71}$$

The choice of α and σ in (3.68) and (3.71), respectively, inherently establish the critical power value, $\overline{P}_{\text{cr}}$ in (3.45). The design has to be iterated if the margin of difference between the rated and critical power values is insufficient.

Candidate design [*voltage-regulation parameters*]. From the RMS open-circuit and rated-voltage values, $\overline{V}_{\text{oc}} = 126\,\text{V}$ and $\overline{V}_{\text{min}} = 114\,\text{V}$, applying (3.71), $\sigma = 6.09\,\Omega^{-1}$, and from (3.68), $\alpha = 4.06\,\text{A/V}^3$. The resulting voltage-regulation curve for these design specifications is illustrated in Fig. 3.10. The inverter is designed to operate in the voltage regime, $\overline{V}_{\text{oc}} \geq \overline{V}_{\text{eq}} \geq \overline{V}_{\text{min}}$. □

3.3.7 Design of Harmonic-oscillator Parameters, C and L

Here, expressions are leveraged for: i) the frequency-regulation characteristic (3.48), ii) the rise time (3.50), and iii) the ratio of amplitudes of the third harmonic to the fundamental (3.66) to obtain a set of design constraints for the harmonic-oscillator parameters, i.e., the capacitance, C, and inductance, L.

Begin with the equilibrium frequency analysis in Section 3.3.2 and the frequency-regulation characteristic in (3.48). The maximum permissible frequency deviation, denoted by $|\Delta\omega|_{\max}$, is a design input. Substituting for κ_{v} and κ_{i} from (3.67) in (3.48), and considering the worst-case operating condition for the terminal voltage,[6] the following lower bound on the capacitance is obtained, C:

$$C \geq \frac{1}{2|\Delta\omega|_{\max}} \frac{\overline{V}_{\mathrm{oc}}}{\overline{V}_{\min}} \frac{|\overline{Q}_{\mathrm{rated}}|}{\overline{P}_{\mathrm{rated}}} =: C^{\min}_{|\Delta\omega|_{\max}}, \tag{3.72}$$

where $\overline{Q}_{\mathrm{rated}}$ is the maximum average reactive power that can be sourced or consumed by the VO-controlled inverter.

Next, consider the analysis of the (open-circuit) voltage amplitude dynamics in Section 3.3.3, and the expression for the rise time in (3.50). With the maximum-permissible rise time, $t^{\max}_{\mathrm{rise}}$, serving as a design input, from (3.50) and (3.71), get the following upper bound for the capacitance, C:

$$C \leq \frac{t^{\max}_{\mathrm{rise}}}{6} \frac{\overline{V}_{\mathrm{oc}}}{\overline{V}_{\min}} \frac{\overline{V}^2_{\mathrm{oc}}}{\overline{V}^2_{\mathrm{oc}} - \overline{V}^2_{\min}} =: C^{\max}_{t_{\mathrm{rise}}}. \tag{3.73}$$

Finally, consider the harmonics analysis in Section 3.3.4, and the expression for the ratio of the amplitudes of the third harmonic to the fundamental in (3.66). With the maximum-permissible ratio, $\delta^{\max}_{3:1}$, serving as a design input, from (3.66) and (3.71) get an additional lower bound on the capacitance, C:

$$C \geq \left(\frac{1}{8\omega\delta^{\max}_{3:1}}\right) \frac{\overline{V}_{\mathrm{oc}}}{\overline{V}_{\min}} \frac{\overline{V}^2_{\mathrm{oc}}}{\overline{V}^2_{\mathrm{oc}} - \overline{V}^2_{\min}} =: C^{\min}_{\delta_{3:1}}. \tag{3.74}$$

Once a value of capacitance satisfying (3.72), (3.73), and (3.74) is selected, the inductance, L, follows from rearranging terms in (3.39):

$$L = \frac{1}{C(\omega)^2}. \tag{3.75}$$

Combining (3.72), (3.73), and (3.74), the range in which C must be selected to meet the

[6] This corresponds to consuming or sourcing the maximum reactive power at the minimum permissible terminal voltage, $\overline{V}_{\min}$, which is defined in (3.70).

performance specifications of frequency regulation, rise time, and harmonics is given by:

$$\max\left\{C^{\min}_{|\Delta\omega|_{\max}}, C^{\min}_{\delta_{3:1}}\right\} \leq C \leq C^{\max}_{t_{\text{rise}}}. \tag{3.76}$$

If $C^{\max}_{t_{\text{rise}}} < \max\left\{C^{\min}_{|\Delta\omega|_{\max}}, C^{\min}_{\delta_{3:1}}\right\}$, then it is not possible to simultaneously meet the specifications of frequency regulation, rise time, and harmonics. Therefore, (3.76) reveals a fundamental trade-off in specifying performance requirements and designing VO-controlled inverters. In particular, a VO-controlled inverter that offers a short rise time will necessarily have a larger frequency offset and harmonic distortion, while a tightly regulated VO-controlled inverter (smaller frequency offset and harmonic distortion) will necessarily have a longer rise time.

Candidate design [*harmonic-oscillator parameters*]. For the example of a VO-controlled inverter, the following ac performance specifications are selected $|\Delta\omega|_{\max} = 2\pi 0.5\,\text{rad/sec}$, $t^{\max}_{\text{rise}} = 0.2\,\text{sec}$, and $\delta^{\max}_{3:1} = 2\%$ (see Table 3.2). Substituting these into (3.72), (3.73), and (3.74), it is found that $C^{\min}_{|\Delta\omega|_{\max}} = 0.1759\,\text{F}$, $C^{\max}_{t_{\text{rise}}} = 0.2031\,\text{F}$, and $C^{\min}_{\delta_{3:1}} = 0.1010\,\text{F}$. Therefore, to meet the performance specifications, one must select the harmonic-oscillator capacitance, C, in the range $0.1759\,\text{F} \leq C \leq 0.2031\,\text{F}$. Without loss of generality, prioritizing the rise-time specification, C is selected at the lower bound of the specified range, i.e., $C = 0.1759\,\text{F}$. Since $\omega = 2\pi 60\,\text{rad/sec}$, it then follows from (3.75) that $L = 39.99\,\mu\text{H}$.

In closing, it is worth pointing out that the voltage- and frequency-regulation specifications for the inverter are given here in terms of worst-case limits. Given the ubiquity of droop control in this domain, they could be specified in terms of the active- and reactive-power droop coefficients, m_{P} and m_{Q}, respectively. Leveraging the correspondences in (3.79)-(3.80), the design procedure above (for the scaling, voltage-regulation, and harmonic-oscillator parameters) can be modified to ensure the VO-controlled inverter mimics a droop-controlled inverter with the specified m_{P} and m_{Q}, as shown next.

3.3.8 Comparison with Droop Control

For resistive distribution lines, droop control linearly trades off the inverter terminal-voltage amplitude versus active power; and inverter frequency versus reactive power. In the context

of the notation established above, these linear laws can be expressed as:

$$\overline{V}_{\rm eq} = \overline{V}_{\rm oc} + m_{\rm P}\overline{P}_{\rm eq}, \tag{3.77}$$

$$\omega_{\rm eq} = \omega + m_{\rm Q}\overline{Q}_{\rm eq}, \tag{3.78}$$

where $m_{\rm P} < 0$ is the active-power droop coefficient and $m_{\rm Q} > 0$ is the reactive-power droop coefficient [103]. In fact, it is shown in [104] that the relations in (3.77)–(3.78) provide robust performance for various types of line impedances and are thus referred to as *universal droop* laws. In the previous section, it was observed that the equilibria of the averaged VOC dynamics in (3.40)–(3.41) can be engineered to be in close correspondence with the droop laws in (3.77)–(3.78). For instance, a first-order expansion of $\overline{V}_{\rm eq}$ (as a function of $\overline{P}_{\rm eq}$) around the open-circuit voltage, $\overline{V}_{\rm oc}$, is of the form (3.77) with the following choice of $m_{\rm P}$:

$$m_{\rm P} = \frac{\kappa_{\rm v}\kappa_{\rm i}}{2\sigma}\left(\overline{V}_{\rm oc} - \beta\overline{V}_{\rm oc}^3\right)^{-1}. \tag{3.79}$$

This expression can be derived by evaluating $d\overline{V}_{\rm eq}/d\overline{P}_{\rm eq}$ from (3.43) at the open-circuit voltage, $\overline{V}_{\rm oc}$. Similarly, by inspecting (3.48), see that $\omega_{\rm eq}$ as a function of $\overline{Q}_{\rm eq}$ around the open-circuit voltage, $\overline{V}_{\rm oc}$, is of the form (3.78) with the following choice of $m_{\rm Q}$:

$$m_{\rm Q} = \frac{\kappa_{\rm v}\kappa_{\rm i}}{2C\overline{V}_{\rm oc}^2}. \tag{3.80}$$

With the design strategy proposed in Section 3.3 for the parameters $C, \kappa_{\rm v}, \kappa_{\rm i}, \alpha$, and σ, it emerges that the voltage-regulation characteristic in (3.44) and the frequency-regulation characteristic in (3.48) are close to linear over a wide load range. The experimental results in Section 3.4 (see Figs. 3.14 and 3.15) validate this claim; conclusively demonstrating that droop laws are embedded within the equilibria of the nonlinear VOC dynamics. This establishes the backward compatibility of VOC, in that it subsumes droop control in sinusoidal steady state.[7]

Also, consider the converse scenario where droop coefficients, $m_{\rm P}$ and $m_{\rm Q}$, are translated into VOC parameters. The choice of $\kappa_{\rm v}$, $\kappa_{\rm i}$ (as given by (3.67)), and α (as given by (3.68))

[7]In addition to the droop laws highlighted in (3.77)–(3.78), there are other droop laws for different network types. VOC can accommodate arbitrary network impedances by expressing the inverter terminal voltage as $v = x\sin\varphi + y\cos\varphi$, where $x = \kappa_{\rm v}\varepsilon i_L$, $y = \kappa_{\rm v} v_C$, and φ can be interpreted as an angular rotation in the polar plane [105]. With this setting, it can be shown that $\varphi = \pi/2$ yields the droop laws for inductive networks. For the remainder of this section, $\varphi = 0$ is assumed.

would remain unchanged. With regard to σ, from (3.79) and with β given in (3.34), get

$$\sigma = -m_{\mathrm{P}}^{-1}\frac{\kappa_{\mathrm{i}}}{2}. \tag{3.81}$$

Furthermore, from (3.80), it follows that the choice of capacitance, C is be given by

$$C = m_{\mathrm{Q}}^{-1}\frac{\kappa_{\mathrm{i}}}{2\overline{V}_{\mathrm{oc}}}, \tag{3.82}$$

while the inductance, L, would still be specified by (3.75). Limits on C can be considered in a similar fashion as before, if the specification on m_{Q} is in terms of an upper bound.

Although correspondences between the quasi-steady-state behavior of VOC and droop control exist as outlined above, their time-domain performance is markedly different. The main advantage of VOC is that it is a time-domain controller which acts directly on unprocessed ac measurements when controlling the inverter terminal voltage, as evident in (3.32). This is unlike droop control which processes ac measurements to compute phasor-based quantities, namely real and reactive power, which are then used to update the inverter voltage amplitude and frequency setpoints. Since phasor quantities are not well-defined in real-time, droop controllers must necessarily employ a combination of low-pass filters, cycle averaging, coordinate transformations, or $\pi/2$ delays to compute $\overline{P}_{\mathrm{eq}}$ and $\overline{Q}_{\mathrm{eq}}$ in (3.77)–(3.78) (see [76,106–108]). These filters, which typically have a cutoff frequency in the range of 1 Hz to 15 Hz [76, 106, 108], act as a bottleneck to control responsiveness which in turn cause a sluggish response. In contrast, VO-controlled inverters operate on real-time measurements and respond to disturbances as they occur. To illustrate these concepts, a simple case study is presented that demonstrates the time-domain performance of VOC and its power-sharing capabilities.

Simulation Case Study: Consider two identical single-phase inverters connected in parallel through resistors to a parallel R-L load and simulate the time-domain behavior of VOC. For comparison, the performance of droop control is also illustrated. For the droop controller implementation, the droop laws in resistive networks is used (3.77)-(3.78) and the control architecture is adopted from [107]. The virtual oscillator that emulates the regulation characteristics is then derived by using the aforementioned analysis (equations (3.81)-(3.82)).

Figure 3.11 depicts the time it takes for two inverters to synchronize starting from arbitrary initial conditions. The metric used is $||\Pi v||_2$, where $v = [v_1, v_2]^\top$ collects terminal voltages at the inverter. The matrix $\Pi := I_2 - \frac{1}{2}1_2 1_2^\top$ ($I_{2\times 2}$ is the 2×2 identity, and $1_{2\times 1}$ is the 2×1 vector with all entries equal to one) is the so-called projector matrix, and by

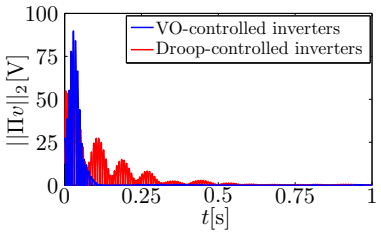

Figure 3.11: Synchronization error, captured from the deviation of the inverter terminal voltages from the average, as a function of time for VOC and droop control. The waveforms are obtained from switching-level simulations. (Source: [28])

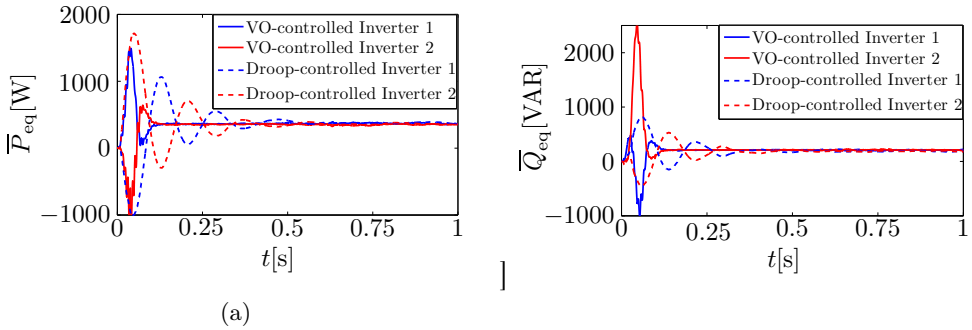

(a)

Figure 3.12: Active- and Reactive-power sharing for the 2-inverter case for VOC and droop control. (Source: [28])

construction, notice that Πv returns a vector where the entries capture deviations from the average of the vector v. From the figure, it can be seen that with VOC, the inverters synchronize by around $t = 0.1\,\text{s}$, while with droop control, the inverters synchronize by $t = 0.6\,\text{s}$. Furthermore, Figs. 3.12 (a)-(b) show that identical active-and reactive- power sharing is achieved with both control strategies; it is worth noting, however, VOC reaches steady-state faster than droop. The R-L load considered in this particular setup has values of $R_{\text{load}} = 20\,\Omega$ and $L_{\text{load}} = 0.1\,\text{H}$ with interconnecting conductances $g_{1,\text{line}} = 5\,\Omega^{-1}$ and $g_{2,\text{line}} = 4\,\Omega^{-1}$ respectively for Inverters 1 and 2. Readers are referred to [105] for other simulation parameters.

A similar simulation result has also been reported in [109]

Remark 2. The above simulation case study was verified experimentally in hardware, see [110].

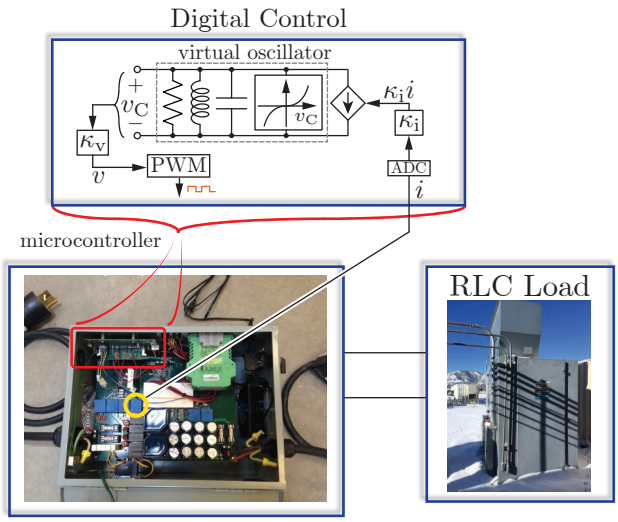

Figure 3.13: Picture of laboratory prototype of VO-controlled inverter and load. (Source: [28])

3.4 Experimental Validation

Engineers at NREL, Dr. Brian Johnson and Dr. Nathan Ainsworth, built a laboratory-scale hardware prototype of a VO-controlled inverter with design specifications in Table 3.2. A picture of the experimental setup is shown in Fig. 3.13. The scaling, voltage-regulation, and harmonic-oscillator parameters—that completely characterize the virtual oscillator and ensure the VO-controlled inverter satisfies the design specifications—were computed in the running example in Section 3.3, and they are listed in Table 3.1. The inverter LCL filter components have values $L_\mathrm{f} = 600\,\mu\mathrm{H}$, $C_\mathrm{f} = 24\,\mu\mathrm{F}$, and $L_\mathrm{g} = 44\,\mu\mathrm{H}$, where L_f, C_f, and L_g are the inverter-side inductor, ac-filter capacitor, and grid-side inductor, respectively (see Fig. 3.8). The switching frequency of the inverter is $T_\mathrm{sw}^{-1} = 15\,\mathrm{kHz}$, the dead time is 200 ns, and three-level unipolar sine-triangle PWM is utilized. The nonlinear dynamics of the virtual-oscillator circuit are programmed on a Texas Instruments TMS320F28335 microcontroller. A short note on the discretization is provided next.

3.4.1 Digital Controller Implementation

Denote the sampling time utilized in the numerical integration by T_s. In this particular implementation, $T_\mathrm{s}^{-1} = 15\,\mathrm{kHz}$. To discretize the virtual-oscillator dynamics (3.32), the

following difference equations are obtained using the trapezoidal rule:

$$\begin{aligned} v[k] = \left(1 - \frac{T_\mathrm{s}\sigma}{2C} + \frac{T_\mathrm{s}^2}{4LC}\right)^{-1} \Bigg[\left(1 + \frac{T_\mathrm{s}\sigma}{2C} - \frac{T_\mathrm{s}^2}{4LC}\right) v[k-1] \\ - \frac{T_\mathrm{s}}{C}\kappa_\mathrm{v} i_L[k-1] - \frac{T_\mathrm{s}}{2C}\kappa_\mathrm{v}\kappa_\mathrm{i}(i[k] + i[k-1]) \\ - \frac{\alpha T_\mathrm{s}}{2C\kappa_\mathrm{v}^2}(v^3[k] + v^3[k-1]) \Bigg], \\ i_L[k] = i_L[k-1] + \frac{T_\mathrm{s}}{2L\kappa_\mathrm{v}}(v[k] + v[k-1]), \end{aligned} \tag{3.83}$$

where $k \in \mathbb{Z}_{\geq 0}$ denotes the kth sampling instance, $i[k]$ is the sampled inverter-output current, $i_L[k]$ is the sampled Van der Pol oscillator inductor current, and $v[k]$ is the sampled inverter-terminal voltage. The difference equations (3.83) cannot be directly implemented on a digital controller, since they contain an algebraic loop through the cubic term $v^3[k]$. Therefore, it is necessary to make a simplifying assumption to eliminate the algebraic loop. While there are many approaches to accomplish this, one option is to simply make the assumption $v^3[k] \approx v^3[k-1]$, allowing (3.83) to be approximated as:

$$\begin{aligned} v[k] = \left(1 - \frac{T_\mathrm{s}\sigma}{2C} + \frac{T_\mathrm{s}^2}{4LC}\right)^{-1} \Bigg[\left(1 + \frac{T_\mathrm{s}\sigma}{2C} - \frac{T_\mathrm{s}^2}{4LC}\right) v[k-1] \\ - \frac{T_\mathrm{s}}{C}\kappa_\mathrm{v} i_L[k-1] - \frac{T_\mathrm{s}}{2C}\kappa_\mathrm{v}\kappa_\mathrm{i}(i[k] + i[k-1]) \\ - \frac{\alpha T_\mathrm{s}}{C\kappa_\mathrm{v}^2} v^3[k-1] \Bigg], \\ i_L[k] = i_L[k-1] + \frac{T_\mathrm{s}}{2L\kappa_\mathrm{v}}(v[k] + v[k-1]). \end{aligned} \tag{3.84}$$

The difference equations (3.84) yield realizable—albeit approximate—dynamics of the virtual oscillator circuit in Fig. 3.8, and they can be implemented directly on the digital controller. The inverter PWM modulation signal, m, can then be constructed as:

$$m[k] := \frac{v[k]}{v_\mathrm{dc}[k]}, \tag{3.85}$$

where $v_\mathrm{dc}[k]$ is the measured value of the inverter dc-bus voltage at the kth sampling instance.

The experimental results that are outlined next focus on validating: i) the steady-state voltage-regulation characteristic in (3.44), ii) the steady-state frequency-regulation characteristic in (3.48), iii) the expression for the rise time in (3.50), and iv) the expression for the

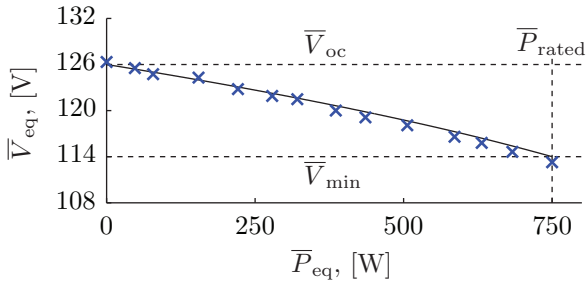

Figure 3.14: Measured versus analytically computed values for steady-state RMS voltage, $\overline{V}_{\text{eq}}$, versus output real power, $\overline{P}_{\text{eq}}$. (Source: [28])

ratio of the amplitudes of the third and first harmonics in (3.66). Results are summarized in Figs. 3.14-3.17; in each case, the analytical results are plotted as solid lines, while results from experimental studies are plotted as $\times$'s.

3.4.2 Steady-state Voltage Regulation

This experiment is performed with the VO-controlled inverter connected to a variable resistive load at the output terminals. The experimental results reported in Fig. 3.14 are obtained by varying the load resistance in discrete steps between open-circuit and $16.7\,\Omega$, and in each case, recording the steady-state RMS terminal voltage. The measured data (plotted as $\times$'s) match the analytical voltage-regulation characteristic (3.44) (plotted as a solid line). Note that the inverter RMS voltage stays within the prescribed upper and lower bounds, $\overline{V}_{\text{oc}}$ and $\overline{V}_{\text{min}}$, respectively, across the entire rated load-power range.

Comparison with voltage-amplitude droop control

The best-fit linear model (in a least-squares sense) to the experimentally collected values $\{\overline{V}_{\text{eq}}, \overline{P}_{\text{eq}}\}$ plotted in Fig. 3.14 is given by:

$$\overline{V}_{\text{eq}} = 126.5449 - 0.0171\,\overline{P}_{\text{eq}}. \tag{3.86}$$

The coefficient of determination—a metric that reveals the quality of a statistical model [111]—for this linear model is $99.59\,\%$. These findings conclusively demonstrate that the voltage-amplitude real-power droop law is embedded within the sinusoidal steady-state of VO-controlled inverters; validating the theoretical analysis in the previous sections.

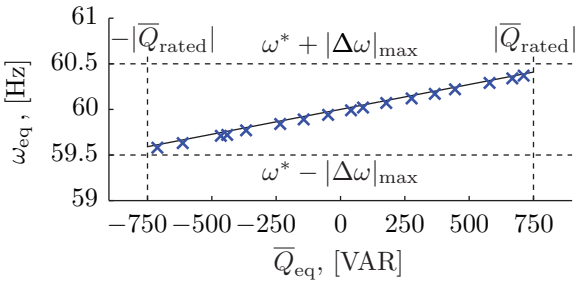

Figure 3.15: Measured versus analytically computed values for steady-state frequency, ω_{eq}, versus output reactive power, $\overline{Q}_{\text{eq}}$. (Source: [28])

3.4.3 Steady-state Frequency Regulation

The frequency-regulation characteristic in (3.48) is validated by connecting a variable reactive load to the inverter-output terminals and adjusting it in incremental steps such that the inverter is delivering purely reactive power into either a capacitive or inductive load. The load was varied such that the total reactive power delivered into the LCL filter and external load was between $\pm\overline{Q}_{\text{rated}}$ where $|\overline{Q}_{\text{rated}}| = 750\,\text{VAR}$. In particular, purely inductive loads were varied discretely between 46.9 mH and 442 mH and capacitive loads were adjusted between 14.9 μF and 92.7 μF. In Fig. 3.15, the measured steady-state reactive power delivered into the filter and load is plotted, $\overline{Q}_{\text{eq}}$, and the frequency at the inverter terminals. The solid curve corresponds to the analytically derived expression in (3.48) when evaluated at $\overline{V}_{\text{eq}} = \overline{V}_{\text{oc}}$ (since $\overline{P}_{\text{eq}} \approx 0$ for this particular experiment).

Comparison with frequency droop control

The best-fit linear model to the experimentally collected values $\{\omega_{\text{eq}}, \overline{Q}_{\text{eq}}\}$ plotted in Fig. 3.15 is given by:

$$\omega_{\text{eq}} = 376.8013 + 0.0035\,\overline{Q}_{\text{eq}}. \tag{3.87}$$

The coefficient of determination for this linear model is 99.98 %. Again, these observations demonstrate that the frequency-reactive power droop law is intrinsically embedded in the sinusoidal steady-state behavior of VO-controlled inverters, further validating the averaging analysis in the previous sections.

3.4.4 Harmonics

The expression for the ratio of the amplitude of the third harmonic to the fundamental, $\delta_{3:1}$, in (3.66) is validated next. In this experiment, the parameters L and C of the inverter VOC

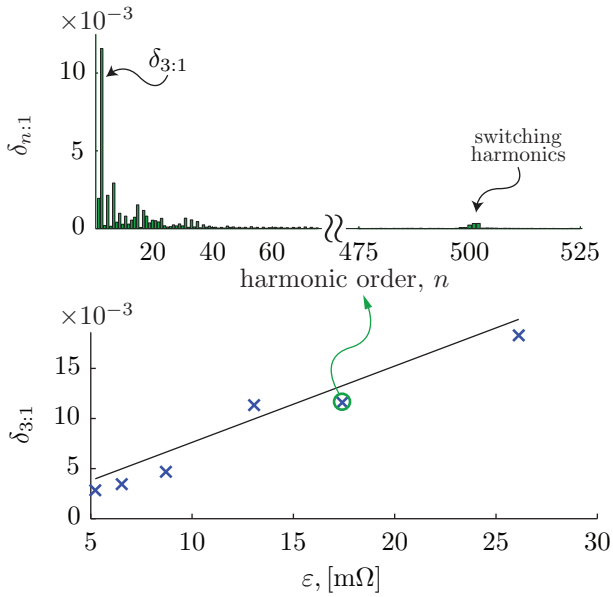

Figure 3.16: Measured versus analytically computed values of the ratio of the third harmonic amplitude and the fundamental amplitude, $\delta_{3:1}$, as a function of ε. Inset depicts higher-order harmonics for a particular value of ε. (Source: [28])

controller were adjusted so that $\varepsilon = \sqrt{L/C}$ varies while $\omega = 1/\sqrt{LC}$ remains constant at $2\pi 60\,\text{rad/sec}$. All other parameters are held fixed to the nominal values in Table 3.1. The $\times$'s in Fig. 3.16 represent experimentally collected values of $\delta_{3:1}$ as a function of ε, while the solid line follows from the expression in (3.66). The inset for a particular measurement confirms that the 3rd harmonic is dominant over all others.

3.4.5 Rise time

Finally, the expression for the rise time is validated, t_{rise}, in (3.50) (recall this is the time for the open-circuit inverter terminal-voltage magnitude to rise from 10% to 90% of its steady-state value $\overline{V}_{\text{eq}} = \overline{V}_{\text{oc}}$). The same sweep of the VOC parameters L and C as in Section 3.4.4 is used here, with all other parameters fixed to the nominal values in Table 3.1. The $\times$'s in Fig. 3.17 represent measured values of the rise time for each value of ε, while the solid line follows from the analytic expression (3.50).

Remark: The harmonics and rise-time experiments in Sections 3.4.4 and 3.4.5 report voltage measurements collected at the filter capacitor, C_{f}, i.e., the voltage v_{f} in Fig. 3.8. Since the $L_{\text{f}}C_{\text{f}}$ filter is solely designed to attenuate switching harmonics, in effect, the low-frequency and slow-time-scale behavior of the voltage, v_{f}, matches that of the inverter

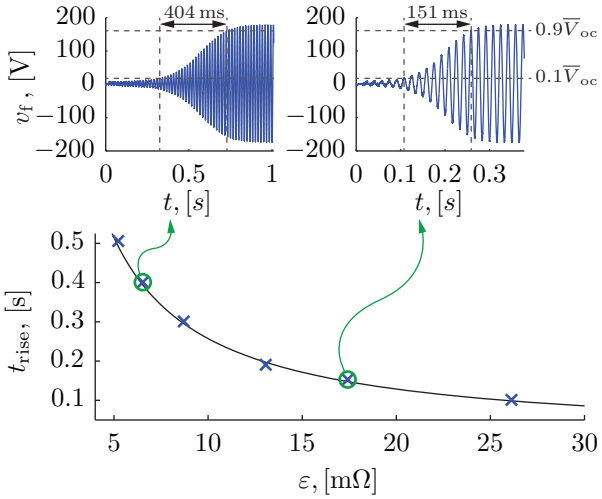

Figure 3.17: Measured versus analytically computed values of rise time, t_{rise}, as a function of ε. Insets depict time-domain waveforms of the inverter terminal voltage for two different values of ε. (Source: [28])

terminal voltage, v, for which the harmonics and rise-time analysis is performed in Section 3.3.4 and 3.3.3. In particular, since the corner frequency of the $L_{\text{f}}C_{\text{f}}$ low-pass filter, $1/\sqrt{L_{\text{f}}C_{\text{f}}} = 8.33 \times 10^3\,\text{rad/s} \gg \omega = 377\,\text{rad/s}$, and the open-circuit voltage builds up over multiple ac cycles, the rise-time of v_{f} closely mirrors that of the inverter terminal voltage, v. Furthermore, since $|v_{\text{f}}(\text{j}\omega)|/|\widetilde{v}(\text{j}\omega)| = \left\|(\text{j}\omega C_{\text{f}})^{-1}/((\text{j}\omega C_{\text{f}})^{-1} + \text{j}\omega L_{\text{f}})\right\|_2$ evaluated at ω and 3ω is approximately equal to 1.0021 and 1.0018, $\delta_{3:1}$ can be computed from measurements of v_{f} without compromising accuracy.

3.5 Stability of VOC Amplitude & Phase Dynamics

Having spent, most of the time on the *local* perspective, where the behavior on the inverter-level was scrutinized, the attention is now shifted towards the *network* level perspective. The questions of system stability and convergence are now asked, all of which depend, of course, on the kind of *network*. As demonstrated in chapter 2, the nature of trajectories that emerge is highly dependent upon the *nature of coupling*, which in this case is via the electrical network. In the following, resistive networks are considered; however, the results can be extended to heterogeneous lines with arbitrary resistances and inductances, provided the oscillator based controllers are tweaked according to the implementation at hand. A remark to that effect, deriving from the synchronization results presented in chapter 2, is included at the end. The notation is slightly abused, as in the following, r is used to denote

the amplitude as opposed to V in the previous section and the voltage κ_{v} scaling is dropped without loss of generality and can be introduced in a straightforward manner. Also, the current gains are just denoted by κ_j for the j-th inverter. With these slight modifications in place, the following averaged dynamics are considered for the analysis

$$\frac{d}{dt}\overline{r}_j = \frac{\alpha}{2C}\left(\overline{r}_j - \frac{\beta}{4}\overline{r}_j^3\right) - \frac{\kappa_j}{C\overline{r}_j}\overline{P}_j, \tag{3.88a}$$

$$\frac{d}{dt}\overline{\theta}_j = +\frac{\kappa_j}{C\overline{r}_j^2}\overline{Q}_j. \tag{3.88b}$$

3.5.1 Microgrid Network Architecture

The microgrid electrical network is described by an undirected graph with inverters and/or loads in the system connected to the nodes of the graph, and edges representing interconnections through transmission lines. The nodes of the electrical network are collected in the set $\mathcal{A}$, and branches (edges) are collected in the set $\mathcal{E} := \{(j,\ell)\} \subset \mathcal{A} \times \mathcal{A}$. Let $\mathcal{N} := \{1,\dots,N\} \subseteq \mathcal{A}$ denote nodes that the inverters are connected to, referred to as the set of *boundary nodes*. Shunt loads—modeled as parallel combinations of resistances and/or constant (in a synchronous dq-frame) current sources—are connected to *interior nodes*. The set $\mathcal{I} := \mathcal{A} \setminus \mathcal{N}$ collects all the interior nodes in the network.

Denote the vectors that collect the nodal current injections and node voltages in the network by $i_{\mathcal{A}}$ and $v_{\mathcal{A}}$, respectively. To be precise, $i_{\mathcal{A}}$ and $v_{\mathcal{A}}$ are real-valued functions of time. The coupling between the inverters is described by Kirchhoff's and Ohm's laws, which read in matrix-vector form as

$$i_{\mathcal{A}} = Q_{\mathcal{A}} v_{\mathcal{A}}, \tag{3.89}$$

where, entries of the *conductance matrix* $Q_{\mathcal{A}} \in \mathbb{R}^{|\mathcal{A}|\times|\mathcal{A}|}$ are

$$[Q_{\mathcal{A}}]_{j\ell} := \begin{cases} g_j + \sum_{(j,k)\in\mathcal{E}} g_{jk}, & \text{if } j = \ell, \\ -g_{j\ell}, & \text{if } (j,\ell) \in \mathcal{E}, \\ 0, & \text{otherwise}, \end{cases} \tag{3.90}$$

with $g_j \in \mathbb{R}_{\geq 0}$ denoting the shunt (load) conductance at node j, and $g_{j\ell} = g_{\ell j} \in \mathbb{R}_{\geq 0}$ the conductance of the line (j,ℓ).

Let $i = [i_1,\dots,i_N]^{\mathrm{T}}$ and $v = [v_1,\dots,v_N]^{\mathrm{T}}$ be the vectors of inverter current injections and terminal voltages at the boundary nodes, and let $i_{\mathcal{I}}$ and $v_{\mathcal{I}}$ be the vectors collecting

the current injections and nodal voltages for the interior nodes.[8] Entries of $i_{\mathcal{I}}$ are non-zero only if the interior nodes are connected to current sources. With this notation, (3.89) gives

$$\begin{bmatrix} i \\ i_{\mathcal{I}} \end{bmatrix} = \begin{bmatrix} Q_{\mathcal{N}\mathcal{N}} & Q_{\mathcal{N}\mathcal{I}} \\ Q_{\mathcal{N}\mathcal{I}}^{\mathrm{T}} & Q_{\mathcal{I}\mathcal{I}} \end{bmatrix} \begin{bmatrix} v \\ v_{\mathcal{I}} \end{bmatrix}. \tag{3.91}$$

Assuming that the submatrix $Q_{\mathcal{I}\mathcal{I}}$ is nonsingular,[9] the second set of equations in (3.91) can be uniquely solved for the interior voltages as $v_{\mathcal{I}} = Q_{\mathcal{I}\mathcal{I}}^{-1}(i_{\mathcal{I}} - Q_{\mathcal{N}\mathcal{I}}^{\mathrm{T}} v)$. Using this:

$$i = Qv + Q_{\mathcal{N}\mathcal{I}} Q_{\mathcal{I}\mathcal{I}}^{-1} i_{\mathcal{I}}, \tag{3.92}$$

where the matrix $Q = \left(Q_{\mathcal{N}\mathcal{N}} - Q_{\mathcal{N}\mathcal{I}} Q_{\mathcal{I}\mathcal{I}}^{-1} Q_{\mathcal{N}\mathcal{I}}^{\mathrm{T}}\right)$ is referred to as the *Kron-reduced conductance matrix*. This model reduction through a Schur complement of the conductance matrix is known as *Kron reduction* [55]. With a slight abuse of notation, the effective shunt-conductance load for the jth inverter is denoted by g_j (note that this is given by the jth nonnegative row sum of the Kron-reduced conductance matrix Q), and the effective conductance of the (j,ℓ) line in the Kron-reduced electrical network by $g_{j\ell} = -[Q]_{j\ell}$ in all subsequent discussions. Additionally, the shunt current source at the jth inverter recovered after Kron reduction, given by the jth entry of the vector $Q_{\mathcal{N}\mathcal{I}} Q_{\mathcal{I}\mathcal{I}}^{-1} i_{\mathcal{I}}$, will be denoted by $\iota_j \cos(\omega t + \gamma_j)$, where ι_j is the amplitude of the current source, and γ_j is the phase offset with respect to the rotating reference frame established by ω. With this notation, the average real- and reactive-power injections for the jth inverter are given by [82]:

$$\begin{aligned} \overline{P}_j &= \frac{\overline{r}_j \iota_j}{2} \cos(\overline{\theta}_j - \gamma_j) + \frac{\overline{r}_j^2}{2} g_{jj} - \frac{\overline{r}_j}{2} \sum_{\ell=1, \ell \neq j}^{N} g_{j\ell} \overline{r}_\ell \cos(\overline{\theta}_{j\ell}), \\ \overline{Q}_j &= \frac{\overline{r}_j \iota_j}{2} \sin(\overline{\theta}_j - \gamma_j) - \frac{\overline{r}_j}{2} \sum_{\ell=1}^{N} g_{j\ell} \overline{r}_\ell \sin(\overline{\theta}_{j\ell}), \end{aligned} \tag{3.93}$$

where $\overline{\theta}_{j\ell} := \overline{\theta}_j - \overline{\theta}_\ell$, and $\frac{\overline{r}_j \iota_j}{2} \cos(\overline{\theta}_j - \gamma_j)$ and $\frac{\overline{r}_j \iota_j}{2} \sin(\overline{\theta}_j - \gamma_j)$ are the active and reactive power drawn by the equivalent current source at the jth-inverter terminals (after Kron reduction). For these networks, the following well-posedness and convergence result is obtained.

Theorem 7 (Convergence of VOC). *Consider the interconnected averaged VOC dynam-*

[8] The subscript $\mathcal{N}$ is dropped when referring to the current and voltage vectors corresponding to the boundary nodes.

[9] This holds true in general for *RLC* networks, except for some pathological cases, see [54]. For the resistive networks, $Q_{\mathcal{I}\mathcal{I}}$ is always nonsingular due to irreducible diagonal dominance [55].

ics (3.88) *with real and reactive power injections given by* (3.93)*. Suppose that the terminal-voltage amplitudes are upper bounded by the open-circuit voltage,* $\overline{r}^{\mathrm{oc}} := \sqrt{4\alpha/3k}$.[10] *Assume further, that the network and oscillator parameters satisfy* $\forall j \in \mathcal{N}$

$$\frac{16}{81}\left(\alpha - \kappa_j g_{jj}\right)^3 \geq k\kappa_j^2 \left(\iota_j + \overline{r}^{\mathrm{oc}} \sum_{\ell=1,\ell\neq j}^{N} g_{j\ell}\right)^2 . \tag{3.94}$$

Then, for all initial conditions $(\overline{r}_0, \overline{\theta}_0) \in \mathbb{R}^N_{\geq 0} \times \mathbb{T}^N$ *that satisfy*

$$\overline{r}_j^{\mathrm{low}} := \sqrt{\frac{4}{9k}\left(\alpha - \kappa_j g_{jj}\right)} \leq \overline{r}_{0,j} \leq \overline{r}^{\mathrm{oc}}, \forall j \in \mathcal{N}, \tag{3.95}$$

the dynamics (3.88), (3.93) *have positive radii* $\overline{r}_j(t) \geq \overline{r}_j^{\mathrm{low}}$ *for all* $j \in \mathcal{N}$ *and for all* $t \geq 0$*, and they ultimately converge to a set of equilibria as* $t \to \infty$*.*

The assumptions in Theorem 7 are briefly discussed next. Condition (3.94) assures that the radii $\overline{r}_j(t)$ remain greater than a strictly positive value $\overline{r}_j^{\mathrm{low}}$ given in (3.95). Condition (3.94) is always guaranteed for sufficiently small current and resistive loads and a weakly coupled network, and it can be satisfied by choosing the ratio of design parameters α/κ_j sufficiently large. The proof of Theorem 7 relies on a gradient formulation of the system dynamics and LaSalle arguments:

Proof of Theorem 7. Inspired by [112] [113], the system (3.88), (3.93) is rewritten in gradient form as

$$\dot{\overline{r}}_j =: p_j(\overline{r}, \overline{\theta}) = -\nabla_{\overline{r}_j} H(\overline{r}, \overline{\theta}), \tag{3.96a}$$

$$\dot{\overline{\theta}}_j =: q_j(\overline{r}, \overline{\theta}) = -\frac{1}{\overline{r}_j^2} \nabla_{\overline{\theta}_j} H(\overline{r}, \overline{\theta}), \tag{3.96b}$$

where $[\overline{r},\ \overline{\theta}]^{\mathrm{T}} = [\overline{r}_1, \ldots, \overline{r}_N, \overline{\theta}_1, \ldots, \overline{\theta}_N]^{\mathrm{T}}$, and the potential $H : \mathbb{R}^N_{\geq 0} \times \mathbb{T}^N \to \mathbb{R}$ is defined as

$$H(\overline{r}, \overline{\theta}) := \sum_{j=1}^{N} \Bigg[\frac{\alpha}{4C}\left(-\overline{r}_j^2 + \frac{\beta}{8}\overline{r}_j^4\right) + \frac{\kappa_j \iota_j}{2C}\overline{r}_j \cos(\overline{\theta}_j - \gamma_j) + \frac{\kappa_j}{4C} g_{jj} \overline{r}_j^2 - \frac{\kappa_j}{2C} \sum_{\ell=1,\ell\neq j}^{N} \overline{r}_j \overline{r}_\ell g_{j\ell} \cos(\overline{\theta}_{j\ell}) \Bigg].$$

[10] The open-circuit voltage of the VO-controlled inverter is defined as the voltage obtained when no current is drawn from it. It is recovered from the high-voltage solution of (3.20) by setting $\overline{P}_{j,\mathrm{eq}} = 0$.

Notice that the phase dynamics (3.96b) are not defined for $\overline{r}_j = 0$, and the notion of a *radius* is ill-posed whenever $\overline{r}_j \leq 0$. Hence, establish conditions such that the radii remain greater than $\chi > 0$ are first established, i.e., conditions that ensure the set

$$\Omega_\chi := \left\{(\overline{r}, \overline{\theta}) \in \mathbb{R}^N_{\geq 0} \times \mathbb{T}^N : \chi \leq \overline{r}_j \leq \overline{r}^{\mathrm{oc}}, \forall j \in \mathcal{N}\right\}$$

is positively invariant are sought. To this end, cases are evaluated such that $p_j(\overline{r}, \overline{\theta}) \geq 0$ whenever $\left(\overline{r}, \overline{\theta}\right) \in \Xi_j \times \mathbb{T}^N$, where

$$\Xi_j := \left\{\overline{r} \in \mathbb{R}^N_{\geq 0} : \overline{r}_j = \chi_j, \chi_\ell \leq \overline{r}_\ell \leq \overline{r}^{\mathrm{oc}}, \ell \neq j\right\}, \tag{3.97}$$

with χ_j and χ_ℓ yet to be determined. In particular, $\forall j \in \mathcal{N}$

$$\begin{aligned}
&p_j(\overline{r}, \overline{\theta})|_{\left(\overline{r},\overline{\theta}\right)\in\Xi_j\times\mathbb{T}^N} \\
&= \left[\frac{\alpha}{2C}\left(\overline{r}_j - \frac{\beta}{4}\overline{r}_j^3\right) - \frac{\kappa_j \iota_j}{2C}\cos(\overline{\theta}_j - \gamma_j)\right. \\
&\quad \left. - \frac{\kappa_j \overline{r}_j}{2C} g_{jj} + \frac{\kappa_j}{2C}\sum_{\ell=1,\ell\neq j}^{N} g_{j\ell}\overline{r}_\ell \cos(\overline{\theta}_{j\ell})\right]\Big|_{\left(\overline{r},\overline{\theta}\right)\in\Xi_j\times\mathbb{T}^N} \\
&\geq \frac{\alpha}{2C}\left(\chi_j - \frac{\beta}{4}\chi_j^3\right) - \frac{\kappa_j}{2C}\left(\iota_j + \chi_j g_{jj} + \overline{r}^{\mathrm{oc}}\sum_{\ell=1,\ell\neq j}^{N} g_{j\ell}\right) \\
&\geq 0,
\end{aligned}$$

which holds if and only if there exists a $\chi_j \in \mathbb{R}_{>0}$ so that

$$h_j(\chi_j) := \frac{\alpha\beta}{4}\chi_j^3 - (\alpha - \kappa_j g_{jj})\,\chi_j + \kappa_j \iota_j + \kappa_j \overline{r}^{\mathrm{oc}} \sum_{\ell=1,\ell\neq j}^{N} g_{j\ell}$$

is nonpositive. Since h_j is a cubic polynomial with leading-order positive coefficient $\alpha\beta/4$, the question *whether there is a* $\chi_j > 0$ *so that* $h_j(\chi_j) < 0$ can be answered by calculating the positive maximum/minimum χ_j^* (the root of the equation $\partial h_j/\partial \chi_j = 0$) and verifying that $h_j(\chi_j^*) \leq 0$.[11] The positive root χ_j^* is denoted by $\overline{r}_j^{\mathrm{low}}$ in (3.95) and $h_j(\overline{r}_j^{\mathrm{low}}) \leq 0$ if and

[11] For $h(x) = ax^3 - bx + c$, the extremal points are obtained by $0 = \frac{\partial h}{\partial x} = 3ax^2 - b$. Assuming $a, b > 0$, the positive root is given by $x^* = \sqrt{\frac{b}{3a}}$. Thus, $h(x^*) = a\frac{b}{3a}\sqrt{\frac{b}{3a}} - b\sqrt{\frac{b}{3a}} + c$. Notice that $h(x^*) \leq 0$ if and only if $a\frac{b}{3a} - b \leq -c\sqrt{\frac{3a}{b}}$. This is equivalent to the condition $\frac{4}{27}b^3 \geq ac^2$.

only if (3.94) holds true. Hence, under condition (3.94), the set is positively invariant

$$\Omega := \left\{ (\overline{r}, \overline{\theta}) \in \mathbb{R}^N_{\geq 0} \times \mathbb{T}^N : \overline{r}^{\text{low}} \leq \overline{r}^{\text{low}}_j \leq \overline{r}_j \leq \overline{r}^{\text{oc}}, \forall j \in \mathcal{N} \right\},$$

where $\overline{r}^{\text{low}} := \min_{j \in \mathcal{N}} \overline{r}^{\text{low}}_j$. Every trajectory originating in Ω remains in Ω, i.e., $\overline{r}_j(t)$ is greater than $\overline{r}^{\text{low}}_j$, $\forall t \geq 0$.

The level sets of $H(\overline{r}, \overline{\theta})$ are closed (due to continuity), bounded in $\overline{\theta}$ (due to boundedness of the trigonometric nonlinearities), and radially unbounded in $\overline{r}$. Moreover, $H(\overline{r}, \overline{\theta})$ is non-increasing along trajectories, since

$$\begin{aligned} \dot{H}(\overline{r}, \overline{\theta}) &= -\sum_{j=1}^{N} \left(\nabla_{\overline{r}_j} H(\overline{r}, \overline{\theta})) \right)^2 + \left(\frac{1}{\overline{r}_j} \nabla_{\overline{\theta}_j} H(\overline{r}, \overline{\theta})) \right)^2 \\ &= -\sum_{j=1}^{N} p_j(\overline{r}, \overline{\theta})^2 + \overline{r}_j^2 q_j(\overline{r}, \overline{\theta})^2 \leq 0 \,. \end{aligned}$$

Thus, the sublevel sets of $H(\overline{r}, \overline{\theta})$ are compact and forward invariant, and by LaSalle's invariance principle [80, Theorem 4.4] that the dynamics (3.88), (3.93) converge to the largest positively invariant set contained in

$$\left\{ (\overline{r}, \overline{\theta}) \in \Omega : \, H(\overline{r}, \overline{\theta}) \leq H(\overline{r}_0, \overline{\theta}_0) \,, \, \dot{H}(\overline{r}, \overline{\theta}) = 0 \right\} ,$$

where the positive invariance of Ω is incorporated. The condition $\dot{H}(\overline{r}, \overline{\theta}) = 0$ identifies the set of equilibria and points of zero amplitude $\overline{r}_j = 0$. Since the latter set is excluded from Ω, all trajectories originating in Ω converge to the non-empty set of equilibria. □

Next, linearization of the system around an equilibrium point $(\overline{r}_{\text{eq}}, \overline{\theta}_{\text{eq}})$ is considered. The Jacobian of the system around the equilibrium point can be partitioned into blocks as follows:

$$J = \left[\begin{array}{c|c} J_{\text{A}} & J_{\text{B}} \\ \hline J_{\text{C}} & J_{\text{D}} \end{array} \right] . \tag{3.98}$$

The entries of $J_{\rm A}$, $J_{\rm B}$, $J_{\rm C}$, and $J_{\rm D}$ are specified as:

$$\Big[J_{\rm A}\Big]_{j\ell} = \begin{cases} \frac{\alpha}{2C}(1-\frac{3}{4}\overline{r}_{j,\rm eq}^2) - \frac{\kappa_j}{2C}g_{jj} & \text{if } j=\ell \\ \frac{\kappa_j}{2C}g_{jl}\cos(\overline{\theta}_{\rm eq,j\ell}) & \text{if } j\neq\ell \end{cases}$$

$$\Big[J_{\rm B}\Big]_{j\ell} = \begin{cases} 0 & \text{if } j=\ell \\ -\frac{\kappa_j}{2C}g_{j\ell}\overline{r}_{j,\rm eq}\sin(\overline{\theta}_{\rm eq,j\ell}) & \text{if } j\neq\ell \end{cases}$$

$$\Big[J_{\rm C}\Big]_{j\ell} = \begin{cases} 0 & \text{if } j=\ell \\ \frac{\kappa_j}{2C\overline{r}_{j,\rm eq}}g_{j\ell}\sin(\overline{\theta}_{\rm eq,j\ell}) & \text{if } j\neq\ell \end{cases}$$

$$\Big[J_{\rm D}\Big]_{j\ell} = \begin{cases} \frac{\kappa_j}{2C\overline{r}_{j,\rm eq}}\Big(\iota_j\cos(\overline{\theta}_{j,\rm eq}-\gamma_j) \\ -\sum_{\ell=1,\ell\neq j}^{N}\overline{r}_{\ell,\rm eq}\cos(\overline{\theta}_{j\ell,\rm eq})\Big) & \text{if } j=\ell \\ -\frac{\kappa_j}{2C\overline{r}_{j,\rm eq}}g_{j\ell}\overline{r}_{\ell,\rm eq}\cos(\overline{\theta}_{\rm eq,j\ell}) & \text{if } j\neq\ell, \end{cases}$$

where $\overline{\theta}_{\rm eq,jl} := \overline{\theta}_{j,\rm eq} - \overline{\theta}_{l,\rm eq}$. It is evident that when the angles differences between the nodes are small i.e., $\sin(\overline{\theta}_{j,\rm eq} - \overline{\theta}_{\ell,\rm eq}) \approx 0$, the system becomes *decoupled*, i.e., the Jacobian (4.32) becomes block-diagonal. In spirit, similar observations are frequently leveraged in analyzing bulk power-system dynamics in a variety of contexts [82]. Next, the amplitude and phase dynamics are studied under this decoupling assumption. In particular, the phase offsets (respectively, amplitudes) are assumed to be constant at their equilibrium values in the averaged amplitude (respectively, phase) dynamics in (3.88a) (respectively, (3.88b)). Following which, sufficient conditions are derived for the exponential stability of amplitude and phase dynamics.

3.5.2 Amplitude Dynamics in Decoupled Settings

Under the decoupling approximations described above, the phase offsets are fixed to their equilibrium values, i.e., $\overline{\theta}_j = \overline{\theta}_{j,\rm eq}, \forall j \in \mathcal{N}$; following which the terminal-voltage amplitude dynamics, recovered from (3.88a) and (3.93), are given by:

$$\begin{aligned}\dot{\overline{r}}_j = \frac{\alpha}{2C}\left(\overline{r}_j - \frac{\beta}{4}\overline{r}_j^3\right) - \frac{\iota_j\kappa_j}{2C}\cos(\overline{\theta}_{j,\rm eq}-\gamma_j) \\ - \frac{\kappa_j}{2C}g_{jj}\overline{r}_j + \frac{\kappa_j}{2C}\sum_{\ell=1,\ell\neq j}^{N} g_{j\ell}\overline{r}_\ell\cos(\overline{\theta}_{j\ell,\rm eq}).\end{aligned} \tag{3.99}$$

Theorem 8 (**Local exponential stability of decoupled amplitude dynamics).** *Consider the decoupled terminal-voltage amplitude dynamics in* (3.99)*. Suppose each inverter is*

loaded according to (3.45). *If an equilibrium,* $\overline{r}_{j,\mathrm{eq}}$, *satisfies*

$$\overline{r}_j^{\mathrm{low}} < \overline{r}_{j,\mathrm{eq}} \leq \overline{r}^{\mathrm{oc}},\ \forall j \in \mathcal{N}, \tag{3.100}$$

then it is locally exponentially stable.

Proof of Theorem 8. For small perturbations about the equilibrium point $\overline{r}_{\mathrm{eq}} = [\overline{r}_{1,\mathrm{eq}}, \ldots, \overline{r}_{N,\mathrm{eq}}]^{\mathrm{T}}$ of (3.42), express $\overline{r} = \overline{r}_{\mathrm{eq}} + \widetilde{r}$, where $\widetilde{r} := [\widetilde{r}_1, \ldots, \widetilde{r}_N]^{\mathrm{T}}$. Linearizing (3.99) around the equilibrium point (given by the solution of (3.42)), $\overline{r}_{\mathrm{eq}}$, $\dot{\widetilde{r}} = K\Gamma\widetilde{r}$, where $K := \mathrm{diag}\{\kappa_1, \ldots, \kappa_N\}$. The diagonal entries of Γ are

$$[\Gamma]_{jj} = \frac{\alpha}{2C\kappa_j}\left(1 - \frac{3}{4}\beta\overline{r}_{j,\mathrm{eq}}^2\right) - \frac{1}{2C}\left(g_j + \sum_{\ell=1,\ell\neq j}^{N} g_{j\ell}\right).$$

Furthermore, the matrix Γ is irreducible (due to connectivity) and symmetric since

$$[\Gamma]_{j\ell} = [\Gamma]_{\ell j} = \frac{1}{2C} g_{j\ell}\cos(\overline{\theta}_{j,\mathrm{eq}} - \overline{\theta}_{\ell,\mathrm{eq}}).$$

If

$$\frac{\alpha}{2\kappa_j}\left(1 - \frac{3}{4}\beta\overline{r}_{j,\mathrm{eq}}^2\right) - \frac{1}{2}g_j < 0, \tag{3.101}$$

then Γ is negative definite (due to strictly irreducible diagonal dominance [114]). By Sylvester's inertia theorem [115], the inertia (i.e., the triple of positive, negative, and zero eigenvalues) of Γ and $K\Gamma$ are identical since $\kappa_j > 0, \forall j \in \mathcal{N}$ and K is positive definite. Consequently, $K\Gamma$ is negative definite, provided (3.101) is satisfied. The bounds in (3.100) are obtained by rearranging terms in (3.101). The upper bound in (3.100) is the open-circuit voltage. □

3.5.3 Phase Dynamics in Decoupled Settings

Under the decoupling assumptions, the terminal-voltage amplitudes are fixed to their equilibrium values, $\overline{r}_j = \overline{r}_{j,\mathrm{eq}}, \forall j \in \mathcal{N}$, and the phase dynamics (3.88b) and (3.93) are given by:

$$\dot{\overline{\theta}}_j = \frac{\kappa_j}{2C\overline{r}_{j,\mathrm{eq}}}\left(\iota_j \sin(\overline{\theta}_j - \gamma_j) - \sum_{\ell=1,\ell\neq j}^{N} g_{j\ell}\overline{r}_{\ell,\mathrm{eq}}\sin(\overline{\theta}_{j\ell})\right). \tag{3.102}$$

Analysis of the decoupled phase dynamics (3.102) with coupled oscillator theory [44, 116] leads to the following result.

Theorem 9 (Local exponential stability of decoupled phase dynamics). *Consider the decoupled phase dynamics* (3.102)*. Assume that there exists an equilibrium* $\overline{\theta}_{j,\mathrm{eq}}$ *so that*

$$|\overline{\theta}_{j\ell,\mathrm{eq}}| < \pi/2 \quad \textit{and} \quad |\overline{\theta}_{j,\mathrm{eq}} - \gamma_j| > \pi/2, \quad \forall j, \ell \in \mathcal{N}. \tag{3.103}$$

If there is at least one constant current load, then the equilibrium $\overline{\theta}_{j,\mathrm{eq}}$ *is locally exponentially stable. Without constant current loads, the phase-synchronized equilibrium manifold* $\overline{\theta}_{j,\mathrm{eq}} = \overline{\theta}_{\ell,\mathrm{eq}}$*, for all* $j, \ell \in \mathcal{N}$*, is locally exponentially stable.*

Condition (3.103) identifies the equilibria corresponding to small reactive power flows (as suggested by the condition $|\overline{\theta}_{j\ell,\mathrm{eq}}| < \pi/2$) and requires the local current sources to inject reactive power (as suggested by the condition $|\overline{\theta}_{j,\mathrm{eq}} - \gamma_j| > \pi/2$). Without current loads, the phase synchronization result perfectly matches the previous experimental results in [17, 20].

Proof of Theorem 9. Linearization of (3.102) around the equilibrium point $\overline{\theta}_{\mathrm{eq}}$ yields $\dot{\widetilde{\theta}} = K\Theta M\widetilde{\theta}$, where $\overline{\theta} = \overline{\theta}_{\mathrm{eq}} + \widetilde{\theta}$, $K := \mathrm{diag}\{\kappa_1/\overline{r}_{1,\mathrm{eq}}, \ldots, \kappa_N/\overline{r}_{N,\mathrm{eq}}\}$ and $M := \mathrm{diag}\{\overline{r}_{1,\mathrm{eq}}, \ldots, \overline{r}_{N,\mathrm{eq}}\}$. The matrix Θ is irreducible (due to connectivity), and symmetric with off-diagonal entries

$$[\Theta]_{j\ell} = [\Theta]_{\ell j} = \frac{g_{j\ell}}{2C}\cos(\overline{\theta}_{j\ell,\mathrm{eq}}).$$

The diagonal entries of Θ are given by

$$[\Theta]_{jj} := \frac{\iota_j}{2C\overline{r}_{j,\mathrm{eq}}}\cos(\overline{\theta}_{j,\mathrm{eq}} - \gamma_j) - \sum_{\ell=1,\ell\neq j}^{N} [\Theta]_{j\ell}.$$

Under assumption (3.103), the off-diagonal entries $[\Theta]_{j\ell}$ are nonnegative, and all row sums are non-positive. If there is at least one constant current load, the associated row sum is strictly negative. Hence, Θ is irreducibly diagonal dominant (due to connectivity), and thus also nonsingular [114, Corollary 6.2.27]. It follows that Θ is negative definite, and the equilibrium $\overline{\theta}_{\mathrm{eq}}$ is isolated and locally exponentially stable. In the absence of local current loads, the negative Jacobian, $-\Theta$, is a Laplacian matrix associated with an undirected and connected graph. For this matrix, the phase-synchronized equilibrium manifold is locally exponentially stable; see [44, Theorem 5.1] for details. The eigenvalues of the matrix $(K\Theta)M$ are the same as $M(K\Theta)$. Since K, M are diagonal and Θ is symmetric, again by Sylvester's inertia theorem [115], the inertia of Θ and $MK\Theta$ are identical since $\kappa_j > 0, \overline{r}_j > 0, \forall j \in \mathcal{N}$. Consequently, $K\Theta M$ is negative definite, and therefore, the phase dynamics are locally exponentially stable, provided that (3.103) is satisfied. □

Remark 3. The stability results presented here can be extended in various ways. If the networks are series R-L, which is a common model for transmission line interconnections, then if instead of the virtual capacitor voltage v, a filtered version of the voltage, $(s+\gamma)v$ is used, which amounts to the linear combination of the states of the oscillator, then one can guarantee the asymptotic convergence of oscillator dynamics too. The proofs follow a mixture of the state-space methods mentioned in Chapter 2 and the averaging technique followed in this chapter to establish the stability certificates.

Chapter 4

Decentralized Switch Interleaving for DC-DC Converters

This chapter presents a decentralized switch-interleaving control strategy for multiphase dc-dc buck converters serving a common load. The architecture presents no single point of failure and requires no communication between the converters. The proposed controller is grounded on the dynamics of a type of nonlinear oscillator, engineered such that the interleaved state is characterized by the minimum stored energy in a collection of such nonlinear oscillators. Convergence to the interleaved state is spontaneously driven by the intrinsic interconnection of the underlying nonlinear dynamical systems through the electrical network and without the need for an explicit communication bus. (See Fig. 4.1(a).) In addition to establishing analytical guarantees for convergence and stability, experimental results are provided for a parallel connected buck converter setup to validate the concept.

Interleaved multiphase architectures are increasingly emerging as the norm in a variety of applications including (but not limited to): dc front-end converters in renewable energy systems and microgrids [3, 117, 118], voltage regulator modules [119–121], and power-factor correction circuits [122, 123]. Many compelling reasons underscore the widespread adoption of interleaved multiphase converters including: cost (canceling ripple reduces the requirements for passive filters), reliability (bulk capacitors used in filters are recognized reliability bottlenecks), modularity (the system can operate in a lower power mode with a reduced number of converters), power ratings (current-handling capacity of parallel systems is higher than an individual converter), and efficiency (converters can be turned on/off to minimize losses depending on the load to be served; this is commonly referred to as *phase shedding*). Decentralized interleaving realizes all the the benefits of multiphase dc-dc converter systems

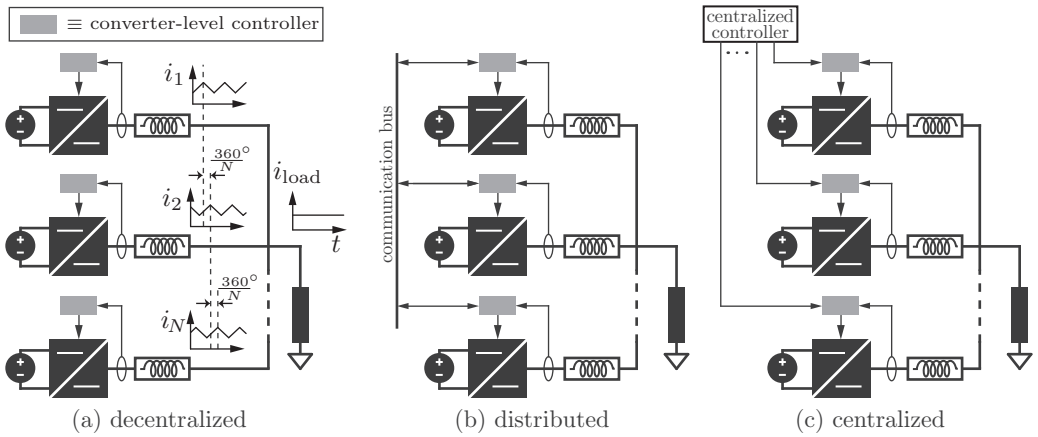

Figure 4.1: Proposed approach to interleaving is (a) decentralized, representing a paradigm shift since it is communication free with no single point of failure. State-of-the-art methods for interleaving are (b) distributed, requiring a communication bus [1, 2]. Majority of the literature on interleaving focuses on switch timing managed (c) centrally [3–8]. (Current waveforms not shown in (b) and (c) for conciseness.) (Source: [30])

mentioned previously, with the bonus that interleaving can be guaranteed with no single point of failure and independent of load fluctuations and initial conditions. Furthermore, the decentralized nature of the proposed controller enables a decoupling of the real-time interleaving operation from supervisory-level routines such as droop control or phase shedding which can then be realized with low-bandwidth signals during normal operation.

State-of-the-art approaches to switch interleaving are currently (at best) distributed, requiring an explicit communication bus as shown in Fig. 4.1(b) [1, 2]. In fact, a majority of the literature in this domain has focused largely on centralized approaches (see Fig. 4.1(c)) which have reliability, implementation, and modularity bottlenecks [3–8]. The method proposed in this work (see Fig. 4.1(a)) allows interleaving without any explicit communication channel, and thereby enables modular, reliable, and low-cost multiphase architectures.

Nonlinear oscillator dynamics form the basis of the proposed control strategy. In particular, the discretized second-order dynamics of a particular type of nonlinear oscillator—called the Liénard oscillator— is programmed on the digital controller of each converter. The locally measured inductor current for each converter acts as an input to the oscillator, and the oscillator dynamical states are used to generate the corresponding triangular PWM carrier (see Fig. 4.2 for details). Liénard oscillator dynamics have been examined in a variety of scientific and engineering disciplines [124]. Tangentially related to the application at hand, they have been used to realize decentralized real-time synchronization of ac voltages for

inverters in microgrids [17–19, 125, 126], adaptive synchronization of grid-connected three-phase inverters [127], and carrier wave synchronization for three-phase parallel-connected inverters to suppress circulating currents [128]. While these studies examined *synchronization* of waveforms in the context of *ac* systems, here, the focus is on the dual problem of *interleaving* PWM waveforms for *dc* systems. Theoretical foundations for this work are grounded on passivity-based frameworks to examine the networked dynamics of nonlinear oscillators. This is an expansive research topic, see, e.g., [23, 25, 129–131].

The theoretical and experimental results in this section are presented with buck converters serving as the topology of choice in the parallel-connected multiphase system. However, it must be noted that the analytical approach and feedback-synthesis method developed here can conceivably be applied to other converter topologies and network architectures. Focusing on the application at hand, while the proposed nonlinear controllers generate the interleaved PWM carriers, we leverage outer-loop droop controllers to ensure decentralized proportional power sharing [3]. From a theoretical vantage point, the main contribution of this work is to establish analytical guarantees for the existence and stability of the interleaved solutions. To that end, a model is built for the parallel-connected converter system based on the collective dynamics of the oscillators, buck converters, and the electrical network. Then, we leverage a coordinate transformation of the system dynamics to polar coordinates to extract amplitude and phase information of the PWM waveforms. Following this, the stability of equilibria that result from the involved dynamics is discussed. Experimental results demonstrate spontaneous convergence to the interleaved state through a variety of large-signal disturbances including: startup from arbitrary initial conditions, load steps, and converter addition. While the analysis considers an ideal, symmetric, and uniform setting with equal dc-bus voltages and equal values for filter elements, the exhaustive experimental validation establishes robustness of the control strategy to parasitics, and parametric and input variations that are inescapable in any hardware implementation.

4.1 System Description and Modeling

In this section, the model of the oscillator-controlled dc-dc buck converters is described that are connected in parallel and are supplying a common load. Using circuit laws and dynamics of the oscillators, we derive a coupled-oscillator model and then transform it to polar coordinates to extract phase information of the PWM waveforms.

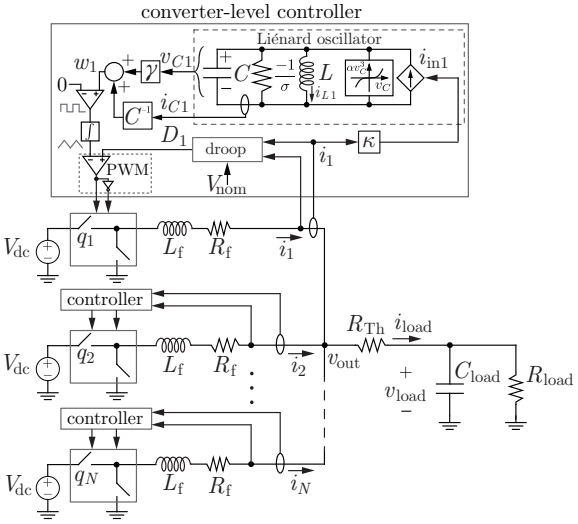

Figure 4.2: System of parallel-connected buck converters with local controllers. The proposed controller has the dynamics of a nonlinear Liénard-type oscillator circuit which takes the converter output current as feedback and generates the triangular PWM carrier at each converter by using a linear combination of its states. Droop control ensures decentralized power sharing. (Source: [30])

4.1.1 Controller Description

The system architecture is illustrated in Fig. 4.2. It is composed of N parallel dc-dc buck converters indexed in the set $\mathcal{N}$ supplying a common load. The controller for each converter (labeled *converter-level controller* for the first converter and simply as *controller* for the others) is decentralized and composed of two parts: i) a discretized version of the second-order differential equation which describes Liénard-type oscillators (labeled as *Liénard oscillator* for the first converter) that is responsible for switch interleaving, and ii) a slower-timescale droop-control-based voltage-regulation method (labeled as *droop* for the first converter).

The virtual-oscillator inductor and capacitor, L and C, are selected such that the oscillator resonant frequency coincides with the switching frequency $\omega_{\text{sw}} = 1/\sqrt{LC}$ (the switching period is denoted by $T_{\text{sw}} = 2\pi/\omega_{\text{sw}}$). Furthermore, ensuring that $\sqrt{L/C} \ll 1$ renders the j-th oscillator voltage, $v_{Cj}(t)$, to be nearly sinusoidal [17]. The oscillator further consists of a negative conductance, $-\sigma$, and a voltage dependent current source, αv_{Cj}^3, where $\alpha \in \mathbb{R}$ is a positive real constant. Next, the j-th comparator and integrator act on a scaled sum of $v_{Cj}(t)$ and $i_{Cj}(t)$ to yield the PWM carrier (the comparator creates a square wave and the integrator produces the carrier). Lastly, the switch pulses are generated in a typical fashion where the carrier and duty ratio, D_j, are fed to a comparator and associated logic. This proposed structure for carrier generation is independent of the controller that governs the

duty ratio. The outer-loop controller that generates the duty ratio runs on a much slower time scale. Here, a prototypical droop controller is considered that yields the duty ratio for each converter (details are in Section 4.1.3). Each converter has an inductive output filter $L_{\rm f}$ (with parasitic resistance, $R_{\rm f}$), and dc input voltage, $V_{\rm dc}$. The load is modeled as a parallel combination of a resistor, $R_{\rm load}$, and a capacitor, $C_{\rm load}$, behind a Thévenin resistance, $R_{\rm Th}$.

4.1.2 Parallel-converter System Model in Polar Coordinates

To analyze interleaving, it is necessary to describe the evolution of the phases corresponding to the switching signals of the converters controlled as shown in Fig. 4.2. Kirchhoff's laws yield the following dynamics for the inductor current, i_{Lj}, and capacitor voltage, v_{Cj}, for the j-th oscillator in each controller:

$$L\frac{di_{Lj}}{dt} = v_{Cj}, \quad C\frac{dv_{Cj}}{dt} = (\sigma v_{Cj} - \alpha v_{Cj}^3) - i_{Lj} + i_{{\rm in}j}. \tag{4.1}$$

Above, $i_{{\rm in}j}$ denotes the input current that serves as feedback to the oscillator. (See Fig. 4.2.) Defining $\varepsilon := \sqrt{L/C}$, $x_j := \varepsilon i_{Lj}$, and $y_j := v_{Cj}$, the above dynamics can be rewritten as

$$\dot{x}_j = \omega_{\rm sw} y_j, \quad \dot{y}_j = -\omega_{\rm sw} x_j + \varepsilon\left(\sigma y_j - \alpha y_j^3\right) + \varepsilon i_{{\rm in}j}. \tag{4.2}$$

Notice that x_j and y_j are orthogonal. To extract the phase dynamics, the amplitude is defined and instantaneous phase angle corresponding to (4.2) as below:

$$r_j = \sqrt{x_j^2 + y_j^2}, \quad \phi_j = \arctan\left(\frac{x_j}{y_j}\right). \tag{4.3}$$

To simplify analysis, the focus is on the phase-angle offset $\theta_j = \phi_j - \omega_{\rm sw} t$, which quantifies the angle difference with respect to a nominal reference frame rotating at the switching frequency, $\omega_{\rm sw}$. Algebraic and trigonometric manipulations applied to (4.2) yield the following amplitude and phase-offset dynamics:

$$\begin{aligned}
\dot{r}_j &= \varepsilon\omega_{\rm sw}\sigma r_j \cos^2(\omega_{\rm sw} t + \theta_j) - \varepsilon\omega_{\rm sw}\alpha r_j^3 \cos^4(\omega_{\rm sw} t + \theta_j) \\
&\quad + \varepsilon\omega_{\rm sw} i_{{\rm in}j} \cos(\omega_{\rm sw} t + \theta_j), \\
\dot{\theta}_j &= -\frac{\varepsilon\omega_{\rm sw}}{2}\left(\sigma - \alpha r_j^2 \cos^2(\omega_{\rm sw} t + \theta_j)\right)\sin(2\omega_{\rm sw} t + 2\theta_j) \\
&\quad - \frac{\varepsilon\omega_{\rm sw}}{r_j} i_{{\rm in}j} \sin(\omega_{\rm sw} t + \theta_j).
\end{aligned} \tag{4.4}$$

Given that (4.4) is time varying, it is difficult to analyze. Averageing it over one switch cycle yields the following averaged model:[1]

$$\dot{\overline{r}}_j = \frac{\varepsilon\omega_{\rm sw}}{2}\left(\sigma\overline{r}_j - 3\alpha\overline{r}_j^3\right) + \frac{\varepsilon\omega_{\rm sw}^2}{2\pi}\int_0^{T_{\rm sw}} i_{{\rm in}j}\cos(\omega_{\rm sw}t + \overline{\theta}_j)dt,$$

$$\dot{\overline{\theta}}_j = -\frac{\varepsilon\omega_{\rm sw}^2}{2\pi\overline{r}_j}\int_0^{T_{\rm sw}} i_{{\rm in}j}\sin(\omega_{\rm sw}t + \overline{\theta}_j)dt, \tag{4.5}$$

where $\overline{r}_j$, $\overline{\theta}_j$ are the averaged states. The derivation of (4.5) uses integration by parts and ignores second order (i.e., $\mathcal{O}(\varepsilon^2)$) terms (see [132] for details on a similar proof for a different application). Furthermore, it can be shown that in the parametric regime $\varepsilon \ll 1$ where waveforms are sinusoidal, the original oscillator dynamics can be approximated by the averaged model with $\mathcal{O}(\varepsilon)$ error [59, 87, 126, 132].

4.1.3 Feedback and Coupled-oscillator Dynamical Model

The feedback for the oscillators is through the current $i_{{\rm in}j}$, which, as shown in Fig. 4.2, is constructed as follows:

$$i_{{\rm in}j} = \kappa i_j, \tag{4.6}$$

where $\kappa > 0$ is a feedback gain and i_j is the output current of the buck converter. Furthermore, the signal used to generate the PWM carrier wave, w_j, is built as the following linear combination of the virtual-oscillator dynamic states:

$$w_j = \frac{1}{C}i_{Cj} + \gamma v_{Cj}, \tag{4.7}$$

where

$$\gamma := \frac{R_{\rm f}}{L_{\rm f}}. \tag{4.8}$$

It turns out that the above strategy is equivalent to constructing the feedback as:

$$i_{{\rm in}j} = \kappa\left(\gamma i_j + \frac{di_j}{dt}\right), \tag{4.9}$$

[1]For a time-varying dynamical system $\dot{x} = \varepsilon f(x,t,\varepsilon)$ where vector field $f(x,t,\varepsilon)$ is time periodic with period $T > 0$ (i.e., $f(x,t,\varepsilon) = f(x,t+T,\varepsilon)$), and $0 < \varepsilon \ll 1$, the associated *time-averaged dynamical system* is given by $\dot{\overline{x}} = \varepsilon\overline{f}(\overline{x}) = \varepsilon\frac{1}{T}\int_{\tau=0}^{T} f(\overline{x},\tau,0)d\tau$. The solution of the averaged system is $\mathcal{O}(\varepsilon)$ *close* to the solution of the original system, i.e., $||x(t,\varepsilon) - \overline{x}(\varepsilon t)||_2 = \mathcal{O}(\varepsilon), \quad \forall t \in [0, t^*]$, for some $t^* > 0$ for which unique solutions exist for both systems and assuming $||x(0,\varepsilon) - \overline{x}(0)||_2 = \mathcal{O}(\varepsilon)$ [59].

with the PWM carrier wave picked to be the virtual-capacitor voltage and the coefficient of nonlinearity for the voltage-dependent current source in the oscillator accordingly rescaled as follows:

$$w_j = v_{Cj}, \quad \alpha' = \frac{\alpha}{\sqrt{\omega_{\text{sw}}^2 + \gamma^2}}\,. \tag{4.10}$$

For subsequent developments this equivalent system is leveraged for analytical convenience since the feedback in (4.9) brings forth the coupling between the oscillators (see (B.9)). However, while the feedback and PWM carrier wave generation through (4.9)–(4.10) facilitate analysis, they involve an acausal derivative term that challenges implementation. Therefore, the hardware implementation is built with the priorly introduced feedback and PWM carrier wave generation method in (4.6)–(4.7). The equivalence of (4.6)–(4.7) and (4.9)–(4.10) is proved in Appendix B.

The duty-ratio commands for the individual oscillators are generated using droop control. The droop relation for the jth buck converter yields the following voltage reference:

$$V_{\text{ref}j} = V_{\text{nom}} - mi_j, \tag{4.11}$$

where $m > 0$ is the droop slope, and V_{nom} is the nominal output voltage. The buck converter achieves the target voltage ($V_{\text{ref}j}$) through a proportional-integral (PI) regulator with a feedthrough term. In particular, the duty cycle is governed by

$$V_{\text{dc}} D_j = k_p \left(V_{\text{ref}j} - v_{\text{out}}\right) + \int k_i \left(V_{\text{ref}j} - v_{\text{out}}\right) dt + V_{\text{ref}j}, \tag{4.12}$$

where k_p and k_i are the proportional and integral gains respectively, and v_{out} is the output voltage (see Fig. 4.2). In typical implementations, k_p and k_i are picked so that the duty-ratio commands vary on a much slower timescale in comparison to the switching period [3].

A variety of other advanced outer-loop control techniques have been proposed in the literature that improve attributes such as transiest response, current distribution, and output-voltage regulation [133, 134]. Along these lines, accurate current sharing is critical in multiphase architectures since it can prevent inductor saturation and limit thermal stress [135]. With that being said, the approach to interleaving the switching waveforms is decoupled from—and hence agnostic to—outer-loop control strategies; in this work, the classical droop-control strategy discussed above is adopted without loss of generality.

With the feedback strategy adopted in (4.6)–(4.7), and droop control for generating the

duty cycle shown in (4.12), it emerges that the dynamics in (4.5) boil down to the following:

$$\begin{aligned}\dot{\overline{r}}_j &= h_j(\overline{r}_j) \ - \varepsilon\omega_{\rm sw}R_{\rm Th}\sqrt{\xi^2+\chi^2}\sum_{k=1}^{N}\zeta_k\cos(\overline{\theta}_{jk}+\delta),\\ \dot{\overline{\theta}}_j &= \frac{\varepsilon\omega_{\rm sw}R_{\rm Th}\sqrt{\xi^2+\chi^2}}{\overline{r}_j}\sum_{k=1}^{N}\zeta_k\sin(\overline{\theta}_{jk}+\delta),\end{aligned} \tag{4.13}$$

where $\overline{\theta}_{jk} := \overline{\theta}_j - \overline{\theta}_k$, and

$$\zeta_j := \frac{V_{\rm dc}\sin(D_j\pi)\kappa}{\pi L_{\rm f}}\frac{L_{\rm f}^2}{(\omega_{\rm sw}L_{\rm f})^2+R_{\rm f}^2}, \tag{4.14}$$

$$h_j(\overline{r}_j) := \frac{\varepsilon\omega_{\rm sw}}{2}\left(\sigma\overline{r}_j - 3\alpha\overline{r}_j^3 + 2\zeta_j\right), \tag{4.15}$$

$$\xi := \frac{\psi_1\left(1+\eta\right)^{-1}}{\omega_{\rm sw}L_{\rm f}\left(1-\psi_1\left(1+\eta\right)^{-1}\psi_2\right)}, \tag{4.16}$$

$$\chi := \frac{\left(1-\eta\right)^{-1}}{\omega_{\rm sw}L_{\rm f}\left(1-\psi_1\left(1+\eta\right)^{-1}\psi_2\right)}, \tag{4.17}$$

$$\delta := \sin^{-1}\left(\frac{\xi}{\sqrt{\xi^2+\chi^2}}\right), \tag{4.18}$$

with η, ψ_1, and ψ_2 given by:

$$\eta := \left(1-\frac{1}{\omega_{\rm sw}^2R_{\rm load}C_{\rm load}}\right)^{-1}\frac{N}{\omega_{\rm sw}^2C_{\rm load}L_{\rm f}}, \tag{4.19}$$

$$\psi_1 := \frac{R_{\rm f}+NR_{\rm Th}}{\omega_{\rm sw}L_{\rm f}} - \frac{\eta}{\omega_{\rm sw}R_{\rm load}C_{\rm load}}, \tag{4.20}$$

$$\psi_2 := -\frac{R_{\rm f}+NR_{\rm Th}+NR_{\rm load}}{\omega_{\rm sw}L_{\rm f}} + \eta\omega_{\rm sw}R_{\rm load}C_{\rm load}. \tag{4.21}$$

The derivation of the model in (4.13) hinges on the equivalence between the feedback and PWM carrier wave construction in (4.6)–(4.7) to that in (4.9)–(4.10) as shown in Appendix A. Building on this, integration by parts is used and a suite of circuit-theoretic notions including: i) Kirchhoff's voltage law to describe the network dynamics, ii) dynamics of the load voltage, iii) a Fourier-series representation of the switching signal, and iv) the input-output behavior of the dc-dc buck converters to arrive at (4.13). A sketch of this derivation is provided in Appendix B.

4.2 Equilibria and Stability

In this section, different equilibria that result from the collective dynamics in (4.13) are enumerated and subsequently the stability of each is discussed. To that end, first a dynamical model is established that collects and compactly represents all the individual oscillator dynamics in (4.13).

To evaluate stability of different equilibria in the following, further assume that $D_j = D_k$, $\forall j,k \in \mathcal{N}$, which is true in the averaged sense and for time horizons pertinent to stability analysis of the interleaved state. From (4.14), we see that this implies $\zeta_j = \zeta_k =: \zeta$, $\forall j,k \in \mathcal{N}$, which further renders $h_j(\overline{r}_j) =: h(\overline{r}_j)$, $\forall j \in \mathcal{N}$. Furthermore, also suppose $\delta = 0$, which translates to an ideal setup where the Thévenin resistance on the load side is negligibly small, and the switching frequency is high (see (4.18)). With these assumptions in place, the dynamics (4.13) can be compactly and collectively expressed as:

$$\dot{\overline{r}} = H - \rho C 1_N\,, \quad \dot{\overline{\theta}} = \rho R^{-1}\, S 1_N, \tag{4.22}$$

where $\overline{r} = [\overline{r}_1, \ldots, \overline{r}_N]^{\mathrm{T}}$, $\overline{\theta} = [\overline{\theta}_1, \ldots, \overline{\theta}_N]^{\mathrm{T}}$, and $H \in \mathbb{R}^N$, $N \times N$ real matrices R, C, S, and $\rho \in \mathbb{R}$ are given by:

$$[H]_j = h(\overline{r}_j), \quad R = \mathrm{diag}\{\overline{r}\}\,, \tag{4.23}$$

$$[C]_{j\ell} = \cos(\overline{\theta}_{jl}), \quad [S]_{j\ell} = \sin(\overline{\theta}_{jl})\,, \tag{4.24}$$

$$\rho = \varepsilon \omega_{\mathrm{sw}} R_{\mathrm{Th}} \zeta \sqrt{\xi^2 + \chi^2}. \tag{4.25}$$

To clarify the notation above, $[X]_{jk}$ represents the entry in the jth row and kth column of matrix X; for vector x, $\mathrm{diag}\{x\}$ denotes the diagonal matrix obtained by stacking elements of x on the main diagonal; and 1_N denotes the length-N vector with all ones.

Notice that the phase dynamics in (4.22) are not defined for $\overline{r}_j = 0$; and indeed, the very notion of a radius is ill-posed when $\overline{r}_j \leq 0$. Hence, first conditions such that the radii remain greater than zero are established. In particular, when the number of oscillators are upper bounded as follows:

$$N < \frac{1}{R_{\mathrm{Th}} \sqrt{\xi^2 + \chi^2}}, \tag{4.26}$$

the set

$$\mathcal{I} := \{(\overline{r}, \overline{\theta}) \in \mathbb{R}^N_{\geq 0} \times \mathbb{T}^N : \overline{r}_j > 0, \forall j \in \mathcal{N}\}, \tag{4.27}$$

where $\mathbb{T}^N$ denotes the N-dimensional torus is positively invariant with the designed feed-

back (4.6). To see this, consider that from the amplitude dynamics in (4.22):

$$\begin{aligned}\dot{\overline{r}}_j &= \varepsilon\omega_{\text{sw}}\left(\frac{\sigma\overline{r}_j - \alpha\overline{r}_j^3}{2} + \zeta - R_{\text{Th}}\sqrt{\xi^2+\chi^2}\sum_{k=1}^{N}\zeta\cos(\overline{\theta}_{jk})\right) \\ &\geq \frac{\varepsilon\omega_{\text{sw}}}{2}\left(\sigma\overline{r}_j - \alpha\overline{r}_j^3\right) + \varepsilon\omega_{\text{sw}}\zeta\left(1 - NR_{\text{Th}}\sqrt{\xi^2+\chi^2}\right).\end{aligned} \tag{4.28}$$

So, if (4.26) holds then

$$\dot{\overline{r}}_j \geq \frac{\varepsilon\omega_{\text{sw}}}{2}\left(\sigma\overline{r}_j - \alpha\overline{r}_j^3\right) + r_\circ, \tag{4.29}$$

where $r_\circ$ is a positive constant. Clearly $\forall\ \overline{r}_j < \sqrt{\sigma/\alpha}$, $\dot{\overline{r}}_j > 0$, which renders $\mathcal{I}$ to be positively invariant.

From the above discussion, it is implied that R has all positive entries. At equilibrium, where $\dot{\overline{\theta}} = 0_N$ (0_N denotes the length-N vector with all zeros), from (4.22) it is implied that

$$S1_N = 0_N. \tag{4.30}$$

Given the definition of matrix S in (4.24), one can identify different types of equilibria that satisfy the constraint in (4.30) (sketched on the phase plane in Fig. 4.3): a) bi-cluster synchronous state, b) phase-synchronous state, c) generalized interleaved state, and d) symmetric-interleaved state: the desired state where the phases of the PWM carriers are uniformly spaced apart. These are formally defined and studied next, and in each case, it is *validated* that the phases indeed satisfy the constraint for equilibria, namely (4.30).

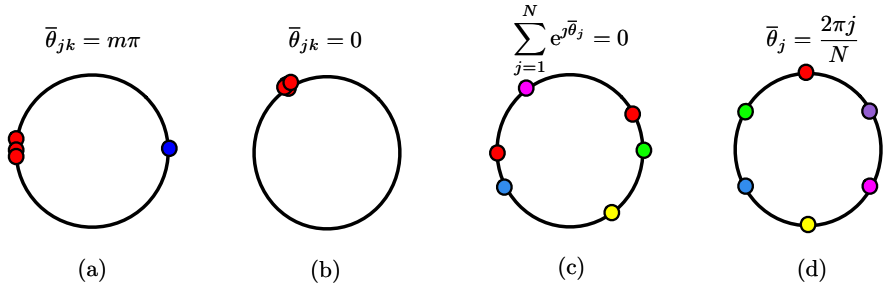

Figure 4.3: Equilibria for the coupled oscillator dynamics (4.22): a) bi-cluster synchronous state, b) phase-synchronous state, c) generalized interleaved state, and d) symmetric-interleaved state. Recall that $\overline{\theta}_j$ is the averaged phase-angle offset (with respect to a nominal reference frame rotating at the switching frequency) corresponding to the voltage of the virtual capacitor, v_{Cj} (and hence of its corresponding carrier waveform) for the j-th oscillator. Furthermore, $\overline{\theta}_{jk} = \overline{\theta}_j - \overline{\theta}_k$. (Source: [30])

4.2.1 Bi-cluster Synchronous State

The coupled system is said to be in the bi-cluster synchronous state if the phases evolve as

$$\overline{\theta}_j - \overline{\theta}_k = m\pi,\ \forall j,k \in \mathcal{N}, \forall m \in \mathbb{Z}. \tag{4.31}$$

The bi-cluster synchronous state is illustrated in Fig. 4.3(a).

Validity

To see that this is indeed an equilibrium, note from (4.24) that $[S]_{j\ell} = \sin(\overline{\theta}_{jl}) = 0$, $\forall j,k \in \mathcal{N}$ when $\overline{\theta}_j - \overline{\theta}_k = m\pi$, $\forall m \in \mathbb{Z}$. This further implies that phases defined by (4.31) satisfy $S1_N = 0_N$, and hence the bi-cluster synchronous state is an equilibrium of the dynamics (4.22).

Stability

Using linearization-based arguments, it can be shown that this bi-cluster synchronous state is locally unstable unless the number of oscillators in the two clusters are equal. To establish this, consider that the Jacobian of the linearized version of (4.22) around equilibria $\overline{\theta}_j - \overline{\theta}_k = m\pi$, where $m \in \mathbb{Z}$, has the following block-diagonal form:

$$J = \left[\begin{array}{c|c} J_{\mathrm{A}} & 0_{N\times N} \\ \hline 0_{N\times N} & J_{\mathrm{D}} \end{array}\right], \tag{4.32}$$

where $0_{N\times N}$ is the $N \times N$ matrix with all entries equal to 0. The entries of J_{A} and J_{D} are specified as:

$$\begin{aligned} \Big[J_{\mathrm{A}}\Big]_{j\ell} &= \begin{cases} h'(\overline{r}_j^*) & \text{if } j = \ell \\ 0 & \text{if } j \neq l \end{cases} \\ \Big[J_{\mathrm{D}}\Big]_{j\ell} &= \begin{cases} -\frac{\rho}{\overline{r}_j^*} & \text{if } j \neq l\ ,\ \overline{\theta}_{j\ell} = 2m\pi \\ \frac{\rho}{\overline{r}_j^*} & \text{if } j \neq l\ ,\ \overline{\theta}_{j\ell} = (2m+1)\pi \\ -\sum_{\ell=1,\ell\neq j}^{N} [J_{\mathrm{D}}]_{j\ell} & \text{if } j = \ell, \end{cases} \end{aligned} \tag{4.33}$$

where $m \in \mathbb{Z}$ and $\overline{r}_j^*$ is the equilibrium radius for the jth oscillator. Since J is block diagonal, its eigenvalues are those of J_{A} and J_{D}. In the following, the focus is on the analysis on the eigenvalues of J_{D}. Since $\overline{\theta}_j - \overline{\theta}_k = m\pi$, the phases of the oscillators belong to one of the two clusters on the circle (depending on whether m is odd or even). Two cases need attention:

i) The sizes of the two clusters differ by more than one: Denote e_j to be the length-N unit basis vector with 1 at the jth entry and zeros elsewhere. Denote ℓ to be the index of any node in the bigger cluster. The diagonal entries of J_{D} corresponding to oscillators in the bigger cluster are positive, and since $e_\ell^{\mathrm{T}} J_{\mathrm{D}} e_\ell > 0$, it is not negative semidefinite, therefore J_{D} must have at least one positive eigenvalue [73].
ii) The sizes of the clusters differ by one: The diagonal entries are either 0 (for the nodes in the bigger cluster) or -2 (for the nodes in the smaller cluster). Thus, there exists a symmetric principal minor of order 2 (corresponding to two nodes in distinct clusters) of the form

$$\frac{\rho}{2} \cdot \begin{bmatrix} 0 & \pm 1 \\ \pm 1 & -2 \end{bmatrix}$$

which features a positive eigenvalue. Therefore J_{D} cannot be negative semidefinite [73] in this case as well.

In conclusion, J_{D} (and hence, J) has at least one eigenvalue with positive real part. This establishes the local instability of clusters where the phase equilibria satisfy: $\overline{\theta}_j - \overline{\theta}_k = m\pi$ and the number of oscillators in each cluster is not the same.

4.2.2 Phase-synchronous State

This corresponds to the state where the phases of all oscillators are perfectly synchronized:

$$\overline{\theta}_j = \overline{\theta}_k, \ \forall j, k \in \mathcal{N}. \tag{4.34}$$

This state is illustrated in Fig. 4.3 (b). Note that it is recovered as a special case from the bi-cluster synchronous state for $m = 0$.

Validity

To see that this is indeed an equilibrium, note from (4.24) that $[S]_{j\ell} = \sin(\overline{\theta}_{jl}) = 0$, $\forall j, k \in \mathcal{N}$ when $\overline{\theta}_j = \overline{\theta}_k$. This further implies that phases defined by (4.34) satisfy $S1_N = 0_N$, and hence the phase-synchronous state is indeed an equilibrium of the dynamics (4.22).

Stability

Notice that the phase-synchronous state is recovered from the bi-cluster synchronous state when $m = 0$. Therefore, the stability result from Section 4.2.1 applies in this case as well. In particular, for the case $m = 0$, J_{D} in (4.33) is a Laplacian matrix of a complete graph

and therefore is positive semidefinite. This establishes that the phase-synchronous state is locally unstable.

4.2.3 Generalized Interleaved State

This is a generalized notion of the symmetric interleaved state, and captures the setting where the phases of the oscillators evolve functionally constrained as follows

$$\sum_{j=1}^{N} \mathrm{e}^{\jmath\overline{\theta}_j} = 0, \tag{4.35}$$

where $\jmath = \sqrt{-1}$. This state is also known as the phase-balanced state, and it is widely studied in the coupled-oscillator literature [44]. Closer to the application at hand, it was investigated for an asymmetric interleaving application [7] where the first harmonic was eliminated to minimize the current ripple. The generalized interleaved state is illustrated in Fig. 4.3 (c).

Validity

Unlike the bi-cluster synchronous state and the phase-synchronized state, in this case, S is not a null matrix and therefore condition (4.30) is not satisfied trivially. Nonetheless, it turns out that when S is not a null matrix then $S1_N = 0_N$ if and only if $C1_N = 0_N$. (See Lemma 4 in Chapter 2.) For the generalized interleaved state where $\sum_{j=1}^{N} \mathrm{e}^{\jmath\overline{\theta}_j} = 0$, it is true that $C1_N = 0_N$ *and* $S1_N = 0_N$, and therefore, this indeed corresponds to an equilibrium of the phase dynamics in (4.22).

Stability

Construct a directed graph to establish the nature of equilibria in the oscillator dynamics (4.22). Let N nodes of the graph denote the oscillators and if the vector field governing $\dot{\overline{\theta}}_j$ has a $\overline{\theta}_{jk}$ term (i.e., the evolution of the jth oscillator dynamics depends on the dynamics of the kth oscillator), then there is an edge between nodes j and k. The phase dynamics in (4.22) can be compactly recast as follows:

$$\dot{\overline{\theta}} = R^{-1} B \sin(B^{\mathrm{T}} \overline{\theta}), \tag{4.36}$$

where $B \in \mathbb{R}^{N \times \binom{N}{2}}$ is the edge-oriented incidence matrix of the underlying complete graph. Furthermore, with regard to notation, for $\theta = [\theta_1, \ldots, \theta_N]^{\mathrm{T}} \in \mathbb{T}^N$, $\sin(\theta) := [\sin(\theta_1), \ldots, \sin(\theta_N)]^{\mathrm{T}}$,

and $\cos(\theta) := [\cos(\theta_1), \ldots, \cos(\theta_N)]^{\mathrm{T}}$.

Introduce a coordinate change to $\widetilde{\theta} = B^{\mathrm{T}}\overline{\theta} \in \mathbb{R}^{\binom{N}{2}}$, that captures angle differences between the oscillators. In this new set of coordinates, the phase dynamics can be written as:

$$\dot{\widetilde{\theta}} = \rho B^{\mathrm{T}} R^{-1} B \sin \widetilde{\theta}\,. \tag{4.37}$$

Consider the following potential function

$$V(\overline{r}, \widetilde{\theta}) = -\sum_{j=1}^{N} \int_0^{\overline{r}_j} h(s)ds + 1_N^{\mathrm{T}} RB \cos \widetilde{\theta}, \tag{4.38}$$

from which, it follows that

$$\dot{V}(\overline{r}, \widetilde{\theta}) = -\left(H - \rho B \cos \widetilde{\theta}\right)^2 - \rho (\sin \widetilde{\theta})^{\mathrm{T}} B^{\mathrm{T}} R R^{-1} B \sin \widetilde{\theta}.$$

Notice that $\dot{V}(\overline{r}, \widetilde{\theta}) \leq 0$, since it is the sum of two quadratic terms with a negative leading sign. Thus, the sublevel sets of V are compact (closed due to continuity and bounded as $V(\overline{r}, \widetilde{\theta})$ is radially unbounded).

Finally, by LaSalle's invariance principle [59], all trajectories starting in $\mathcal{I}$ (defined in (4.27)) converge to the subset identified by $\dot{V} = 0$, i.e., amplitudes and phases are such that $B \sin \widetilde{\theta} = 0_N$ (which is true if and only if $S1_N = 0_N$ which implies $C1_N = 0$ when S is not a null matrix) and $H - \rho C 1_N = 0$ (which gives $H = 0_N$ when S is not a null matrix). As discussed earlier, $S1_N = 0_N$, either gives rise to the bi-cluster synchronous state (of which the phase-synchronous state is a special case) or the generalized interleaved state. It has already been established that the bi-cluster synchronous state is locally unstable. Therefore, almost all trajectories must eventually converge to the generalized interleaved state.

4.2.4 Symmetric-interleaved State

The multiphase system is said to be in a symmetric interleaved state if the phases of the coupled oscillators evolve uniformly spaced apart as follows:

$$\overline{\theta}_j = j\frac{2\pi}{N} + \theta_\circ \pmod{2\pi}, \forall j \in \mathcal{N}, \quad 0 \leq \theta_\circ \leq 2\pi. \tag{4.39}$$

The symmetric interleaved state is illustrated in Fig. 4.3(d).

Validity

It was established previously that the generalized interleaved state (where phases are governed by (4.35)) is indeed an equilibrium of the phase dynamics (4.22). Notice that the symmetric-interleaved state, where phases are governed by (4.39) is a special case of the generalized interleaved state, and therefore satisfies the condition (4.30) as well.

Stability

To establish whether the interleaved state is locally stable, the amplitude and phase dynamics from (4.22) are shifted to the origin as follows:

$$\mu_j = \overline{r}_j - \overline{r}^*, \quad \varphi_j = \overline{\theta}_j - j\frac{2\pi}{N}, \tag{4.40}$$

where $\overline{r}^*$ denotes the equilibrium radius which solves $h(\overline{r}^*) = 0$. Now, the dynamics of the coupled system (4.22) around this equilibrium can be written as:

$$\begin{aligned} \dot{\mu}_j &= h(\overline{r}^* + \mu_j) \ - \rho \sum_{k=1}^{N} \cos\left(\frac{2\pi(j-k)}{N} + \varphi_{jk}\right), \\ \dot{\varphi}_j &= \frac{\rho}{\overline{r}^* + \mu_j} \sum_{k=1}^{N} \sin\left(\frac{2\pi(j-k)}{N} + \varphi_{jk}\right), \end{aligned} \tag{4.41}$$

where $\varphi_{jk} := \varphi_j - \varphi_k$. Leveraging the fact that μ_j and φ_{jk} are small quantities as it captures the behavior around the neighborhood of the interleaved state, and therefore, $\sin\varphi_{jk} \approx \varphi_{jk}$, $\cos\varphi_{jk} \approx 1$ and $(\overline{r}^* + \mu_j)^{-1} \approx \frac{1}{\overline{r}^*}(1 - \frac{\mu_j}{\overline{r}^*})$. With these simplifications in place and ignoring second-order terms like $\mu_j\varphi_{jk}$, the phase dynamics reduce to:

$$\dot{\varphi} = \frac{\rho}{\overline{r}^*} J\varphi, \tag{4.42}$$

where $\varphi := [\varphi_1, \ldots, \varphi_N]^{\mathrm{T}} \in \mathbb{T}^N$ and J is a symmetric circulant matrix with entries given by:

$$[J]_{j\ell} = \begin{cases} -1 & \text{if } j = \ell \\ -\cos\left(\frac{2\pi}{N}(j-\ell)\right), & \text{if } j \neq \ell. \end{cases} \tag{4.43}$$

Table 4.1: Specifications, parameters, and ratings for the experimental prototype. (Source: [30])

Power Stage Hardware	48 V to 12 V step-down, 120 W per converter
L_{f}	141.6 μH $\pm$10%
R_{f}	13.70 mΩ
C_{load}	1100 μF $\pm$20%
R_{Th}	0.1 Ω $\pm$5%
R_{load}	1.6 Ω $\pm$10%
R_{par}	50 mΩ $\pm$5%
Switching frequency	20 kHz
MOSFET	Fairchild FDB035N10A
Gate driver	Silicon Labs SI8234
Current sensors	Allegro ACS730KLCTR
Voltage sensors	Broadcom ACPL-C87AT
Control Stage Hardware	
Device	Xilinx Artix-7 XC7A35T-L1CSG324I FPGA
Controller time step	150 ns
ADC sampling rate	500 kHz

Oscillator parameters	
σ	$90\,\Omega^{-1}$
α	$60\,\mathrm{A/V^3}$
L	$0.61\,\mu$H
C	$16.67\,\mu$F
Droop controller parameters	
k_p	$0.32\,\mathrm{V/V}$
k_i	$0.06\,\mathrm{s^{-1}}$
m	$1.5\,\mathrm{V/A}$
V_{nom}	$12\,\mathrm{V}$

Since J is a circulant matrix, its eigenvalues are given by

$$\lambda_j(J) = \sum_{k=0}^{N-1} \cos\left(\frac{2\pi k}{N}\right) \Omega_j^k, \tag{4.44}$$

where $\Omega_j = \mathrm{e}^{\jmath 2\pi j/N}$ denotes one of the N-th roots of unity. Notice that two of these eigenvalues are $-N/2$ and the rest are zero. Thus, the linearized phase dynamics around the symmetrically interleaved equilibrium are marginally stable.

4.3 Experimental Validation

The proposed approach is validated with a hardware prototype of parallel-connected dc-dc buck converters with independent FPGA controllers as shown in Fig. 4.5. The prototype consists of five independent converters rated at 120 W each, stepping down from 48 V to

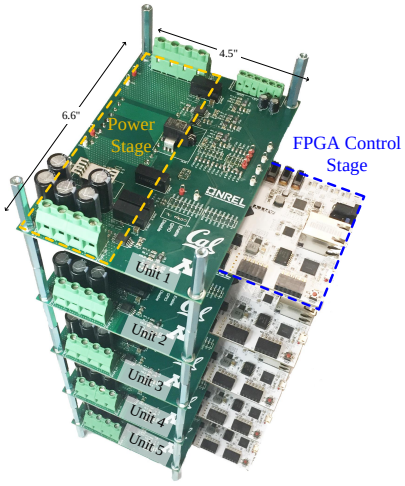

Figure 4.4: Photograph of the experimental prototype: five dc-dc converters and associated controller boards. Note that there is no communication between controllers. (Source: [30])

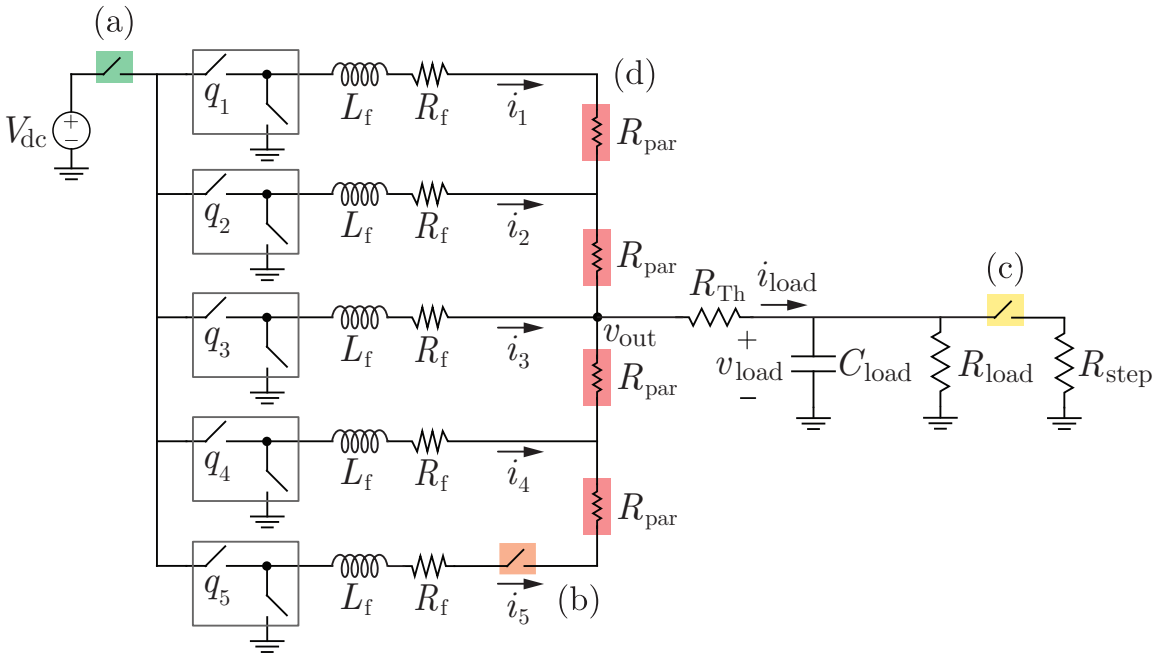

Figure 4.5: Circuit diagram illustrating experiments performed: (a) start up from arbitrary initial conditions, (b) addition of one converter to system, (c) load step, (d) unit addition in non-symmetric network with parasitics (in this case, converters continue to sense local output voltages for droop control even though this is not explicitly depicted in the figure). (Source: [30])

12 V at 20 kHz. The parameters for the controllers along with specifications and ratings of the prototype are listed in Table 4.1. In this section, the design procedure is outlined that was followed to select the oscillator (controller) and converter parameters listed in Table 4.1., following which experimental results are provided.

4.3.1 System Parameters and Controller Design

The oscillator parameters L and C are tuned to the switching frequency, i.e. $1/\sqrt{LC} = \omega_{\text{sw}} = 2\pi \times 20\,\text{rad/s}$ while maintaining the quasi-harmonic regime, i.e., $\sqrt{L/C} = \varepsilon \ll 1$. $\varepsilon = 0.19$ is chosen for the implementation. Setting $\sigma > 0$ satisfies the Liénard condition for sustaining oscillations [124], and $\alpha = 2\sigma/3$ yields a sinusoidal oscillation of unit amplitude for the oscillators which aids in regularizing the design. The current gain $\kappa > 0$ is necessary for interleaving and is chosen to be 10. (Empirically, it is observed that very small values of κ result in slow convergence to the equilibrium state, while very large values of κ induce non-sinusoidal oscillator states with no convergence guarantees.) The droop controller gains k_p and k_i are selected so that the time constant of the controller is about 5 s and there is a clear time-scale separation from the switching period. Furthermore, for each individual buck converter, L_{f} was selected to guarantee continuous conduction mode at the selected operating point and C_{load} is just sufficiently large to establish a constant voltage at the load side. Finally, it is also verified that the sufficient positive invariance condition (4.26) derived in Section 4.2 is met so that phase dynamics are well-posed, i.e., $NR_{\text{Th}}\sqrt{\xi^2 + \chi^2} < 1$. Notice that in the ideal setup as $R_{\text{Th}} \to 0$, the condition is always satisfied for all N. The current setup with the chosen physical parameters satisfies this condition up to 41 units.

Tolerances of various components utilized in the hardware setup are also listed alongside nominal values in Table 4.1. While the analysis presumed an ideal and symmetric setup, the experimental results provided subsequently establish the robustness of the approach to a variety of parametric variations (including the ones in Table 4.1 that are readily quantifiable through values from datasheets).

Jason conducted four experimental tests to validate the performance and robustness of the proposed interleaving control method: a) start up of five units from arbitrary initial conditions, b) addition of one unit to four units in steady state, c) a load step applied to five units in steady state, d) unit addition to a non-symmetric network with lossy lines. The setup and experiments performed listed above are sketched in Fig. 4.4. Next, results from these experiments demonstrate that, in each case, the proposed controller ensures interleaving in steady state without any communication between converters.

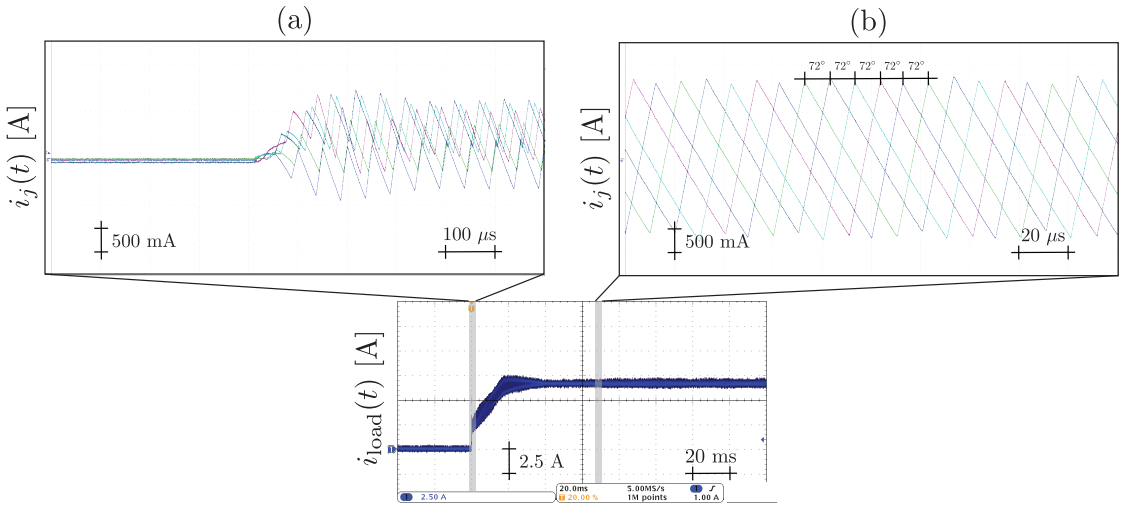

Figure 4.6: Five buck converters are started from arbitrary initial conditions with the designed oscillator-based controllers (a). The system achieves symmetric interleaving with $72° = 360°/5$ phase spacing and the droop controller maintains balanced currents in each of the five units in steady state (b). (Source: [30])

4.3.2 Start Up from Arbitrary Initial Conditions

First, the start-up scenario in which five units are initiated simultaneously is considered, each with arbitrary initial conditions. The dynamics of the load current and the ac components of the phase currents for this case are shown in Fig. 4.6. The phase currents, i_j, of the individual converters at the turn-on instant are arbitrarily spaced, which results in a larger ripple in i_{load}. After approximately 40 ms, the phase currents of the five converters settle to the interleaved state with $72° = 360°/5$ phase offset and the ripple in i_{load} is visibly reduced.

4.3.3 Unit Addition

Next, to demonstrate the plug-and-play nature of the proposed control strategy, the system performance is investigated when an additional converter is added. As shown in Fig. 4.7, the system is initialized in steady state with four parallel units with phase currents that are $90° = 360°/4$ out of phase with adjacent units. After adding an additional fifth unit, the system reaches the interleaved state in approximately 6 ms with each phase current now $72°$ ($360°/5$) out of phase with adjacent units. The benefits of interleaving with additional units are also evident in reducing load-current ripple. Again, the droop controller successfully maintains current sharing before and after the addition of the fifth unit.

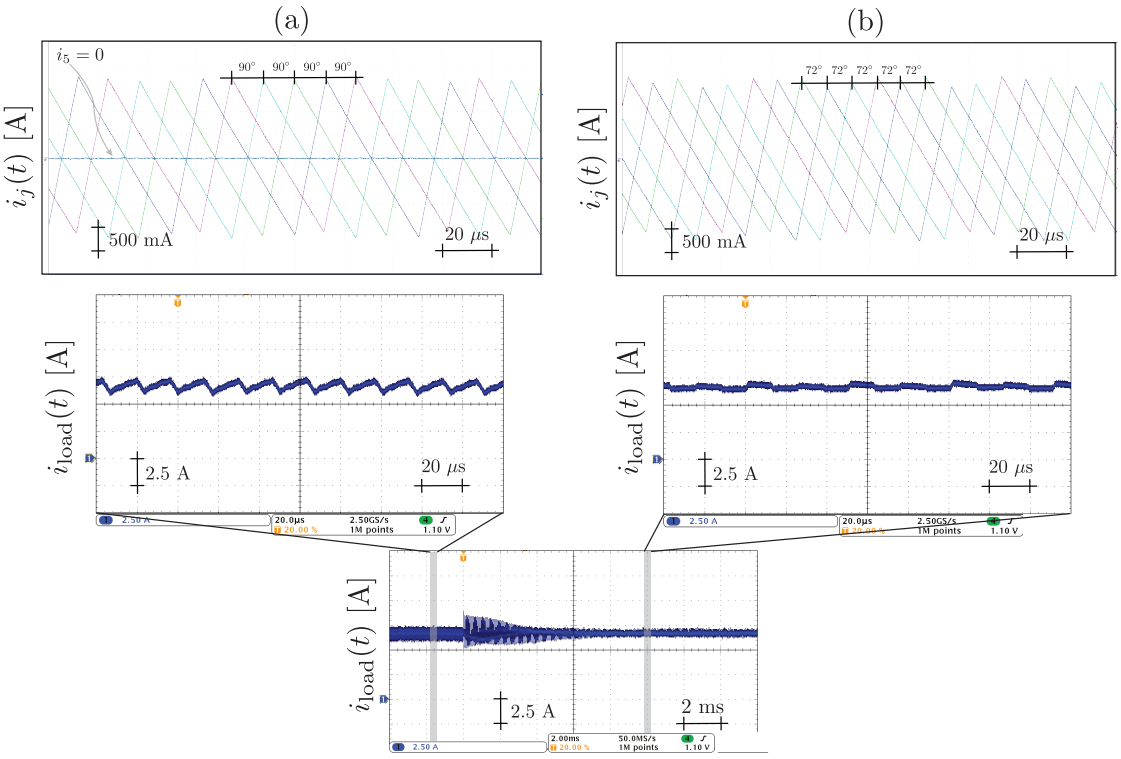

Figure 4.7: One additional buck converter unit is added to four functioning units. The phase currents i_j automatically transition from having $90° = 360°/4$ phase shift (a) to $72° = 360°/5$ phase shift (b). (Source: [30])

4.3.4 Load Step

A load step was experimentally implemented to validate the robustness of the control method to typical operating transients. As shown in Fig. 4.8, the load is changed from $R_{\text{load}} = 1.6\ \Omega$ to $R_{\text{load}} = 1.3\ \Omega$ at $t = 0$ with five units connected. The system maintains the interleaved state before and after the transient, as indicated by the unchanged ripple magnitude in i_{load} and the unchanged 72° phase shift in phase currents i_j.

4.3.5 Non-ideal Output Parallel Configuration

Lastly, in order to validate the robustness of the proposed method to non-idealities in the parallel output configuration, the circuit shown in Fig. 4.4 was implemented, where deliberately introduced resistors R_{par} induce a nontrivial output impedance to each converter. This eliminates the ideal parallel connection between the dc-dc converters. With this circuit, the task of adding one unit to four units in steady state was executed. As shown in Fig. 4.9,

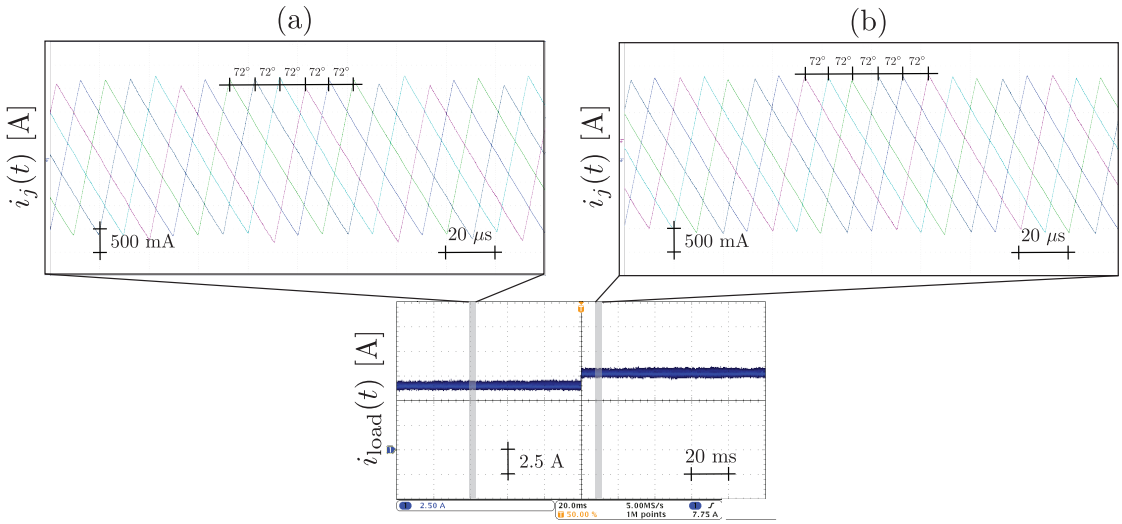

Figure 4.8: To evaluate the robustness to load variations, a load step from $R_{\text{load}} = 1.6\ \Omega$ (a) to $R_{\text{load}} = 1.3\ \Omega$ (b) at $t = 0$ is introduced with five units in steady state. The convergence to the new steady state is almost instantaneous and the system maintains the symmetric interleaved state with $72° = 360°/5$ phase spacing between converters. (Source: [30])

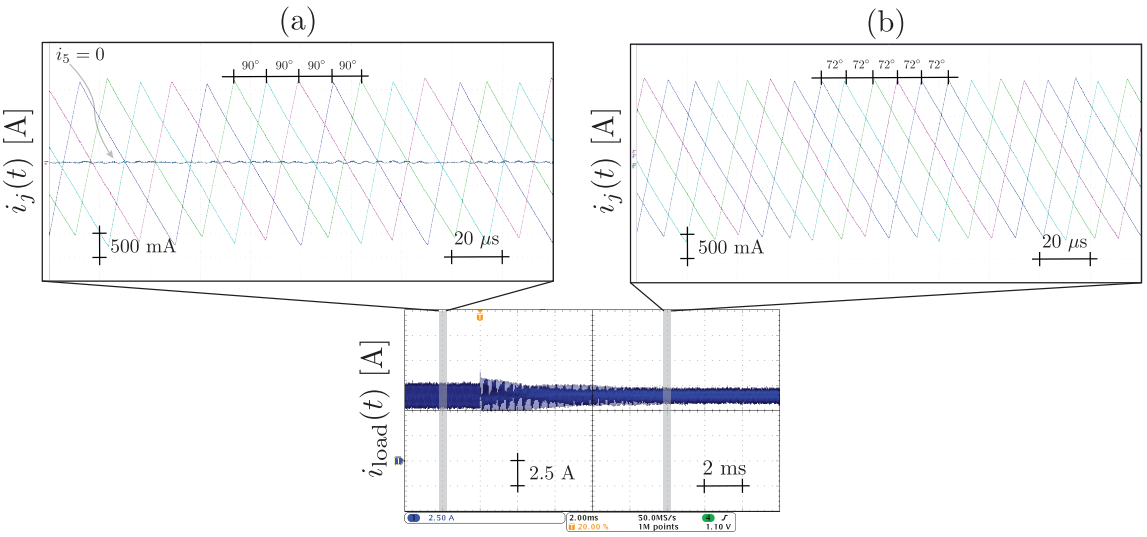

Figure 4.9: Addition of one unit to four units in steady state with the non-symmetric setup and lossy network shown in Fig. 4.4. The phase currents i_j automatically transition from having $90°(360°/4)$ phase shift (a) to $72°(360°/5)$ phase shift (b). (Source: [30])

four units are initially interleaved with $90° = 360°/4$ degree phase shift in currents. When the fifth unit is added, the system reaches the new interleaved state after approximately

8 ms, at which point the phase shifts automatically adjust to $72^\circ = 360^\circ/5$. Notice from the figure that the ripple in load current reduces with the additional unit. The presence of the non-idealities does increase the ripple (compared to the test shown in Fig. 4.7) by approximately 50%. Regardless, this test has demonstrated the robustness of the method to achieve interleaving even in the presence of modestly large non-idealities in the output loading configuration. Moreover, these non-idealities have minimal impact on the droop controller and its ability to ensure current sharing between the units.

Chapter 5

Conclusions and Future Research

The thesis develops tools for control, modeling and analysis of power electronic converters connected via an electrical network. It tackles two key relevant problems in networks of inverters and dc-dc converters in a decentralized way in order to support modular plug-n-play paradigm that allows seamless interconnection. First problem is of inverter control in low-inertia microgrids tackled in Chapter 3, where sustainable energy resources such as photovoltaic (PV) arrays, microwind turbines, and fuel cells are interfaced through autonomously controlled power-electronic inverters, and any uncertainty in supply is managed by energy storage devices. This is motivated by the pressing need to adapt the real-time control algorithms to allow high renewable integration that impose variable ambient conditions and fluctuating loads. Migrating to these energy system of the future poses significant operational challenges in the form of low inertia stability & power quality maintenance, adoption of ad hoc networks & plug-n-play control, and robustness & distributed implementation. With a view towards meeting these challenges, a suite of methods called virtual oscillator control is considered here, which is implemented by programming a weakly nonlinear Liénard-type oscillator on the inverter micro-controller and using its states to construct the reference wave in the sine pulse width modulation (PWM) for switching in the inverter while getting the current output at the inverter terminals as the feedback. One major contribution of the research presented here has been to establish a link between virtual oscillator control and the classical droop laws. By leveraging arguments from theory of averaging for slowly varying time periodic vector fields, a droop-like interpretation of the nonlinear control strategy is recovered that allows to outline a comprehensive design procedure for synthesis of virtual oscillators in a way that incorporates steady state regulation, control of harmonic content and quantification of dynamic response in terms of rate of convergence.

Furthermore, this also renders the virtual oscillator control backwards compatible and therefore decades of work on droop control and its variants could conceivably be used to inform the design of these time domain controllers. Additionally, based on these droop-like models for oscillator-based inverters, stability certificates are derived to showcase convergence to solutions when starting initially within a specified set and their exponential stability under various operating conditions. In addition to guaranteeing stability in power electronics dominant microgrids with high renewable penetration, it is equally important to ascertain that the control algorithms enable operation with high efficiency. So, developing performance metric based analysis for oscillator-based controllers is an exciting direction for future work. In this regard, robust control based metrics H_2 and H_∞ have been recently applied to droop controllers in microgrids to analyze the performance in various operating scenarios as well as to design their improved versions. However, the studies are still in their infancy and use restrictive modeling assumptions to derive the results. Treading on a similar path could lead to subsequent improvement in the time-domain controllers proposed here. Furthermore, the impact of rotational inertia on the stability boundaries of a mixed microgrid with inverters and machines is also poorly understood and has been a recent matter of significant concern with proposals of offering inertia as an ancillary service being considered at various places. Virtual inertia emulation and their optimal placement is being aggressively explored and recent trends suggest that the power electronic interfaces, coupled with well designed algorithms, do not require the presence of a physical inertia in the system to guarantee stable operation with well-behaved transients. Towards that end, quantifying the performance of various controllers in low-inertia settings rigorously can pave a way for better controllers and ultimately towards large scale generation without the presence of machines to deal with transients. Finally, the conventional hierarchical operation of bulk power systems is not suited for distributed generation and breaking the time scale separation to optimize on a composite objective of economic operation and optimal control also requires a revaluation of the known performance metrics in order to devise relevant measures for the emerging low-inertia networks. Distributed transient frequency controller leveraging set invariance and Lyapunov theory as explored in this dissertation as well as designing feedback controllers that converge to optimal power solutions are promising directions that could augment the findings here and lead to a modern system with flat hierarchy.

The second problem deals with switch interleaving in parallel connected dc-dc converters which enhances power quality and efficiency in parallel converter systems, This involves temporal separation of the pulse width modulation (PWM) carriers of the converters across a given switch cycle to achieve current-ripple cancellation at the load bus and is achieved by

typically maintaining a centralized system-wide timing. While centralized solutions may be appropriate for systems that contain a fixed number of converters, they are inadequate for systems that benefit from modular plug-and-play such as dc microgrids or voltage regulation modules (VRMs). Recognizing the gap, a completely decentralized and communication-free interleaving strategy is devised for a system of parallel connected converters supplying a common load. Again, leveraging the rich dynamical behavior of coupled Liénard-type oscillators, the foundational theory is built for the decentralized control algorithms thereby adapting the interleaving methods towards the modular adhoc architectures, making them more reliable and flexible. The key idea is to construct PWM using a linear combination of states of the nonlinear oscillators and the output currents of each converter unit with current gains appropriately chosen from which interleaving emerges innately from the electrical interconnection. Analytical stability proofs are constructed that guarantee convergence to solutions almost globally and show that the uniformly spaced out state, the so-called *splay state*, is locally stable. The work is timely and aligns perfectly with recent progress in wide-bandgap semiconductors that has facilitated the development of power electronic circuits that operate at large voltage and power levels. In particular, so-called modular multilevel converters, which have received significant attention in recent years, are constructed with interconnected stacks of power electronic modules for large voltage and current applications. Although these circuits have a modular structure, they usually have a centralized controller that manages system-wide timing between units and executes requisite closed-loop control functions due to which scalability and plug-n-play functionality are hindered as the controller must be reconfigured or redesigned as additional modules are added. Decentralized control laws that converge to desired operating conditions without explicit module-to-module communication can, therefore, overcome this limitation and obtain systems that are modular in both construction and control, hence truly scalable in implementation. To this end, system-theoretic notions considered here can permeate benefits to design circuit controllers that converge to the desired equilibria just by virtue of the interconnection. Particular applications include switch interleaving in series connected modular multilevel converters and output current sharing in parallel resonant converters. Ultimately, it is envisaged that these advances in control algorithms shall enable the next-generation of utility-scale electronics for multi-megawatt applications. Another interesting related question that could be asked is of optimal interleaving. It has been recently shown that in a heterogeneous setup with non-identical dc-dc converters serving non-identical loads connected via an electrical network, the symmetric solutions where the carriers are equally spaced part across a switch cycle is sub-optimal and a centralized gradient-based algorithm achieves a significantly bet-

ter performance. Devising controllers that achieve this in a decentralized way is a worthy open problem that, if solved, would propel modular architectures. Finally, for very high-frequency power electronics, digital control becomes a bottleneck due to the restrictions put forth by sampling restrictions on the sensors. Since the oscillators presented admit a circuit realization, developing analog controllers for the power-electronic converters would enable very high-frequency applications and is also a part of the ongoing investigations.

References

[1] D. J. Perreault and J. G. Kassakian, "Distributed interleaving of paralleled power converters," *IEEE Transactions on Circuits and Systems I: Fundamental Theory and Applications*, vol. 44, no. 8, pp. 728–734, Aug 1997.

[2] W. Huang and B. Lehman, "A compact coupled inductor for interleaved multiphase dc–dc converters," *IEEE Transactions on Power Electronics*, vol. 31, no. 10, pp. 6770–6775, Oct 2016.

[3] J. M. Guerrero, J. C. Vasquez, J. Matas, L. G. De Vicuña, and M. Castilla, "Hierarchical control of droop-controlled AC and DC microgrids: A general approach toward standardization," *IEEE Transactions on Industrial Electronics*, vol. 58, no. 1, pp. 158–172, Jan 2011.

[4] M. Schuck and R. C. Pilawa-Podgurski, "Ripple minimization in asymmetric multiphase interleaved dc-dc switching converters," in *IEEE Energy Conversion Congress and Exposition*, Sept 2013, pp. 133–139.

[5] ——, "Current ripple cancellation for asymmetric multiphase interleaved dc-dc switching converters," in *IEEE Power and Energy Conference at Illinois*, 2013, pp. 162–168.

[6] ——, "Input current ripple reduction through interleaving in single-supply multiple-output dc-dc converters," in *14th IEEE Workshop on Control and Modeling for Power Electronics*, 2013, pp. 1–5.

[7] M. Schuck, A. D. Ho, and R. C. Pilawa-Podgurski, "Asymmetric interleaving in low-voltage cmos power management with multiple supply rails," *IEEE Transactions on Power Electronics*, vol. 32, no. 1, pp. 715–722, Jan 2017.

[8] M. Schuck and R. C. Pilawa-Podgurski, "Ripple minimization through harmonic elimination in asymmetric interleaved multiphase dc–dc converters," *IEEE Transactions on Power Electronics*, vol. 30, no. 12, pp. 7202–7214, Dec 2015.

[9] R. W. Erickson and D. Maksimovic, *Fundamentals of power electronics*. Springer Science & Business Media, 2007.

[10] M. H. Rashid, *Power electronics handbook*. Butterworth-Heinemann, 2017.

[11] B. K. Bose, "Power electronics and ac drives," *Englewood Cliffs, NJ, Prentice-Hall, 1986, 416 p.*, 1986.

[12] J. G. Kassakian, M. F. Schlecht, and G. C. Verghese, *Principles of power electronics*. Graphis, 2000.

[13] B. K. Bose, "Power electronics, smart grid, and renewable energy systems," *Proceedings of the IEEE*, vol. 105, no. 11, pp. 2011–2018, Nov 2017.

[14] J. D. Irwin, *Control in power electronics: selected problems*. Elsevier, 2002.

[15] D. Maksimović, R. Zane, and R. Erickson, "Impact of digital control in power electronics," in *Proc. IEEE International Symposium on Power Semiconductor Devices & ICs*, 2004, pp. 13–22.

[16] A. Yazdani and R. Iravani, *Voltage-sourced converters in power systems: modeling, control, and applications*. John Wiley & Sons, 2010.

[17] B. B. Johnson, S. V. Dhople, A. O. Hamadeh, and P. T. Krein, "Synchronization of Parallel Single-Phase Inverters With Virtual Oscillator Control," *IEEE Transactions on Power Electronics*, vol. 29, no. 11, pp. 6124–6138, November 2014.

[18] L. A. B. Tôrres, J. P. Hespanha, and J. Moehlis, "Power supplies dynamical synchronization without communication," in *Proc. of the Power & Energy Society 2012 General Meeting*, July 2012.

[19] L. A. B. Tï¿œrres, J. P. Hespanha, and J. Moehlis, "Synchronization of identical oscillators coupled through a symmetric network with dynamics: A constructive approach with applications to parallel operation of inverters," *IEEE Transactions on Automatic Control*, vol. 60, no. 12, pp. 3226–3241, Dec 2015.

[20] B. B. Johnson, S. V. Dhople, A. O. Hamadeh, and P. T. Krein, "Synchronization of Nonlinear Oscillators in an LTI Electrical Power Network," *IEEE Transactions on Circuits and Systems I: Regular Papers*, vol. 61, no. 3, pp. 834–844, March 2014.

[21] B. B. Johnson, S. V. Dhople, J. L. Cale, A. O. Hamadeh, and P. T. Krein, "Oscillator-based inverter control for islanded three-phase microgrids," *IEEE Journal of Photovoltaics*, vol. 4, no. 1, pp. 387–395, January 2014.

[22] S. V. Dhople, B. B. Johnson, and A. O. Hamadeh, "Virtual Oscillator Control for voltage source inverters," in *Annual Allerton Conference on Communication, Control, and Computing*, October 2013, pp. 1359–1363.

[23] M. Sinha, F. Dörfler, B. B. Johnson, and S. V. Dhople, "Phase balancing in globally connected networks of Liénard-type oscillators," in *56th IEEE Conference on Decision and Control*, Dec 2017.

[24] M. Sinha, F. Dörfler, B. B. Johnson, and S. V. Dhople, "Synchronization of liénard-type oscillators in uniform electrical networks," in *2016 American Control Conference (ACC)*, July 2016, pp. 4311–4316.

[25] M. Sinha, F. Dörfler, B. B. Johnson, and S. V. Dhople, "Synchronization of Liénard-type oscillators in heterogeneous electrical networks," in *4th Indian Control Conference*, Dec 2017.

[26] ——, "Uncovering droop control laws embedded within the nonlinear dynamics of van der pol oscillators," *IEEE Trans. Control of Networked Sys.*, 2014, in review. [Online] Available at: `http://arxiv.org/abs/1411.6973`.

[27] M. Sinha, F. Dörfler, B. B. Johnson, and S. V. Dhople, "Virtual oscillator control subsumes droop control," in *American Control Conference*, submitted 2015.

[28] B. B. Johnson, M. Sinha, N. G. Ainsworth, F. Dörfler, and S. V. Dhople, "Synthesizing virtual oscillators to control islanded inverters," *IEEE Transactions on Power Electronics*, vol. 31, no. 8, pp. 6002–6015, 2016.

[29] M. Sinha, S. Dhople, B. Johnson, M. Rodriguez, and J. Poon, "Decentralized interleaving of paralleled dc-dc buck converters," in *2017 IEEE 18th Workshop on Control and Modeling for Power Electronics (COMPEL)*, July 2017, pp. 1–6.

[30] M. Sinha, J. Poon, B. Johnson, M. Rodr?guez, and S. V. Dhople, "Decentralized interleaving of parallel-connected buck converters," *IEEE Transactions on Power Electronics*, 2018, to appear.

[31] S. Sastry, *Nonlinear systems: analysis, stability, and control*. Springer Science & Business Media, 2013, vol. 10.

[32] M. W. Hirsch, S. Smale, and R. L. Devaney, *Differential equations, dynamical systems, and an introduction to chaos*. Academic press, 2012.

[33] D. W. Jordan and P. Smith, *Nonlinear ordinary differential equations*. Clarendon Press Oxford, 1987.

[34] S. H. Strogatz, *Nonlinear Dynamics and Chaos: With Applications to Physics, Biology, Chemistry, and Engineering*, 1st ed., ser. Studies in nonlinearity. Westview Press, Jan. 2001. [Online]. Available: http://www.worldcat.org/isbn/0738204536

[35] R. H. Rand, "Lecture notes on nonlinear vibrations," 2012.

[36] B. Van der Pol, "The nonlinear theory of electric oscillations," *Proceedings of the Institute of Radio Engineers*, vol. 22, no. 9, pp. 1051–1086, 1934.

[37] B. Van Der Pol and J. Van Der Mark, "Lxxii. the heartbeat considered as a relaxation oscillation, and an electrical model of the heart," *The London, Edinburgh, and Dublin Philosophical Magazine and Journal of Science*, vol. 6, no. 38, pp. 763–775, 1928.

[38] G. Wilson, "Hilbert's sixteenth problem," *Topology*, vol. 17, no. 1, pp. 53–73, 1978.

[39] M. Arcak, "Passivity as a design tool for group coordination," *IEEE Transactions on Automatic Control*, vol. 52, no. 8, pp. 1380–1390, 2007.

[40] A. Pavlov and L. Marconi, "Incremental passivity and output regulation," *Systems & Control Letters*, vol. 57, no. 5, pp. 400–409, 2008.

[41] A. Isidori and C. I. Byrnes, "Output regulation of nonlinear systems," *IEEE transactions on Automatic Control*, vol. 35, no. 2, pp. 131–140, 1990.

[42] C. Byrnesl, A. Isidoril, and J. Willems, "Feedback equivalence to passive nonlinear systems," *Progress in Systems and Control Theory*, p. 118, 1991.

[43] H. Kim and C. De Persis, "Adaptation and disturbance rejection for output synchronization of incrementally output–feedback passive systems," *International Journal of Robust and Nonlinear Control*, 2017. [Online]. Available: http://dx.doi.org/10.1002/rnc.3781

[44] F. Dörfler and F. Bullo, "Synchronization in complex oscillator networks: A survey," *Automatica*, vol. 50, no. 6, pp. 1539–1564, 2014.

[45] X. Li and G. Chen, "Synchronization and desynchronization of complex dynamical networks: An engineering viewpoint," *IEEE Trans. Circuits Syst. I: Fundam. Theory Appl.*, vol. 50, no. 11, pp. 1381–1390, Nov. 2003.

[46] A. Mauroy, P. Sacré, and R. J. Sepulchre, "Kick synchronization versus diffusive synchronization," in *IEEE Conference on Decision and Control*, 2012, pp. 7171–7183.

[47] A. Hamadeh, G.-B. Stan, R. Sepulchre, and J. Goncalves, "Global state synchronization in networks of cyclic feedback systems," *IEEE Trans. Autom. Control*, vol. 57, no. 2, pp. 478–483, Feb. 2012.

[48] G.-B. Stan and R. Sepulchre, "Analysis of interconnected oscillators by dissipativity theory," *IEEE Trans. Autom. Control*, vol. 52, no. 2, pp. 256–270, Feb. 2007.

[49] M. Arcak, "Passivity as a design tool for group coordination," *IEEE Trans. Autom. Control*, vol. 52, no. 8, pp. 1380–1390, Aug. 2007.

[50] A. Pogromsky and H. Nijmeijer, "Cooperative oscillatory behavior of mutually coupled dynamical systems," *IEEE Trans. Circuits Syst. I: Fundam. Theory Appl.*, vol. 48, no. 2, pp. 152–162, Feb. 2001.

[51] M. Bürger and C. De Persis, "Dynamic coupling design for nonlinear output agreement and time-varying flow control," in *IEEE Conference on Decision and Control*, 2014, pp. 1353–1358.

[52] ——, "Dynamic coupling design for nonlinear output agreement and time-varying flow control," *Automatica*, vol. 51, no. 1, pp. 210–222, 2015.

[53] A. Hamadeh, "Constructive Robust Synchronization of Networked Control Systems," Ph.D. dissertation, Cambridge University, UK, June 2010.

[54] S. V. Dhople, B. B. Johnson, F. Dörfler, and A. O. Hamadeh, "Synchronization of nonlinear circuits in dynamic electrical networks with general topologies," *IEEE Transactions on Circuits and Systems I: Regular Papers*, vol. 61, no. 9, pp. 2677–2690, September 2014.

[55] F. Dörfler and F. Bullo, "Kron reduction of graphs with applications to electrical networks," *IEEE Transactions on Circuits and Systems I: Regular Papers*, vol. 60, no. 1, pp. 150–163, Jan. 2013.

[56] F. Zhang, H. L. Trentelman, and J. M. A. Scherpen, "Dynamic feedback synchronization of lure networks via incremental sector boundedness," *IEEE Transactions on Automatic Control*, vol. 61, no. 9, pp. 2579–2584, Sept 2016.

[57] G. Casadei, L. Marconi, and C. De Persis, "Synchronization of nonlinear oscillators over networks with dynamic links," in *IEEE Conference on Decision and Control*. IEEE, 2015, pp. 6184–6189.

[58] M. Sinha, S. Dhople, B. Johnson, M. Rodriguez, and J. Poon, "Decentralized interleaving of paralleled dc-dc buck converters," in *2017 IEEE 18th Workshop on Control and Modeling for Power Electronics (COMPEL)*, July 2017, pp. 1–6.

[59] H. Khalil, *Nonlinear Systems*, 3rd ed. Upper Saddle River, NJ: Prentice Hall, 2002.

[60] Y. Kuramoto, "Self-entrainment of a population of coupled non-linear oscillators," in *International symposium on mathematical problems in theoretical physics*. Springer, 1975, pp. 420–422.

[61] ——, *Chemical oscillations, waves, and turbulence*. Springer Science & Business Media, 2012, vol. 19.

[62] F. Dörfler and F. Bullo, "Synchronization in complex networks of phase oscillators: A survey," *Automatica*, vol. 50, no. 6, pp. 1539–1564, 2014.

[63] D. Aronson, M. Golubitsky, and J. Mallet-Paret, "Ponies on a merry-go-round in large arrays of Josephson junctions," *Nonlinearity*, vol. 4, no. 3, p. 903, 1991.

[64] H. Gang, X. Fagen, Q. Zhilin, and S. Pengliang, "Antiphase states in coupled oscillator systems," *Communications in Theoretical Physics*, vol. 31, no. 1, p. 99, 1999.

[65] P. Ashwin, G. King, and J. W. Swift, "Three identical oscillators with symmetric coupling," *Nonlinearity*, vol. 3, no. 3, p. 585, 1990.

[66] D. A. Paley, N. E. Leonard, and R. Sepulchre, "Oscillator models and collective motion: Splay state stabilization of self-propelled particles," in *Proceedings of the 44th IEEE Conference on Decision and Control*. IEEE, 2005, pp. 3935–3940.

[67] D. J. Klein, P. Lee, K. A. Morgansen, and T. Javidi, "Integration of communication and control using discrete time Kuramoto models for multivehicle coordination over broadcast networks," *IEEE Journal on Selected Areas in Communications*, vol. 26, no. 4, pp. 695–705, 2008.

[68] D. Anderson, A. Tenzer, G. Barlev, M. Girvan, T. M. Antonsen, and E. Ott, "Multiscale dynamics in communities of phase oscillators," *Chaos: An Interdisciplinary Journal of Nonlinear Science*, vol. 22, no. 1, p. 013102, 2012.

[69] R. Sepulchre, D. A. Paley, and N. E. Leonard, "Stabilization of planar collective motion with limited communication," *IEEE Transactions on Automatic Control*, vol. 53, no. 3, pp. 706–719, 2008.

[70] Z. Chen and H.-T. Zhang, "A remark on collective circular motion of heterogeneous multi-agents," *Automatica*, vol. 49, no. 5, pp. 1236–1241, 2013.

[71] G. Teschl, *Ordinary differential equations and dynamical systems*. American Mathematical Society Providence, 2012, vol. 140.

[72] A. Jain and D. Ghose, "Stabilization of collective motion in synchronized, balanced and splay phase arrangements on a desired circle," in *American Control Conference (ACC)*, 2015, pp. 731–736.

[73] R. A. Horn and C. R. Johnson, *Matrix Analysis*. Cambridge University Press, 2012.

[74] M. C. Chandorkar, D. M. Divan, and R. Adapa, "Control of parallel connected inverters in standalone AC supply systems," *IEEE Transactions on Industry Applications*, vol. 29, no. 1, pp. 136–143, January 1993.

[75] Q.-C. Zhong, "Robust droop controller for accurate proportional load sharing among inverters operated in parallel," *IEEE Transactions on Industrial Electronics*, vol. 60, no. 4, pp. 1281–1290, 2013.

[76] N. Pogaku, M. Prodanovic, and T. Green, "Modeling, analysis and testing of autonomous operation of an inverter-based microgrid," *IEEE Transactions on Power Electronics*, vol. 22, no. 2, pp. 613–625, March 2007.

[77] A. Bidram and A. Davoudi, "Hierarchical structure of microgrids control system," *IEEE Transactions on Smart Grid*, vol. 3, no. 4, pp. 1963–1976, 2012.

[78] L. A. B. Tôrres, J. P. Hespanha, and J. Moehlis, "Synchronization of oscillators coupled through a network with dynamics: A constructive approach with applications to the parallel operation of voltage power supplies," Sep. 2013, submitted to journal publication.

[79] R. Rand and P. Holmes, "Bifurcation of periodic motions in two weakly coupled Van der Pol oscillators," *International Journal of Non-Linear Mechanics*, vol. 15, no. 4, pp. 387–399, 1980.

[80] H. K. Khalil, *Nonlinear Systems*, 3rd ed. Prentice Hall, 2002.

[81] F. Dörfler, J. W. Simpson-Porco, and F. Bullo, "Breaking the hierarchy: Distributed control & economic optimality in microgrids," 2014, submitted. Available at http://arxiv.org/pdf/1401.1767v1.pdf. [Online]. Available: http://arxiv.org/abs/1401.1767

[82] P. Kundur, N. J. Balu, and M. G. Lauby, *Power system stability and control*. McGraw-hill New York, 1994, vol. 7.

[83] J. M. Guerrero, M. Chandorkar, T. Lee, and P. C. Loh, "Advanced control architectures for intelligent microgrids—Part I: Decentralized and hierarchical control," *IEEE Transactions on Industrial Electronics*, vol. 60, no. 4, pp. 1254–1262, Apr. 2013.

[84] Q.-C. Zhong, "Robust droop controller for accurate proportional load sharing among inverters operated in parallel," *IEEE Transactions on Industrial Electronics*, vol. 60, no. 4, pp. 1281–1290, April 2013.

[85] J. M. Guerrero, J. C. Vasquez, J. Matas, L. G. de Vicuña, and M. Castilla, "Hierarchical control of droop-controlled AC and DC microgrids–a general approach toward standardization," *IEEE Trans. Ind. Electron.*, vol. 58, no. 1, pp. 158–172, 2011.

[86] R. Majumder, A. Ghosh, G. Ledwich, and F. Zare, "Angle droop versus frequency droop in a voltage source converter based autonomous microgrid," in *IEEE Power & Energy Society General Meeting*, Calgary, AB, Canada, Jul. 2009, pp. 1–8.

[87] S. E. Tuna, "Synchronization analysis of coupled lienard-type oscillators by averaging," *Automatica*, vol. 48, no. 8, pp. 1885–1891, 2012.

[88] P. T. Krein, J. Bentsman, R. M. Bass, and B. C. Lesieutre, "On the use of averaging for the analysis of power electronic systems," in *IEEE Power Electronics Specialists Conf.*, June 1989, pp. 463–467.

[89] S. R. Sanders, J. M. Noworolski, X. Z. Liu, and G. C. Verghese, "Generalized averaging method for power conversion circuits," *IEEE Trans. Power Electron.*, vol. 6, no. 2, pp. 251–259, 1991.

[90] J. W. Kimball and P. T. Krein, "Singular perturbation theory for dc-dc converters and application to PFC converters," *IEEE Trans. Power Electron.*, vol. 23, no. 6, pp. 2970–2981, 2008.

[91] B. Lehman and R. M. Bass, "Switching frequency dependent averaged models for PWM dc-dc converters," *IEEE Trans. Power Electron.*, vol. 11, no. 1, pp. 89–98, 1996.

[92] V. A. Caliskan, O. Verghese, and A. M. Stankovic, "Multifrequency averaging of dc-dc converters," *IEEE Trans. Power Electron.*, vol. 14, no. 1, pp. 124–133, 1999.

[93] J. W. Simpson-Porco, F. Dörfler, and F. Bullo, "Synchronization and power sharing for droop-controlled inverters in islanded microgrids," *Automatica*, vol. 49, no. 9, pp. 2603–2611, 2013.

[94] J. W. Simpson-Porco, F. Dörfler, and F. Bullo, "Voltage stabilization in microgrids via quadratic droop control,"," in *IEEE Conf. on Decision and Control, Florence, Italy*, 2013, pp. 7582–7589.

[95] J. Schiffer, D. Goldin, J. Raisch, and T. Sezi, "Synchronization of droop-controlled microgrids with distributed rotational and electronic generation," in *IEEE 52nd Annual Conference on Decision and Control*, 2013, pp. 2334–2339.

[96] Q.-C. Zhong and Y. Zeng, "Parallel operation of inverters with different types of output impedance," in *Annual Conference of the IEEE of Industrial Electronics Society*, Nov 2013, pp. 1398–1403.

[97] A. Yazdani and R. Iravani, *Voltage-Sourced Converters in Power Systems*. Hoboken, NJ: John Wiley & Sons, Inc., 2010.

[98] A. H. Nayfeh, *Introduction to Perturbation Techniques*. John Wiley & Sons, 2011.

[99] A. Davoudi, J. Jatskevich, and T. De Rybel, "Numerical state-space average-value modeling of PWM DC-DC converters operating in DCM and CCM," *IEEE Transactions on Power Electronics*, vol. 21, no. 4, pp. 1003–1012, July 2006.

[100] C. A. Hernandez-Aramburo, T. C. Green, and N. Mugniot, "Fuel consumption minimization of a microgrid," *IEEE Trans. Ind. Appl.*, vol. 41, no. 3, pp. 673–681, May 2005.

[101] P. T. Krein, *Elements of Power Electronics.* New York, NY: Oxford University Press, 1998.

[102] P. Jakobsen, "Introduction to the method of multiple scales," *arXiv preprint arXiv:1312.3651*, 2013.

[103] J. Rocabert, A. Luna, F. Blaabjerg, and P. Rodríguez, "Control of power converters in ac microgrids," *IEEE Trans. Power Electron.*, vol. 27, no. 11, pp. 4734–4749, Nov. 2012.

[104] Q.-C. Zhong and Y. Zeng, "Parallel operation of inverters with different types of output impedance," in *Industrial Electronics Society Conf.*, Nov. 2013, pp. 1398–1403.

[105] M. Sinha, S. Dhople, B. Johnson, N. Ainsworth, and F. Dorfler, "Nonlinear supersets to droop control," in *IEEE 16th Workshop on Control and Modeling for Power Electronics (COMPEL)*, July 2015, pp. 1–6.

[106] Y.-R. Mohamed and E. El-Saadany, "Adaptive decentralized droop controller to preserve power sharing stability of paralleled inverters in distributed generation microgrids," *IEEE Trans. Power Electron.*, vol. 23, no. 6, pp. 2806–2816, Nov. 2008.

[107] A. Micallef, M. Apap, C. Spiteri-Staines, J. M. Guerrero, and J. C. Vasquez, "Reactive power sharing and voltage harmonic distortion compensation of droop controlled single phase islanded microgrids," *IEEE Transactions on Smart Grid*, vol. 5, no. 3, pp. 1149–1158, May 2014.

[108] H. Avelar, W. Parreira, J. Vieira, L. de Freitas, and E. Alves Coelho, "A state equation model of a single-phase grid-connected inverter using a droop control scheme with extra phase shift control action," *IEEE Trans. Ind. Electron.*, vol. 59, no. 3, pp. 1527–1537, Mar. 2012.

[109] N. B. Gallegos, V. G. Segura, and M. Molinas, "Synchronization properties of voltage source converters when seen as coupled oscillators based on the kuramoto model."

[110] B. Johnson, M. Rodriguez, M. Sinha, and S. Dhople, "Comparison of virtual oscillator and droop control," in *2017 IEEE 18th Workshop on Control and Modeling for Power Electronics (COMPEL)*, July 2017, pp. 1–6.

[111] N. R. Draper and H. Smith, *Applied regression analysis 2nd ed.* John Wiley and Sons, New York, 1981.

[112] J. Schiffer, R. Ortega, A. Astolfi, J. Raisch, and T. Sezi, "Conditions for stability of droop–controlled inverter–based microgrids," *Automatica. Submitted*, 2013.

[113] R. Ortega, A. Van Der Schaft, B. Maschke, and G. Escobar, "Interconnection and damping assignment passivity-based control of port-controlled hamiltonian systems," *Automatica*, vol. 38, no. 4, pp. 585–596, 2002.

[114] R. A. Horn and C. R. Johnson, *Matrix analysis.* Cambridge university press, 2012.

[115] D. Carlson and H. Schneider, "Inertia theorems for matrices: The semidefinite case," *Jnl. of Mathematical Analysis and Applications*, vol. 6, pp. 430–446, 1963.

[116] F. Dörfler, M. Chertkov, and F. Bullo, "Synchronization in complex oscillator networks and smart grids," *Proceedings of the National Academy of Sciences*, vol. 110, no. 6, pp. 2005–2010, February 2013. [Online]. Available: http://www.pnas.org/content/early/2013/01/11/1212134110

[117] L. Che and M. Shahidehpour, "Dc microgrids: Economic operation and enhancement of resilience by hierarchical control," *IEEE Transactions on Smart Grid*, vol. 5, no. 5, pp. 2517–2526, Sept 2014.

[118] M. Baranwal, S. M. Salapaka, and M. V. Salapaka, "Robust decentralized voltage control of dc-dc converters with applications to power sharing and ripple sharing," in *American Control Conference (ACC)*, July 2016, pp. 7444–7449.

[119] A. Costabeber, P. Mattavelli, and S. Saggini, "Digital time-optimal phase shedding in multiphase buck converters," *IEEE Transactions on Power Electronics*, vol. 25, no. 9, pp. 2242–2247, 2010.

[120] Y. C. Wang and Y. Y. Tzou, "Design and realization of a digital multiphase-interleaved vrm controller using FPGA," in *33rd Annual Conference of the IEEE Industrial Electronics Society (IECON)*, Nov 2007, pp. 1978–1982.

[121] E. A. Burton, G. Schrom, F. Paillet, J. Douglas, W. J. Lambert, K. Radhakrishnan, and M. J. Hill, "FIVR — fully integrated voltage regulators on 4th generation Intel Core SoCs," in *IEEE Applied Power Electronics Conference and Exposition*, Mar 2014, pp. 432–439.

[122] Y. C. Chen, J. D. Hsu, Y. A. Ang, and T. Y. Yang, "A new phase shedding scheme for improved transient behavior of interleaved boost pfc converters," in *IEEE Applied Power Electronics Conference and Exposition*, Mar 2014, pp. 1916–1919.

[123] J. W. Kolar, G. R. Kamath, N. Mohan, and F. C. Zach, "Self-adjusting input current ripple cancellation of coupled parallel connected hysteresis-controlled boost power factor correctors," in *IEEE Power Electronics Specialists Conference*, vol. 1, Jun 1995, pp. 164–173.

[124] S. H. Strogatz, *Nonlinear dynamics and chaos: with applications to physics, biology, chemistry, and engineering.* Westview press, 2014.

[125] M. Colombino, D. Groß, and F. Dörfler, "Global phase and voltage synchronization for power inverters: a decentralized consensus-inspired approach," in *Proceedings of the 56th IEEE Conference on Decision and Control*, 2017.

[126] M. Sinha, F. Dörfler, B. B. Johnson, and S. V. Dhople, "Uncovering droop control laws embedded within the nonlinear dynamics of Van der Pol oscillators," *IEEE Transactions on Control of Network Systems*, vol. 4, no. 2, pp. 347–358, June 2017.

[127] M. Li, Y. Gui, J. M. Guerrero, R. Teodorescu, and J. C. Vasquez, "Adaptive synchronization of grid-connected three-phase inverters by using virtual oscillator control," in *IEEE Applied Power Electronics Conference and Exposition*, Mar 2018.

[128] J. Hu and H. Ma, "Synchronization of the carrier wave of parallel three-phase inverters with virtual oscillator control," *IEEE Transactions on Power Electronics*, vol. 32, no. 10, pp. 7998–8007, Oct 2017.

[129] C. De Persis and B. Jayawardhana, "On the internal model principle in the coordination of nonlinear systems," *IEEE Transactions on Control of Network Systems*, vol. 1, no. 3, pp. 272–282, 2014.

[130] G.-B. Stan and R. Sepulchre, "Analysis of interconnected oscillators by dissipativity theory," *IEEE Transactions on Automatic Control*, vol. 52, no. 2, pp. 256–270, 2007.

[131] R. Sepulchre, D. Paley, and N. Leonard, "Collective motion and oscillator synchronization," in *Cooperative control*. Springer, 2005, pp. 189–205.

[132] M. Sinha, F. Dörfler, B. B. Johnson, and S. V. Dhople, "Uncovering droop control laws embedded within the nonlinear dynamics of van der pol oscillators," *arXiv*, vol. abs/1411.6973, 2014. [Online]. Available: http://arxiv.org/abs/1411.6973

[133] Y. Panov and M. M. Jovanovic, "Stability and dynamic performance of current-sharing control for paralleled voltage regulator modules," *IEEE Transactions on Power Electronics*, vol. 17, no. 2, pp. 172–179, March 2002.

[134] H. Wang, M. Han, R. Han, J. M. Guerrero, and J. C. Vasquez, "A decentralized current-sharing controller endows fast transient response to parallel dc-dc converters," *IEEE Transactions on Power Electronics*, vol. 33, no. 5, pp. 4362–4372, May 2018.

[135] H. Mao, L. Yao, C. Wang, and I. Batarseh, "Analysis of inductor current sharing in nonisolated and isolated multiphase dc-dc converters," *IEEE Transactions on Industrial Electronics*, vol. 54, no. 6, pp. 3379–3388, December 2007.

[136] W. E. Vander Velde, *Multiple-input describing functions and nonlinear system design*. McGraw-Hill, New York, 1968.

[137] J. Sun, "Pulse-width modulation," in *Dynamics and Control of Switched Electronic Systems*. Springer, 2012, pp. 25–61.

Appendix A

Details on Averaging Operations

We show in this appendix that by means of averaging and integration by parts, we can derive (3.10) from (3.16). We begin by considering the amplitude dynamics. Recall that by standard averaging arguments [80, Theorem 10.4], we know that the solution of the averaged VOC dynamics (3.15) is $\mathcal{O}(\varepsilon)$ close the solution of original VOC dynamics (3.14) for $s \in [0, t^*]$, i.e., $r(\tau) - \overline{r}(\varepsilon\tau) = \mathcal{O}(\varepsilon)$. From (3.16), we have

$$\begin{aligned}
&\dot{\overline{r}}(\varepsilon\tau) - \frac{\varepsilon\alpha}{2}\left(\overline{r}(\varepsilon\tau) - \beta\frac{1}{4}\overline{r}^3(\varepsilon\tau)\right) \\
&\quad = -\frac{\varepsilon}{2\pi}\int_{\tau-2\pi}^{\tau} i(s)\cos(s+\overline{\theta})ds \\
&\quad = -\frac{\varepsilon}{2\pi}\int_{\tau-2\pi}^{\tau} \frac{1}{\overline{r}(\varepsilon s)}\overline{r}(\varepsilon s)i(s)\cos(s+\overline{\theta})ds \\
&\quad = -\frac{\varepsilon}{2\pi}\int_{\tau-2\pi}^{\tau} \frac{1}{\overline{r}(\varepsilon s)}\left(r(s) - \mathcal{O}(\varepsilon)\right)i(s)\cos(s+\overline{\theta})ds \\
&\quad = -\frac{\varepsilon}{2\pi}\int_{\tau-2\pi}^{\tau} \frac{1}{\overline{r}(\varepsilon s)}r(s)i(s)\cos(s+\overline{\theta})ds + \mathcal{O}(\varepsilon^2) \\
&\quad = -\frac{\varepsilon}{2\pi}\left[\frac{1}{\overline{r}(\varepsilon s)}\int r(s)i(s)\cos(s+\overline{\theta})ds\right]_{\tau-2\pi}^{\tau} \\
&\quad - \frac{\varepsilon}{2\pi}\int_{\tau-2\pi}^{\tau} \frac{-\dot{\overline{r}}(\varepsilon s)}{\overline{r}^2(\varepsilon s)}\left(\int r(s)i(s)\cos(s+\overline{\theta})ds\right)ds \\
&\quad + \mathcal{O}(\varepsilon^2)\,,
\end{aligned} \tag{A.1}$$

where the expansion in the last equality leverages integration by parts, and we changed the integration limits from $[0, 2\pi]$ as in (3.16) to $[\tau, \tau - 2\pi]$ without loss of generality as the

integrand is 2π-periodic. As $\dot{\overline{r}}(\varepsilon s) = \mathcal{O}(\varepsilon)$, see (3.16), we have

$$\frac{\varepsilon}{2\pi}\int_{\tau-2\pi}^{\tau}\frac{-\dot{\overline{r}}(\varepsilon s)}{\overline{r}^2(\varepsilon s)}\left(\int r(s)i(s)\cos(s+\overline{\theta})ds\right)ds = \mathcal{O}(\varepsilon^2)\,,$$

and therefore ignoring $\mathcal{O}(\varepsilon^2)$ in (A.1) yields:

$$\begin{aligned}\dot{\overline{r}}(\varepsilon\tau) - \frac{\varepsilon\alpha}{2}\left(\overline{r}(\varepsilon\tau) - \beta\frac{1}{4}\overline{r}^3(\varepsilon\tau)\right)\\ = -\frac{\varepsilon}{2\pi}\left[\frac{1}{\overline{r}(\varepsilon s)}\int r(s)i(s)\cos(s+\overline{\theta})ds\right]_{\tau-2\pi}^{\tau}.\end{aligned}$$

The right-hand side can be further simplified as:

$$\begin{aligned}&\left[\frac{1}{\overline{r}(\varepsilon s)}\int r(s)i(s)\cos(s+\overline{\theta})ds\right]_{\tau-2\pi}^{\tau}\\ &= \frac{1}{\overline{r}(\varepsilon\tau)}\int r(s)i(s)\cos(s+\overline{\theta})ds\Big|_{\tau}\\ &\quad - \frac{1}{\overline{r}(\varepsilon(\tau-2\pi))}\int r(s)i(s)\cos(s+\overline{\theta})ds\Big|_{\tau-2\pi}\\ &= \frac{1}{\overline{r}(\varepsilon\tau)}\int r(s)i(s)\cos(s+\overline{\theta})ds\Big|_{\tau}\\ &\quad - \frac{1}{\overline{r}(\varepsilon\tau)+\mathcal{O}(\varepsilon)}\int r(s)i(s)\cos(s+\overline{\theta})ds\Big|_{\tau-2\pi},\end{aligned} \tag{A.2}$$

where we have the used relation

$$\overline{r}(\varepsilon\tau) = \overline{r}(\varepsilon(\tau-2\pi)) + \int_{\tau-2\pi}^{\tau}\dot{\overline{r}}(\varepsilon s)ds = \overline{r}(\varepsilon(\tau-2\pi)) + \mathcal{O}(\varepsilon)\,, \tag{A.3}$$

as $\dot{\overline{r}}(\varepsilon s) = \mathcal{O}(\varepsilon)$. Thus, we can write:

$$\begin{aligned}
&\left[\frac{1}{\overline{r}(\varepsilon s)}\int r(s)i(s)\cos(s+\overline{\theta})ds\right]_{\tau-2\pi}^{\tau} \\
&= \frac{1}{\overline{r}(\varepsilon\tau)}\int r(s)i(s)\cos(s+\overline{\theta})ds\bigg|_{\tau} \\
&\quad - \frac{1}{\overline{r}(\varepsilon\tau)}(1+\mathcal{O}(\varepsilon))^{-1}\int r(s)i(s)\cos(s+\overline{\theta})ds\bigg|_{\tau-2\pi} \\
&= \frac{1}{\overline{r}(\varepsilon\tau)}\bigg(\int r(s)i(s)\cos(s+\overline{\theta})ds\bigg|_{\tau} \\
&\quad - \int r(s)i(s)\cos(s+\overline{\theta})ds\bigg|_{\tau-2\pi}\bigg) + \mathcal{O}(\varepsilon) \\
&= \frac{1}{\overline{r}(\varepsilon\tau)}\int_{\tau-2\pi}^{\tau} r(s)i(s)\cos(s+\overline{\theta})ds + \mathcal{O}(\varepsilon) \\
&= \frac{1}{\overline{r}(\varepsilon s)}\int_{0}^{2\pi} r(s)i(s)\cos(s+\overline{\theta})ds + \mathcal{O}(\varepsilon)\,. \qquad \text{(A.4)}
\end{aligned}$$

where we have used the fact that the integrand is 2π-periodic to change the limits of the definite integral. By substituting (A.4) in (A.1) and ignoring $\mathcal{O}(\varepsilon^2)$, we finally arrive at

$$\dot{\overline{r}} = \frac{\varepsilon\alpha}{2}\left(\overline{r} - \beta\frac{1}{4}\overline{r}^3\right) - \frac{\varepsilon}{2\pi\overline{r}}\int_0^{2\pi} r(\tau)i(\tau)\cos(\tau+\overline{\theta})d\tau\,. \qquad \text{(A.5)}$$

where we have changed the dummy variable s to τ. Furthermore, by acknowledging that $\theta(\varepsilon) - \overline{\theta}(\varepsilon\tau) = \mathcal{O}(\varepsilon)$ for τ in $[0, t^*]$, we can expand the cosine function in (A.5) as:

$$\begin{aligned}
&\cos(\tau+\overline{\theta}) = \cos(\tau+\theta-\mathcal{O}(\varepsilon)) \\
&= \cos(\tau+\theta)\cos(\mathcal{O}(\varepsilon)) + \sin(\tau+\theta)\sin(\mathcal{O}(\varepsilon)) \\
&= \cos(\tau+\theta)(1-\mathcal{O}(\varepsilon^2)) + \sin(\tau+\theta)\mathcal{O}(\varepsilon)\,.
\end{aligned}$$

Ignoring $\mathcal{O}(\varepsilon^2)$ terms and transitioning from τ to t coordinates, we can express (A.5) as a function of the average real power as below:

$$\begin{aligned}
\frac{d\overline{r}}{dt} &= \frac{\alpha}{2C}\left(\overline{r} - \beta\frac{1}{4}\overline{r}^3\right) - \frac{\omega}{2\pi C\overline{r}}\int_0^{\frac{2\pi}{\omega}} i(t)r(t)\cos(\omega t+\theta)dt, \\
&= \frac{\alpha}{2C}\left(\overline{r} - \beta\frac{1}{4}\overline{r}^3\right) - \frac{\omega}{2\pi C\overline{r}}\overline{P}\,. \qquad \text{(A.6)}
\end{aligned}$$

The phase dynamics can be analysed in a similar manner as follows. From (3.15), we have

$$\begin{aligned}
\dot{\overline{\theta}}(\varepsilon\tau) &= \frac{\varepsilon}{2\pi}\int_{\tau-2\pi}^{\tau}\frac{1}{\overline{r}(\varepsilon s)}i(s)\sin(s+\overline{\theta})ds \\
&= \frac{\varepsilon}{2\pi}\int_{\tau-2\pi}^{\tau}\frac{\overline{r}(\varepsilon s)}{\overline{r}^2(\varepsilon s)}i(s)\sin(s+\overline{\theta})ds \\
&= \frac{\varepsilon}{2\pi}\int_{\tau-2\pi}^{\tau}\frac{1}{\overline{r}^2(\varepsilon s)}(r(s)-\mathcal{O}(\varepsilon))i(s)\sin(s+\overline{\theta})ds \\
&= \frac{\varepsilon}{2\pi}\int_{\tau-2\pi}^{\tau}\frac{1}{\overline{r}^2(\varepsilon s)}r(s)i(s)\sin(s+\overline{\theta})ds+\mathcal{O}(\varepsilon^2) \\
&= \frac{\varepsilon}{2\pi}\left[\frac{1}{\overline{r}^2(\varepsilon\tau)}\int r(s)i(s)\sin(s+\overline{\theta})ds\right]_{\tau-2\pi}^{\tau} \\
&\quad -\frac{\varepsilon}{\pi}\int_{\tau-2\pi}^{\tau}\frac{\dot{\overline{r}}(\varepsilon s)}{\overline{r}^3(\varepsilon s)}\left(\int r(s)i(s)\sin(s+\overline{\theta})d\tau\right)d\tau+\mathcal{O}(\varepsilon^2),
\end{aligned}$$

where the last line again follows from integration by parts. Utilizing the fact that $\dot{\overline{r}}(\varepsilon\tau) = \mathcal{O}(\varepsilon)$, see (3.15), we have:

$$\begin{aligned}
\dot{\overline{\theta}}(\varepsilon\tau) &= \frac{\varepsilon}{2\pi}\left[\frac{1}{\overline{r}^2(\varepsilon s)}\int r(s)i(s)\sin(s+\overline{\theta})d\tau\right]_{\tau-2\pi}^{\tau}, \\
&= \frac{\varepsilon}{2\pi}\left(\frac{1}{\overline{r}^2(\varepsilon\tau)}\int r(s)i(s)\sin(s+\overline{\theta})d\tau\Big|_{\tau}\right. \\
&\quad \left.-\frac{1}{\overline{r}^2(\varepsilon(\tau-2\pi))}\int r(s)i(s)\sin(s+\overline{\theta})d\tau\Big|_{\tau-2\pi}\right), \qquad \text{(A.7)}
\end{aligned}$$

where we have ignored $\mathcal{O}(\varepsilon^2)$ and higher-order terms. Equation (A.7) can be reformulated by using (A.3) as

$$\begin{aligned}
\dot{\overline{\theta}}(\varepsilon\tau) &= \frac{\varepsilon}{2\pi}\left(\frac{1}{\overline{r}^2(\varepsilon\tau)}\int r(s)i(s)\sin(s+\overline{\theta})ds\Big|_{\tau}\right. \\
&\quad \left.-\frac{(1+\mathcal{O}(\varepsilon))^{-2}}{\overline{r}^2(\varepsilon\tau)}\int r(s)i(s)\sin(s+\overline{\theta})ds\Big|_{\tau-2\pi}\right), \\
&= \frac{\varepsilon}{2\pi}\frac{1}{\overline{r}^2(\varepsilon s)}\int_0^{2\pi} r(\tau)i\sin(\tau+\overline{\theta})d\tau+\mathcal{O}(\varepsilon^2)\,. \qquad \text{(A.8)}
\end{aligned}$$

Again, we can expand sine function in (A.8) as:

$$\begin{aligned}
&\sin(\tau + \overline{\theta}) = \sin(\tau + \theta - \mathcal{O}(\varepsilon)) \\
&= \sin(\tau + \theta)\cos(\mathcal{O}(\varepsilon)) - \cos(\tau + \theta)\sin(\mathcal{O}(\varepsilon)) \\
&= \sin(\tau + \theta)(1 - \mathcal{O}(\varepsilon^2)) - \cos(\tau + \theta)\mathcal{O}(\varepsilon)\,.
\end{aligned}$$

Ignoring $\mathcal{O}(\varepsilon^2)$ terms, we obtain:

$$\dot{\overline{\theta}} = \frac{\varepsilon}{2\pi}\frac{1}{\overline{r}^2}\int_0^{2\pi} r(\tau)i(\tau)\sin(\tau + \theta)d\tau\,. \tag{A.9}$$

Transitioning from τ to t co-ordinates, we thus have:

$$\begin{aligned}
\frac{d\overline{\theta}}{dt} &= \frac{\omega}{2\pi C}\frac{1}{\overline{r}^2}\int_0^{2\pi/\omega} r(t)i(t)\sin(\omega t + \theta)dt \\
&= \frac{\omega}{2\pi C}\frac{1}{\overline{r}^2}\overline{Q}\,.
\end{aligned} \tag{A.10}$$

Thus, we have arrived at (3.10).

Appendix B

Derivation of Equivalent Model for Analysis in Interleaving of Paralleled Buck Converters

B.0.1 Equivalence of (4.6)–(4.7) to (4.9)–(4.10)

Figure B.1(a) illustrates the closed-loop system as described by the system of equations (4.6)–(4.7): we refer to this as "system (a)" subsequently. The capacitor voltages of the oscillators, collected in the vector y, are used to generate signals in w, which dictate the switching in the buck converters. This is done using the linear time invariant filter $s + \gamma$. (See (4.7) in Section 4.1.3.) Furthermore, $\Delta = G_{\mathrm{L}}(s)I_N$ captures the linear component of the nonlinear-oscillator dynamics, with $G_{\mathrm{L}}(s)$ given by:

$$G_{\mathrm{L}}(s) := \frac{\varepsilon s}{s^2 - \varepsilon\sigma s + \omega_{\mathrm{sw}}^2}. \tag{B.1}$$

The oscillator dynamics are obtained by placing this in feedback with the cubic nonlinearity αy_j^3 (4.1). The approach to decompose the dynamics of Liénard-type oscillators into linear and nonlinear subsystems is commonly used for analysis since it permits the application of describing-functions approaches that extend frequency-domain methods to nonlinear systems [31]. In this particular case, the describing function for the feedback static nonlinearity, αy_j^3, is denoted by $G_{\mathrm{NL}}(y_j)$. All of these are collected in $G_{\mathrm{NL}}(y) = \mathrm{diag}\{G_{\mathrm{NL}}(y_1), \ldots, G_{\mathrm{NL}}(y_N)\}$. Finally, w feeds into a signum function with windowed integrators, a droop controller that generates the requisite duty command for power sharing, and

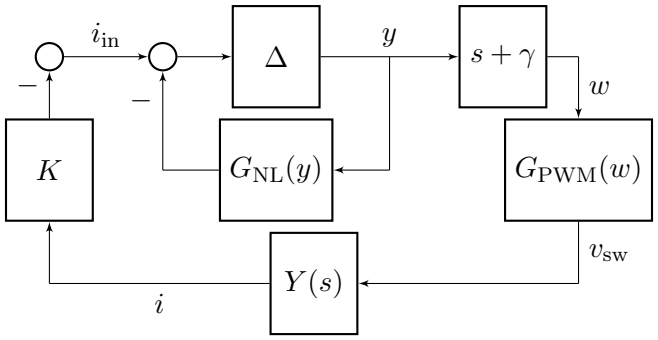

(a) Implementation: Block-diagram of closed-loop system with feedback described by (4.6)–(4.7).

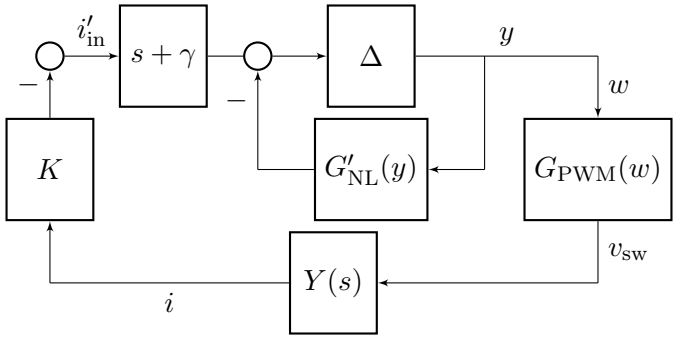

(b) Analysis: Equivalent representation of closed-loop system with feedback described by (4.9)–(4.10).

Figure B.1: Block-diagram representations of interconnected system with the equivalent coupled oscillator model dynamics (4.13): (a) version that is implemented in hardware, (b) equivalent version leveraged for analysis.(Source: [30])

a comparator with a carrier wave that generates the switching signals $q(t)$, which when multiplied by the dc-input voltage V_{dc} gives the switched voltages, $v_{\text{sw}} = \text{diag}\{V_{\text{dc}}q_1, \ldots, V_{\text{dc}}q_N\}$. These dynamics described above are captured in the frequency domain via the scalar transfer function block $s+\gamma$ and the describing function $G_{\text{PWM}}(w)$. Notice that $G_{\text{PWM}}(w)$ has a similar decoupled structure like $G_{\text{NL}}(y)$, and it collects the individual describing functions on the diagonal, i.e., $G_{\text{PWM}}(w) = \text{diag}\{G_{\text{PWM}}(w_1), \ldots, G_{\text{PWM}}(w_N)\}$. To close the loop, the feedback (function of the inductor currents, i, in the buck converters) is described by Kirchhoff's current laws, captured by the admittance of the electrical network, denoted by $Y(s)$, and matrix $K = \kappa I_N$, which is a diagonal static transfer function that incorporates the current gains (see (4.6)).

Figure B.1(b) shows the block diagram of the equivalent system (from an input-output standpoint), described by the system of equations (4.9)–(4.10): we refer to this as "system

(b)" subsequently. Notice that it differs from the original system Fig. B.1(a) in two aspects: i) the placement of the filter block $s+\gamma$, which now filters the feedback currents instead of the output voltages, and ii) the describing function for the nonlinearity, denoted by $G'_{\mathrm{NL}}(y)$. This is due to the fact that the systems have different coefficients α and α' for their nonlinearities. Next, we will derive the relationship between α and α' to ensure the input-output behavior of the systems are the same.

Observe that the i_j to w_j relation in system (a) is given by

$$\frac{\kappa G_{\mathrm{L}}(s) i_j(s)}{(s+\gamma)} = \left(1 + G_{\mathrm{L}}(s)\,(s+\gamma)\,G_{\mathrm{NL}}\left(\frac{w_j(s)}{(s+\gamma)}\right)\right) w_j(s), \tag{B.2}$$

and, similarly, the i_j to w_j relation in the equivalent system (b) is described by:

$$\kappa G_{\mathrm{L}}(s)(s+\gamma) i_j(s) = \left(1 + G_{\mathrm{L}}(s) G'_{\mathrm{NL}}\left(w_j\right)\right) w_j(s)\,. \tag{B.3}$$

Since $G_{\mathrm{L}}(s)$ is a linear block, it commutes with the scalar block $s+\gamma$. Thus, for the systems in (B.2) and (B.3) to be equivalent,

$$(s+\gamma) G_{\mathrm{NL}}\left(\frac{w_j(s)}{(s+\gamma)}\right) = G'_{\mathrm{NL}}(w_j(s)). \tag{B.4}$$

Since $\varepsilon \ll 1$ by design, $G_{\mathrm{L}}(s)$ has bandpass characteristics with resonant frequency ω_{sw}. Therefore, we can assume $w_j = A\cos\omega_{\mathrm{sw}} t$. Using the sinusoidal input describing function approach as outlined in [31, 136], we have

$$G_{\mathrm{NL}}(y_j) = \frac{3\alpha A^2}{4}\,, G'_{\mathrm{NL}}(y_j) = \frac{3\alpha' A^2}{4}\,. \tag{B.5}$$

At $s = \jmath\omega_{\mathrm{sw}}$,

$$\begin{aligned}(s+\gamma) G_{\mathrm{NL}}\left(\frac{w_j(s)}{(s+\gamma)}\right) &= \frac{3\alpha A^2(\jmath\omega_{\mathrm{sw}}+\gamma)}{4(\omega_{\mathrm{sw}}^2+\gamma^2)} \mathrm{e}^{\tan^{-1}(-\gamma/\omega_{\mathrm{sw}})} \\ &= \frac{3\alpha A^2}{4\sqrt{\omega_{\mathrm{sw}}^2+\gamma^2}}\,.\end{aligned} \tag{B.6}$$

Thus, for

$$\alpha' = \frac{\alpha}{\sqrt{\omega_{\mathrm{sw}}^2+\gamma^2}}\,, \tag{B.7}$$

both the systems (a) and (b) have equivalent input-output behavior.

B.0.2 Derivation of (4.13)

Denote the switching signal of the j-th buck converter as $q_j(t) \in \{0, 1\}$. Kirchhoff's voltage law indicates that:

$$V_{\rm dc} q_j(t) - R_{\rm f} i_j(t) - L_{\rm f} \frac{di_j}{dt} - R_{\rm Th} i_{\rm load} = v_{\rm load}, \tag{B.8}$$

where $i_{\rm load} := \sum_{j=1}^{N} i_j$. Recognizing (4.9), we can write:

$$i_{{\rm in}j} = \kappa \left(\frac{R_{\rm f}}{L_{\rm f}} i_j + \frac{di_j}{dt} \right) = \kappa \left(V_{\rm dc} q_j(t) - R_{\rm Th} i_{\rm load} - v_{\rm load} \right). \tag{B.9}$$

Substituting for $i_{{\rm in}j}$ from (B.9) in (4.5) yields:

$$\begin{aligned}
\dot{\overline{r}}_j = & \frac{\varepsilon \omega_{\rm sw}}{2} - \int_0^{T_{\rm sw}} \frac{\varepsilon \omega_{\rm sw}^2 \kappa v_{\rm load}}{2\pi L_{\rm f}} \cos(\omega_{\rm sw} t + \overline{\theta}_j) dt \\
& + \frac{\varepsilon \omega_{\rm sw}^2 \kappa}{2\pi L_{\rm f}} \int_0^{T_{\rm sw}} V_{\rm dc} q_j(t) \cos(\omega_{\rm sw} t + \overline{\theta}_j) dt \\
& - \frac{\varepsilon \omega_{\rm sw}^2 R_{\rm Th} \kappa}{2\pi L_{\rm f}} \int_0^{T_{\rm sw}} i_{\rm load} \cos(\omega_{\rm sw} t + \overline{\theta}_j) dt,
\end{aligned} \tag{B.10}$$

$$\begin{aligned}
\dot{\overline{\theta}}_j = & -\frac{\varepsilon \omega_{\rm sw}^2 \kappa}{2\pi \overline{r}_j L_{\rm f}} \int_0^{T_{\rm sw}} V_{\rm dc} q_j(t) \sin(\omega_{\rm sw} t + \overline{\theta}_j) dt \\
& + \frac{\varepsilon \omega_{\rm sw}^2 R_{\rm Th} \kappa}{2\pi \overline{r}_j L_{\rm f}} \int_0^{T_{\rm sw}} i_{\rm load} \sin(\omega_{\rm sw} t + \overline{\theta}_j) dt \\
& - \frac{\varepsilon \omega_{\rm sw}^2 \kappa}{2\pi L_{\rm f}} \int_0^{T_{\rm sw}} v_{\rm load} \sin(\omega_{\rm sw} t + \overline{\theta}_j) dt.
\end{aligned} \tag{B.11}$$

The PWM switching signal, $q_j(t)$, can be written as the following series for a particular duty ratio, D_j [137]

$$q_j(t) = D_j + \sum_{m=1}^{\infty} \frac{2}{m\pi} \sin(D_j m\pi) \cos(m(\omega_{\rm sw} t + \theta_j)). \tag{B.12}$$

Substituting for $q_j(t)$ from (B.12) in (B.10) yields

$$\begin{aligned}
\dot{\overline{r}}_j &= \frac{\varepsilon\omega_{\mathrm{sw}}}{2}\left(\sigma\overline{r}_j - 3\alpha\overline{r}_j^3\right) - \frac{\varepsilon\omega_{\mathrm{sw}}^2\kappa}{2\pi L_{\mathrm{f}}}\int_0^{T_{\mathrm{sw}}} v_{\mathrm{load}}\sin(\omega_{\mathrm{sw}}t+\overline{\theta}_j)dt \\
&\quad + \frac{\varepsilon\omega_{\mathrm{sw}}^2 R_{\mathrm{Th}}\kappa}{2\pi\overline{r}_j L_{\mathrm{f}}}\int_0^{T_{\mathrm{sw}}} i_{\mathrm{load}}\sin(\omega_{\mathrm{sw}}t+\overline{\theta}_j)dt + \frac{\varepsilon\omega_{\mathrm{sw}}^2\kappa V_{\mathrm{dc}}}{2\pi L_{\mathrm{f}}}\times \\
&\quad \sum_{m=1}^{\infty}\int_0^{T_{\mathrm{sw}}} \frac{2\sin D_j m\pi}{m\pi}\cos(m(\omega_{\mathrm{sw}}t+\theta_j))\cos(\omega_{\mathrm{sw}}t+\overline{\theta}_j)dt \qquad \text{(B.13)} \\
&= \frac{\varepsilon\omega_{\mathrm{sw}}}{2}\left(\sigma\overline{r}_j - 3\alpha\overline{r}_j^3\right) + \frac{\varepsilon\omega_{\mathrm{sw}}^2\kappa V_{\mathrm{dc}}\sin(D_j\pi)}{\pi L_{\mathrm{f}}} \\
&\quad + \frac{\varepsilon\omega_{\mathrm{sw}}^2 R_{\mathrm{Th}}\kappa}{2\pi\overline{r}_j L_{\mathrm{f}}}\int_0^{T_{\mathrm{sw}}} i_{\mathrm{load}}\sin(\omega_{\mathrm{sw}}t+\overline{\theta}_j)dt \\
&\quad - \frac{\varepsilon\omega_{\mathrm{sw}}^2\kappa}{2\pi L_{\mathrm{f}}}\int_0^{T_{\mathrm{sw}}} v_{\mathrm{load}}\sin(\omega_{\mathrm{sw}}t+\overline{\theta}_j)dt. \qquad \text{(B.14)}
\end{aligned}$$

In simplifying the second integral on the first line of (B.14), we have leveraged the following: i) $\overline{\theta}_j(t)$ is $\mathcal{O}(\varepsilon)$ close to $\theta_j(t)$, ii) since integrals of sines and cosines evaluate to zero over their period, only the fundamental harmonic remains in the $q_j(t)$ expansion and the average of $\cos^2(\omega_{\mathrm{sw}}t+\overline{\theta}_j)$ over its time period is $1/2$. Similarly, we get the following for the phase dynamics:

$$\begin{aligned}
\dot{\overline{\theta}}_j &= \frac{\varepsilon\omega_{\mathrm{sw}}^2 R_{\mathrm{Th}}\kappa}{2\pi\overline{r}_j L_{\mathrm{f}}}\int_0^{T_{\mathrm{sw}}} i_{\mathrm{load}}\sin(\omega_{\mathrm{sw}}t+\overline{\theta}_j)dt \\
&\quad - \frac{\varepsilon\omega_{\mathrm{sw}}^2\kappa}{2\pi L_{\mathrm{f}}}\int_0^{T_{\mathrm{sw}}} v_{\mathrm{load}}\sin(\omega_{\mathrm{sw}}t+\overline{\theta}_j)dt. \qquad \text{(B.15)}
\end{aligned}$$

Finally, note that the load current and voltage, i_{load} and v_{load}, are governed by the following dynamics:

$$L_{\text{f}}\frac{di_{\text{load}}}{dt} + (R_{\text{f}} + NR_{\text{Th}})\, i_{\text{load}} = \sum_{j=1}^{N} V_{\text{dc}} q_j(t) - N v_{\text{load}}. \tag{B.16}$$

$$C_{\text{load}}\frac{dv_{\text{load}}}{dt} + \frac{v_{\text{load}}}{R_{\text{load}}} = i_{\text{load}}. \tag{B.17}$$

While (B.17) follows straightforwardly from the circuit laws for an RC tank, (B.16) is derived by summing up all N instances of (B.8). Going back to (B.14) and (B.15), we use integration by parts for integrals involving i_{load} and v_{load} where we substitute appropriately from (B.16)-(B.17) to compute the requisite derivatives. Algebraic simplifications then yield (4.13).